UAB
Universitat Autònoma de Barcelona

# Proximity effects in heterostructures of graphene and low-symmetry 2D materials

**Josef SVETLIK**

UNIVERSITAT AUTÒNOMA DE BARCELONA

DOCTORAL THESIS IN PHYSICS

# Proximity effects in heterostructures of graphene and low-symmetry 2D materials

*Author:*
Josef SVĚTLÍK

*Supervisors:*
Prof. Dr. Sergio O. VALENZUELA
Dr. Juan F. SIERRA

*Tutor:*
Dr. Jordi SORT VIÑAS

*Research group:* Physics and Engineering of Nanodevices

*Institution:* Catalan Institute of Nanoscience and Nanotechnology

*Submitted to the doctoral school of the Autonomous University of Barcelona in partial fulfilment of the requirements for the degree of Doctor of Philosophy.*

Bellaterra, Barcelona

November 29, 2024

# Declaration of Authorship

I, Josef SVĚTLÍK, declare that this thesis titled, "Proximity effects in heterostructures of graphene and low-symmetry 2D materials" and the work presented in it are my own. I confirm that:

- This work was done wholly or mainly while in candidature for a research degree at this University.
- Where any part of this thesis has previously been submitted for a degree or any other qualification at this University or any other institution, this has been clearly stated.
- Where I have consulted the published work of others, this is always clearly attributed.
- Where I have quoted from the work of others, the source is always given. With the exception of such quotations, this thesis is entirely my own work.
- I have acknowledged all main sources of help.
- Where the thesis is based on work done by myself jointly with others, I have made clear exactly what was done by others and what I have contributed myself.

Signed:

Date:

UNIVERSITAT AUTÒNOMA DE BARCELONA

# *Abstract*

**Proximity effects in heterostructures of graphene and low-symmetry 2D materials**

by Josef SVĚTLÍK

Our information age requires the storage and processing of enormous amounts of data. The scaling of classical computing and storage devices is currently reaching physical limits. Devices based on new materials or working principles have to be developed to handle the growing amount of data faster and more efficiently. To this end, two-dimensional materials (2DMs) are promising due to their atomic-scale thickness and because they host a plethora of interesting physical phenomena that could be exploited in future devices. Moreover, the combination of 2DMs in van der Waals (vdW) heterostructures allows for tailoring the physical properties for a specific application through proximity effects. Graphene is a 2DM showing excellent electronic and spin transport properties that attracted considerable attention from the spintronic research community. The long spin coherence time in graphene makes it a perfect material for transmitting spin-encoded information; however, manipulating spin in pristine graphene proves challenging. A possible pathway to achieve spin manipulation in graphene involves inducing spin-orbit coupling (SOC) through proximity effects with 2D transition metal dichalcogenides (TMDCs). This dissertation investigates SOC phenomena in graphene induced by the proximity of low-symmetry TMDCs. Novel types of SOC are identified through spin relaxation and charge-spin interconversion measurements. The results expand our understanding of proximity-induced SOC phenomena in graphene and offer a new pathway for future-generation spintronic devices where spins are generated, manipulated and detected solely in graphene-based circuitry.

# Contents

# List of Figures

# List of Abbreviations

| | |
|---|---|
| **1D** | One-**D**imensional |
| **2D** | Two-**D**imensional |
| **2DM** | Two-**D**imensional **M**aterials |
| **AFM** | **A**tomic **F**orce **M**icroscopy |
| **CNP** | **C**harge **N**eutrality **P**oint |
| **CSI** | **C**harge -**S**pin **I**nterconversion |
| **CVD** | **C**hemical **V**apour **D**eposition |
| **DOS** | **D**ensity **O**f **S**tates |
| **FM** | **F**erro**M**agnetic |
| **GMR** | **G**iant **M**agneto **R**esistance |
| **HDD** | **H**ard **D**isk **D**rive |
| **IPA** | **I**so**P**ropyl **A**lcohol |
| **ISGE** | **I**nverse **S**pin **G**alvanic **E**ffect |
| **ISHE** | **I**nverse **S**pin **H**all **E**ffect |
| **MBE** | **M**olecular **B**eam **E**pitaxy |
| **MIBK** | **M**ethyl **I**sobutyl **K**etone |
| **MMA** | **M**ethyl **M**eth**A**crylate |
| **MRAM** | **M**agnetoresistive **R**andom **A**ccess **M**emory |
| **MOSFET** | **M**etal-**O**xide-**S**emiconductor **F**ield-**E**ffect **T**ransistor |
| **NM** | **N**on**M**agnetic |
| **PID** | **P**roportional **I**ntegral **D**erivative |
| **PDMS** | **P**oly**D**i**M**ethyl**S**iloxane |
| **PMMA** | **P**oly**M**ethyl **M**eth**A**crylate |
| **SEM** | **S**canning **E**lectron **M**icroscope |
| **SGE** | **S**pin **G**alvanic **E**ffect |
| **SHE** | **S**pin **H**all **E**ffect |
| **SOC** | **S**pin-**O**rbit **C**oupling |
| **SOF** | **S**pin-**O**rbit **F**ield |
| **SOT** | **S**pin-**O**rbit **T**orque |
| **SSD** | **S**olid **S**tate **D**rive |
| **STT** | **S**pin-**T**ransfer **T**orque |
| **TMDC** | **T**ransition **M**etal **D**i**C**halcogenide |
| **TMR** | **T**unnelling **M**agneto **R**esistance |
| **VCMA** | **V**oltage-**C**ontrolled **M**agnetic **A**nisotropy |
| **VdW** | **V**an **d**er **W**aals |

# Chapter 1

# Introduction

## 1.1 Transistor scaling and beyond

The transistor, a foundational component of modern electronics and computers, was developed by Bardeen and Brattain under the supervision of Shockley at Bell Labs in 1947 [1]. This compact solid-state semiconducting device, capable of functioning as an electrical switch, ultimately replaced less reliable inefficient and bulky thermionic valves. However, it was not until the development of the metal-oxide-semiconductor field-effect transistor (MOSFET) by Atalla and Kahng in 1960 that industrial-scale production of transistors for a wide range of applications became possible [2–4]. At the same time, Kilby patented the integrated circuit and Noyce invented a more practical monolithic version [5, 6]. Integrated circuits packed with interconnected transistors, capacitors, and resistors were quickly adopted by the electronics industry and became the platform for building modern consumer electronics.

Since then, the goal has been relatively straightforward — to pack more transistors into the same area. Thanks to the incredible effort of material scientists and electrical engineers, the number of transistors in integrated circuits approximately doubled every two years, a trend already noticed by Moore in 1965 [7]. His observation became later known as Moore's law and set the pace for the breathtaking miniaturisation that has been seen over the next 50 years. As of 2024, the number of transistors is higher than 200 million per $mm^2$ in state-of-the-art chips [8]. This exponential increase in transistor density over time brought the remarkable transformation of computers from large machines capable of performing modest calculations for a handful of individuals to ubiquitous pocket "supercomputers", always at our disposal.

Unfortunately, the downscaling of transistors is reaching its fundamental physical limits [9], as electric current starts to leak through the too-thin gate insulator and the too-short silicon channel, leading to small on/off ratios and an increase in power dissipation. These short-channel effects disrupted another scaling law originally observed by Dennard in 1974 also known as Dennard scaling [10]. Dennard discovered that the power density of devices stays roughly constant as their size decreases. Therefore, smaller devices require less power to operate providing improved chip efficiency. Dennard's law accompanied Moore's law until approximately 2006. Since then, a further decrease in transistor size has had an undesired side effect: an increase

in power dissipation due to the short-channel effects [11, 12]. Power dissipation constitutes a serious issue not only for efficiency but also for heat management. Maintaining computer chips at safe operating temperatures is becoming an increasingly challenging problem, and requires extra energy to cool them down. The problem has become so severe that more than 50 % of the total energy consumption in data centres is now spent on cooling [13]. The need to store and manipulate ever-larger amounts of data has steadily grown over the years, but it is increasing at an even faster pace now due to the artificial intelligence revolution currently underway. Therefore, more powerful and efficient devices are needed, but they can not be delivered by standard silicon technology. Instead, a new "Beyond Moore" information technology hardware has to be designed and developed.

Beyond Moore research explores alternative computing paradigms and advanced materials that would first complement and eventually replace silicon technology [14]. Advanced materials with reduced dimensionality include 2D materials [15], 1D carbon nanotubes [16], and 0D molecules [17]. Alternative technologies rely on exploiting degrees of freedom other than the electron's charge, such as the electric dipole [18, 19], orbital currents [20], valley [21, 22], or spin [23, 24]. The most prominent beyond-CMOS technologies include quantum [25], optical [26], and neuromorphic computing [27] and spintronics [23]. As this thesis falls within the field of spintronics, the focus will be solely on the description of early successes and future directions of spintronic technology.

## 1.2 Spintronics

Spintronics, a portmanteau of spin electronics, aims at utilizing the spin of an electron to store and process information. Using spins in addition or, ideally, instead of charge promises more energy-efficient, faster, and denser storage, memory, and logic devices due to the potentially negligible power dissipation in spintronic devices, where a pure spin current carries the information.

Spins, or their larger assembly in magnetic regions made up of many magnetic domains, have been used to store information for over a century [28]. The basic concept of magnetic storage has remained the same over time: read-and-write heads passing in proximity to the surface of the magnetic storage medium save or retrieve information. In write mode, the magnetization of parts of the magnetic medium is changed to record the signal. In read mode, the head passes over the magnetic segments of the storage medium and outputs voltages that directly correlate with the local magnetisation of the medium.

The first important contribution of magnetic recording technology to computers was the magnetic tape storage that replaced punch cards in the early 1950s [29]. It remains important for archival storage to this day because of its high volumetric density and cost-effectiveness. However, disk drives made of magnetic platters began to replace magnetic tape technology in computers since 1956 because they offered

faster data access. Hard disk drives (HDDs) saw a similarly impressive improvement in data density as processors in terms of transistor count. Whereas the first HDD, IBM RAMAC, could store about 2000 bits per square inch, current HDDs store more than 1600,000,000,000 bits per square inch [30]. This impressive advancement was achieved through continuous improvements in the magnetic material of the platters, the read-and-write heads, and the drive electronics.

The first spintronic device exploiting the flow of a spin-polarised current besides the magnetisation of a magnetic medium was the magnetoresistive (MR) read head. The anisotropic MR read head for HDDs was introduced by IBM in 1991. However, Fert's and Grünberg's discovery of giant magnetoresistance or GMR in 1988 already showed that a much more sensitive reading of magnetic field variations could be achieved with vertical heterostructures composed of alternating magnetic and non-magnetic (NM) conductive layers [31, 32]. By 1997, HDDs with spin valve GMR read heads started to replace anisotropic MR read heads. Around 2006, the NM layer sandwiched between the two ferromagnetic metals (FM) was replaced by a thin insulating layer in tunnelling MR (TMR) read heads [33, 34]. Solid-state drive (SSD) technology, based on transistors, has been increasingly substituting HDDs in consumer electronics (PCs, laptops, and smartphones); however, data centres, cloud servers, and other applications requiring massive storage capacity still rely on HDDs.

In addition to data storage, spintronics technology gains importance for non-volatile magnetoresistive random access memory (MRAM) devices. Recently, the toggle magnetoresistive random access memory (MRAM) and spin-transfer torque (STT)-MRAM were introduced [35, 36]. In STT-MRAM, magnetic switching is achieved by transferring the angular momentum of a spin-polarised current into a magnetic storage layer. Currently, spin-orbit torque (SOT)-MRAM [37] and voltage-controlled magnetic anisotropy (VCMA)-MRAM [38] are under intensive research and development. In SOT-MRAM, the spin-orbit coupling (SOC), i.e. coupling between the spin of an electron and its motion inside a crystal, is used to generate a spin current through charge-to-spin conversion phenomena. The accumulated spin angular momentum at the boundaries of the SOT layer is transferred to the adjacent magnetic layer, switching its magnetisation. SOT-MRAM provides higher density and faster speed of operation compared to STT-MRAM [39]. Moreover, SOT-MRAM has better endurance because the (large) writing current flows only through the SOT layer compared to STT-MRAM, where the current runs vertically through a highly sensitive tunnel barrier. In VCMA-MRAM, the strength of interfacial perpendicular magnetic anisotropy at the ferromagnet/oxide interface is modulated by accumulating charge at the interface and it also relies on the effect of SOC [40]. Indeed, SOC is gaining increasing attention in the context of the development of future-generation fast low-power spintronic devices operating at sub-nano second and sub-picojoule regimes [41–43] which makes a deeper understanding of it timely and extremely important.

Besides spintronic data storage and memory devices, intensive research is currently carried out on spin-logic devices [44, 45]. Spin-logic devices are particularly

interesting because they would allow for in-memory computing, i.e. the combination of memory and logic in a single spintronic device. Standard von Neumann computer architecture comprises separate memory and logic chips, thus, energy and time are wasted by moving the data between them. A spintronic device capable of in-memory computing would provide a better performance in terms of efficiency and speed. However, finding suitable materials for making such a device is challenging as the spin-encoded information must be manipulated and communicated across the chip. Spins undergo fast decoherence in most materials and the information is lost over short distances. Since magnetism, SOC and charge scattering are responsible for spin relaxation, NM materials with small SOC and high mobility are the best candidates for achieving long distance spin communication. A wonder material for this purpose, exhibiting negligible SOC and exceptionally high carrier mobility, was isolated by Novoselov and Geim in 2004 and is known as graphene [46].

The isolation of graphene stimulated a great interest in 2D materials (2DMs) research and led to the discovery of many more atomically thin crystal families [47]. Using 2DMs to build ultra-flat circuitry is envisioned as a possible way to extend Moore's law [48–50].

## 1.3 Graphene spintronics

Graphene enables spin transport at room temperature over distances larger than any other material due to its negligible SOC, lack of hyperfine interaction, and high carrier mobility [51, 52]. For this reason, graphene is an ideal material for spin communication. However, the absence of SOC in pristine graphene makes the generation, manipulation, and detection of spin currents impossible and graphene has to be contacted by FMs to inject and detect spins.

The SOC can be useful for generating spin currents through charge-to-spin conversion phenomena, such as the spin Hall effect (SHE) [53] or the Rashba-Edelstein effect [54, 55] also known as inverse spin galvanic effect (ISGE) [56, 57]. In addition, inverse effects, i.e. inverse SHE [58] and inverse Rashba-Edelstein effect (spin galvanic effect) [59], can be used for electrical spin detection as they convert spin into charge current. These charge–spin interconversion (CSI) effects enable FM-free spin injection and detection.

Furthermore, SOC might be employed to control the flow of spins through the channel with an external electric field [60], as originally proposed by Datta and Das [61]. In their proposal of the electronic analogue of the electro-optic modulator, a gate voltage modulates the strength of SOC that rotates the diffusing spins. Graphene with enhanced SOC is envisioned as a promising material for achieving spin-logic devices.

For these reasons, a finite gate-tunable SOC in graphene is desirable as it would provide the means to perform all the basic operations of an active spintronic device, i.e. injection, manipulation, and detection of spins. Excitingly, a sizeable SOC can be

induced in graphene through proximity-induced effects [62, 63]. Proximity effects refer to short-range interactions across the interfaces of materials in heterostructures, where properties of one material are transferred to another. The atomically-thin nature of 2DMs promotes proximity effects and their layered nature allows for direct assembly in van der Waals (vdW) heterostructures in a Lego-like manner.

In recent years, proximity-induced SOC [64, 65], magnetism [66, 67], and superconductivity [68] have been demonstrated in heterostructures made of various 2DMs. Proximity-SOC in graphene is achieved by interfacing it with high-SOC materials, such as transition metal dichalcogenides (TMDCs) [64, 65] and topological insulators [69] and demonstrated through weak antilocalisation experiments [70], nonlocal measurements probing spin relaxation anisotropy [64, 65, 71], and CSI phenomena [55, 72–74].

Measuring spin relaxation anisotropy through (nonlocal) spin precession experiments is a powerful method to investigate spin transport and dynamics in graphene [75, 76]. In these measurements, spin lifetimes along different spatial directions are identified which provides key information on the nature of the induced SOC (e.g. persistent spin texture, Rashba winding spin texture, etc). CSI measurements are mainly performed to measure the spin-charge conversion efficiency, i.e. the spin Hall angle, of various materials and heterostructures. Large spin Hall angles are required to achieve practical applications of spintronic devices. In addition, certain insight into the nature of SOC in graphene can be obtained with these measurements by taking into consideration the symmetries of the present CSI phenomena [77].

Recently, low-symmetry 2DMs attracted attention of the spintronics community [78–81] due to the possibility of generating unconventional CSI components [82] and inducing novel types of SOC in graphene [63]. These discoveries broaden the range of possible device architectures for spintronic applications. Therefore, understanding and mastering the control of SOC in graphene is crucial step towards the development of active 2D spintronic devices.

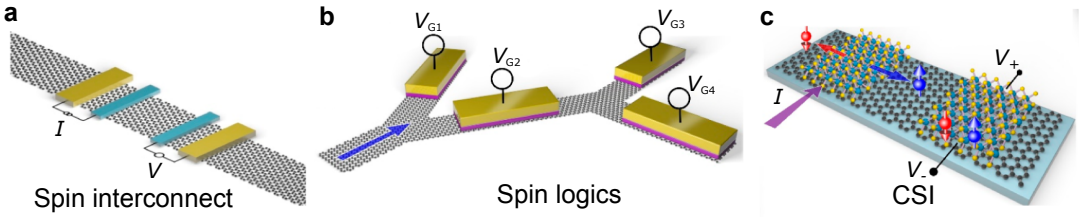


**Fig. 1.1:** Graphene spintronics. **a.** Lateral graphene spin valve for spin communication. **b.** Spin-logic device based on graphene demultiplexer and SOC-modulating logical gates. **c.** Charge-spin interconversion in the graphene region where SOC is enhanced by proximity effect. Adapted from Ref. [83].

## 1.4 Thesis outline

In this thesis, I investigate spin transport in heterostructures of graphene and low-symmetry TMDCs that induce a sizeable SOC in graphene through proximity effects.

The low symmetry of these heterostructures leads to the emergence of novel types of proximity-induced SOC in graphene. Such SOC is studied through a series of measurements based on spin relaxation anisotropy and CSI experiments. The structure and content of the thesis is as follows:

- This chapter briefly presents limits to transistor scaling, spintronics as a technology capable of extending Moore's law, and graphene spintronics as a promising research direction to achieve spin-logic components.
- Chapter 2 presents the background on the physical phenomena and materials explored in this thesis. It begins with an introduction to quantum mechanical spin, spin-orbit coupling, and the general concepts of spin transport, spin relaxation, and charge to spin interconversion phenomena. Then, selected van der Waals materials are presented, followed by a description of spin transport in both pristine and proximitized graphene.
- Chapter 3 introduces the experimental design employed in this thesis, starting with the concept of spin injection, detection, and precession under an out-of-plane, in-plane, and oblique magnetic field in lateral spin devices. Finally, the device geometries for characterising the spin relaxation anisotropy and the CSI are described.
- Chapter 4 introduces the device fabrication steps and the used characterisation methods.
- Chapter 5 describes the modelling of spin transport. The solution of the Bloch diffusion equation is derived for the case of a partially proximitized graphene spin valve. The spin density across anisotropic samples is calculated and simulations of precession curves are presented for different magnetic field configurations. The lineshape dependence of the curves on various geometric and spin transport parameters is investigated.
- Chapter 6 presents an experimental demonstration of anisotropic spin dynamics in low-symmetry graphene/$PdSe_2$ heterostructures. Large in-plane spin relaxation anisotropy is observed, indicating the presence of a novel SOC in graphene/$PdSe_2$. In addition, the anisotropy is shown to be highly tunable by an electric field, paving the way for gate-tunable spin transport devices.
- Chapter 7 first proposes a protocol based on multilateral spin precession experiments to disentangle spin currents and spin densities, induced by the SHE and ISGE, respectively. The chapter demonstrates the possibility of generating spins with polarisation components in all three spatial directions through CSI in a low-symmetry graphene/$WTe_2$ heterostructure.
- Finally, Chapter 8 provides conclusions of the thesis and recommendations for future work.

## References


[1] J. Bardeen and W. H. Brattain; "The Transistor, A Semi-Conductor Triode". *Physical Review* 1948**, 74**, pp. 230–231. DOI: 10.1103/PhysRev.74.230.

[2] H. Iwai. "The First MOSFET Design by J. Lilienfeld and its Long Journey to Implementation" (2023), pp. 65–88. URL: https://onlinelibrary.wiley.com/doi/abs/10.1002/9781394202478.ch7.

[3] M. M. Atalla. "Semiconductor triode". U.S. pat. 3056888A. B. T. L. Inc. Oct. 2, 1962. URL: https://patents.google.com/patent/US3056888A/en.

[4] D. Kahng. "Electric field controlled semiconductor device". U.S. pat. 3102230A. B. T. L. Inc. Aug. 27, 1963. URL: https://patents.google.com/patent/US3102230A/en.

[5] J. S. Kilby. "Miniature semiconductor integrated circuit". U.S. pat. 3115581A. T. I. Inc. Dec. 24, 1963. URL: https://patents.google.com/patent/US3115581A/en.

[6] R. N. Noyce. "Semiconductor device-and-lead structure". U.S. pat. 2981877A. F. S. Corp. Apr. 25, 1961. URL: https://patents.google.com/patent/US2981877A/en.

[7] G. Moore; "Cramming More Components Onto Integrated Circuits". *Proceedings of the IEEE* 1998**, 86**, pp. 82–85. DOI: 10.1109/JPROC.1998.658762.

[8] L. Rodgers et al.; *Inside the miracle of modern chip manufacturing*. *Financial Times*. Feb. 24, 2024. URL: https://ig.ft.com/microchips/.

[9] I. L. Markov; "Limits on fundamental limits to computation". *Nature* 2014**, 512**, pp. 147–154. DOI: 10.1038/nature13570.

[10] R. Dennard et al.; "Design of ion-implanted MOSFET's with very small physical dimensions". *IEEE Journal of Solid-State Circuits* 1974**, 9**, pp. 256–268. DOI: 10.1109/JSSC.1974.1050511.

[11] D. Frank et al.; "Device scaling limits of Si MOSFETs and their application dependencies". *Proceedings of the IEEE* 2001**, 89**, pp. 259–288. DOI: 10.1109/5.915374.

[12] B. Doyle et al.; "Transistor Elements for 30nm Physical Gate Lengths and Beyond." *Intel Technology Journal* 2002**, 6**, p. 42.

[13] M. Dayarathna, Y. Wen, and R. Fan; "Data Center Energy Consumption Modeling: A Survey". *IEEE Communications Surveys & Tutorials* 2016**, 18**, pp. 732–794. DOI: 10.1109/COMST.2015.2481183.

[14] D. E. Nikonov and I. A. Young; "Overview of Beyond-CMOS Devices and a Uniform Methodology for Their Benchmarking". *Proceedings of the IEEE* 2013**, 101**, pp. 2498–2533. DOI: 10.1109/JPROC.2013.2252317.

[15] G. Fiori et al.; "Electronics based on two-dimensional materials". *Nature Nanotechnology* 2014**, 9**, pp. 768–779. DOI: 10.1038/nnano.2014.207.

[16] P. Avouris et al.; "Carbon nanotube electronics". *Proceedings of the IEEE* 2003**, 91**, pp. 1772–1784. DOI: 10.1109/JPROC.2003.818338.

[17] R. L. Carroll and C. B. Gorman; "The Genesis of Molecular Electronics". *Angewandte Chemie International Edition* 2002**, 41**, pp. 4378–4400. DOI: 10.1002/1521-3773(20021202)41:23<4378::AID-ANIE4378>3.0.CO;2-A.

[18] N. Setter et al.; "Ferroelectric thin films: Review of materials, properties, and applications". *Journal of Applied Physics* 2006**, 100**, p. 051606. DOI: 10.1063/1.2336999.

[19] J. F. Scott; "Applications of Modern Ferroelectrics". *Science* 2007**, 315**, pp. 954–959. DOI: 10.1126/science.1129564.

[20] D. Go et al.; "Orbitronics: Orbital currents in solids". *EPL (Europhysics Letters)* 2021**, 135**, p. 37001. DOI: 10.1209/0295-5075/ac2653.

[21] J. R. Schaibley et al.; "Valleytronics in 2D materials". *Nature Reviews Materials* 2016**, 1**, pp. 1–15. DOI: 10.1038/natrevmats.2016.55.

[22] S. A. Vitale et al.; "Valleytronics: Opportunities, Challenges, and Paths Forward". *Small* 2018**, 14**, p. 1801483. DOI: 10.1002/smll.201801483.

[23] I. Žutić, J. Fabian, and S. Das Sarma; "Spintronics: Fundamentals and applications". *Reviews of Modern Physics* 2004**, 76**, pp. 323–410. DOI: 10.1103/RevModPhys.76.323.

[24] A. Hirohata et al.; "Review on spintronics: Principles and device applications". *Journal of Magnetism and Magnetic Materials* 2020**, 509**, p. 166711. DOI: 10.1016/j.jmmm.2020.166711.

[25] A. Steane; "Quantum computing". *Rept. Prog. Phys.* 1998**, 61**, pp. 117–173. DOI: 10.1088/0034-4885/61/2/002.

[26] P. L. McMahon; "The physics of optical computing". *Nature Reviews Physics* 2023**, 5**, pp. 717–734. DOI: 10.1038/s42254-023-00645-5.

[27] D. Marković et al.; "Physics for neuromorphic computing". *Nature Reviews Physics* 2020**, 2**, pp. 499–510. DOI: 10.1038/s42254-020-0208-2.

[28] E. D. Daniel, C. D. Mee, and M. H. Clark; *Magnetic Recording: The First 100 Years*, 1998.

[29] R. H. Dee; "Magnetic Tape for Data Storage: An Enduring Technology". *Proceedings of the IEEE* 2008**, 96**, pp. 1775–1785. DOI: 10.1109/JPROC.2008.2004311.

[30] B. Bhushan; "Current status and outlook of magnetic data storage devices". *Microsystem Technologies* 2023**, 29**, pp. 1529–1546. DOI: 10.1007/s00542-023-05549-z.

[31] M. N. Baibich et al.; "Giant Magnetoresistance of (001)Fe/(001)Cr Magnetic Superlattices". *Physical Review Letters* 1988**, 61**, pp. 2472–2475. DOI: 10.1103/PhysRevLett.61.2472.

[32] G. Binasch et al.; "Enhanced magnetoresistance in layered magnetic structures with antiferromagnetic interlayer exchange". *Physical Review B* 1989**, 39**, pp. 4828–4830. DOI: 10.1103/PhysRevB.39.4828.

[33] E. E. Fullerton and J. R. Childress; "Spintronics, Magnetoresistive Heads, and the Emergence of the Digital World". *Proceedings of the IEEE* 2016**, 104**, pp. 1787–1795. DOI: 10.1109/JPROC.2016.2567778.

[34] B.-Y. Jiang et al.; "Tunneling magnetoresistive devices as read heads in hard disk drives". *Journal of Magnetism and Magnetic Materials* 2023**, 571**, p. 170546. DOI: 10.1016/j.jmmm.2023.170546.

[35] B. Engel et al.; "A 4-Mb toggle MRAM based on a novel bit and switching method". *IEEE Transactions on Magnetics* 2005**, 41**, pp. 132–136. DOI: 10.1109/TMAG.2004.840847.

[36] M. Hosomi et al. "A novel nonvolatile memory with spin torque transfer magnetization switching: spin-ram". In: *IEEE InternationalElectron Devices Meeting, 2005. IEDM Technical Digest.* IEEE InternationalElectron Devices Meeting, 2005. IEDM Technical Digest. Dec. 2005, pp. 459–462. DOI: 10.1109/IEDM.2005.1609379.

[37] V. Krizakova et al.; "Spin-orbit torque switching of magnetic tunnel junctions for memory applications". *Journal of Magnetism and Magnetic Materials* 2022**, 562**, p. 169692. DOI: 10.1016/j.jmmm.2022.169692.

[38] T. Nozaki et al.; "Recent Progress in the Voltage-Controlled Magnetic Anisotropy Effect and the Challenges Faced in Developing Voltage-Torque MRAM". *Micromachines* 2019**, 10**, p. 327. DOI: 10.3390/mi10050327.

[39] G. Prenat et al. "Beyond STT-MRAM, Spin Orbit Torque RAM SOT-MRAM for High Speed and High Reliability Applications" (2015). Ed. by W. Zhao and G. Prenat, pp. 145–157. URL: https://doi.org/10.1007/978-3-319-15180-9_4.

[40] W. Kang et al. "Voltage-controlled MRAM for working memory: Perspectives and challenges". In: *Design, Automation & Test in Europe Conference & Exhibition (DATE), 2017*. Design, Automation & Test in Europe Conference & Exhibition (DATE), 2017. Mar. 2017, pp. 542–547. DOI: 10.23919/DATE.2017.7927047.

[41] A. Manchon et al.; "New perspectives for Rashba spin–orbit coupling". *Nature Materials* 2015**, 14**, pp. 871–882. DOI: 10.1038/nmat4360.

[42] Y. Guo et al.; "Quantum materials for spintronic applications". *npj Spintronics* 2024**, 2**, pp. 1–11. DOI: 10.1038/s44306-024-00038-z.

[43] Y. Cao et al.; "Prospect of Spin-Orbitronic Devices and Their Applications". *iScience* 2020**, 23**. DOI: 10.1016/j.isci.2020.101614.

[44] W. Kang, H. Zhang, and W. Zhao. "Spintronic Memories: From Memory to Computing-in-Memory". In: *2019 IEEE/ACM International Symposium on Nanoscale Architectures (NANOARCH)*. 2019 IEEE/ACM International Symposium on Nanoscale Architectures (NANOARCH). July 2019, pp. 1–2. DOI: 10.1109/NANOARCH47378.2019.181298.

[45] B. Behin-Aein et al.; "Proposal for an all-spin logic device with built-in memory". *Nature Nanotechnology* 2010**, 5**, pp. 266–270. DOI: 10.1038/nnano.2010.31.

[46] K. S. Novoselov et al.; "Electric Field Effect in Atomically Thin Carbon Films". *Science* 2004**, 306**, pp. 666–669. DOI: 10.1126/science.1102896.

[47] G. R. Bhimanapati et al.; "Recent Advances in Two-Dimensional Materials beyond Graphene". *ACS Nano* 2015**, 9**, pp. 11509–11539. DOI: 10.1021/acsnano.5b05556.

[48] J. A. Robinson; "Perspective: 2D for beyond CMOS". *APL Materials* 2018**, 6**, p. 058202. DOI: 10.1063/1.5022769.

[49] C. Huyghebaert et al. "2D materials: roadmap to CMOS integration". In: *2018 IEEE International Electron Devices Meeting (IEDM)*. 2018 IEEE International Electron Devices Meeting (IEDM). Dec. 2018, pp. 22.1.1–22.1.4. DOI: 10.1109/IEDM.2018.8614679.

[50] M. C. Lemme et al.; "2D materials for future heterogeneous electronics". *Nature Communications* 2022**, 13**, p. 1392. DOI: 10.1038/s41467-022-29001-4.

[51] Z. M. Gebeyehu et al.; "Spin communication over 30 µm long channels of chemical vapor deposited graphene on $SiO_2$". *2D Materials* 2019**, 6**, p. 034003. DOI: 10.1088/2053-1583/ab1874.

[52] M. Drögeler et al.; "Spin Lifetimes Exceeding 12 ns in Graphene Nonlocal Spin Valve Devices". *Nano Letters* 2016**, 16**, pp. 3533–3539. DOI: 10.1021/acs.nanolett.6b00497.

[53] J. Sinova et al.; "Spin Hall effects". *Reviews of Modern Physics* 2015**, 87**, pp. 1213–1260. DOI: 10.1103/RevModPhys.87.1213.

[54] Q. Shao et al.; "Strong Rashba-Edelstein Effect-Induced Spin–Orbit Torques in Monolayer Transition Metal Dichalcogenide/Ferromagnet Bilayers". *Nano Letters* 2016**, 16**, pp. 7514–7520. DOI: 10.1021/acs.nanolett.6b03300.

[55] T. S. Ghiasi et al.; "Charge-to-Spin Conversion by the Rashba–Edelstein Effect in Two-Dimensional van der Waals Heterostructures up to Room Temperature". *Nano Letters* 2019**, 19**, pp. 5959–5966. DOI: 10.1021/acs.nanolett.9b01611.

[56] I. Garate; "Inverse Spin-Galvanic Effect in the Interface between a Topological Insulator and a Ferromagnet". *Physical Review Letters* 2010**, 104**. DOI: 10.1103/PhysRevLett.104.146802.

[57] L. A. Benítez et al.; "Tunable room-temperature spin galvanic and spin Hall effects in van der Waals heterostructures". *Nature Materials* 2020**, 19**, pp. 170–175. DOI: 10.1038/s41563-019-0575-1.

[58] E. Saitoh et al.; "Conversion of spin current into charge current at room temperature: Inverse spin-Hall effect". *Applied Physics Letters* 2006**, 88**, p. 182509. DOI: 10.1063/1.2199473.

[59] S. D. Ganichev et al.; "Spin-galvanic effect". *Nature* 2002**, 417**, pp. 153–156. DOI: 10.1038/417153a.

[60] J. Nitta et al.; "Gate Control of Spin-Orbit Interaction in an Inverted $In_{0.53}Ga_{0.47}As/In_{0.52}Al_{0.48}As$ Heterostructure". *Physical Review Letters* 1997**, 78**, pp. 1335–1338. DOI: 10.1103/PhysRevLett.78.1335.

[61] S. Datta and B. Das; "Electronic analog of the electro-optic modulator". *Applied Physics Letters* 1990**, 56**, pp. 665–667. DOI: 10.1063/1.102730.

[62] M. Gmitra and J. Fabian; "Graphene on transition-metal dichalcogenides: A platform for proximity spin-orbit physics and optospintronics". *Physical Review B* 2015**, 92**, p. 155403. DOI: 10.1103/PhysRevB.92.155403.

[63] M. Milivojevic et al.; "Giant asymmetric proximity-induced spin–orbit coupling in twisted graphene/SnTe heterostructure". *2D Materials* 2024**, 11**, p. 035036. DOI: 10.1088/2053-1583/ad59b4.

[64] T. S. Ghiasi et al.; "Large Proximity-Induced Spin Lifetime Anisotropy in Transition-Metal Dichalcogenide/Graphene Heterostructures". *Nano Letters* 2017**, 17**, pp. 7528–7532. DOI: 10.1021/acs.nanolett.7b03460.

[65] L. A. Benítez et al.; "Strongly anisotropic spin relaxation in graphene–transition metal dichalcogenide heterostructures at room temperature". *Nature Physics* 2018**, 14**, pp. 303–308. DOI: 10.1038/s41567-017-0019-2.

[66] B. Huang et al.; "Emergent phenomena and proximity effects in two-dimensional magnets and heterostructures". *Nature Materials* 2020**, 19**, pp. 1276–1289. DOI: 10.1038/s41563-020-0791-8.

[67] T. S. Ghiasi et al.; "Electrical and thermal generation of spin currents by magnetic bilayer graphene". *Nature Nanotechnology* 2021**, 16**, pp. 788–794. DOI: 10.1038/s41565-021-00887-3.

[68] C. Huang et al.; "Inducing Strong Superconductivity in $WTe_2$ by a Proximity Effect". *ACS Nano* 2018**, 12**, pp. 7185–7196. DOI: 10.1021/acsnano.8b03102.

[69] K. Song et al.; "Spin Proximity Effects in Graphene/Topological Insulator Heterostructures". *Nano Letters* 2018**, 18**, pp. 2033–2039. DOI: 10.1021/acs.nanolett.7b05482.

[70] S. Zihlmann et al.; "Large spin relaxation anisotropy and valley-Zeeman spin-orbit coupling in $WSe_2$/graphene/*h*-BN heterostructures". *Physical Review B* 2018**, 97**, p. 075434. DOI: 10.1103/PhysRevB.97.075434.

[71] J. Ingla-Aynés et al.; "Electrical Control of Valley-Zeeman Spin-Orbit-Coupling–Induced Spin Precession at Room Temperature". *Physical Review Letters* 2021**,** **127**, p. 047202. DOI: 10.1103/PhysRevLett.127.047202.

[72] C. K. Safeer et al.; "Room-Temperature Spin Hall Effect in Graphene/$MoS_2$ van der Waals Heterostructures". *Nano Letters* 2019**,** **19**, pp. 1074–1082. DOI: 10.1021/acs.nanolett.8b04368.

[73] F. Herling et al.; "Gate tunability of highly efficient spin-to-charge conversion by spin Hall effect in graphene proximitized with $WSe_2$". *APL Materials* 2020**,** **8**, p. 071103. DOI: 10.1063/5.0006101.

[74] H. Yang et al.; "Twist-angle-tunable spin texture in $WSe_2$/graphene van der Waals heterostructures". *Nature Materials* 2024, pp. 1–7. DOI: 10.1038/s41563-024-01985-y.

[75] B. Raes et al.; "Determination of the spin-lifetime anisotropy in graphene using oblique spin precession". *Nature Communications* 2016**,** **7**, p. 11444. DOI: 10.1038/ncomms11444.

[76] L. A. Benítez et al.; "Investigating the spin-orbit interaction in van der Waals heterostructures by means of the spin relaxation anisotropy". *APL Materials* 2019**,** **7**, p. 120701. DOI: 10.1063/1.5124894.

[77] L. Camosi et al.; "Resolving spin currents and spin densities generated by charge-spin interconversion in systems with reduced crystal symmetry". *2D Materials* 2022**,** **9**, p. 035014. DOI: 10.1088/2053-1583/ac6fec.

[78] B. Zhao et al.; "Unconventional Charge–Spin Conversion in Weyl-Semimetal $WTe_2$". *Advanced Materials* 2020**,** **32**, p. 2000818. DOI: 10.1002/adma.202000818.

[79] M. Vila et al.; "Low-symmetry topological materials for large charge-to-spin interconversion: The case of transition metal dichalcogenide monolayers". *Physical Review Research* 2021**,** **3**, p. 043230. DOI: 10.1103/PhysRevResearch.3.043230.

[80] J. Ingla-Aynés et al.; "Omnidirectional spin-to-charge conversion in graphene/$NbSe_2$ van der Waals heterostructures". *2D Materials* 2022**,** **9**, p. 045001. DOI: 10.1088/2053-1583/ac76d1.

[81] N. Ontoso et al.; "Unconventional Charge-to-Spin Conversion in Graphene/$MoTe_2$ van der Waals Heterostructures". *Physical Review Applied* 2023**,** **19**, p. 014053. DOI: 10.1103/PhysRevApplied.19.014053.

[82] A. Roy, M. H. D. Guimarães, and J. Sławińska; "Unconventional spin Hall effects in nonmagnetic solids". *Physical Review Materials* 2022**,** **6**, p. 045004. DOI: 10.1103/PhysRevMaterials.6.045004.

[83] J. F. Sierra et al.; "Van der Waals heterostructures for spintronics and opto-spintronics". *Nature Nanotechnology* 2021**,** **16**, pp. 856–868. DOI: 10.1038/s41565-021-00936-x.

# Chapter 2

# Theoretical background

This chapter introduces the theory of the physical phenomena investigated in this thesis. The chapter begins by introducing the concept of quantum mechanical spin and its mathematical framework. It then delves into spin–orbit coupling, spin transport, spin relaxation, and charge–spin interconversion phenomena. Subsequent sections provide an overview of van der Waals and two-dimensional (2D) materials. Finally, the chapter discusses spin transport in graphene and proximitized graphene.

## 2.1 Electron spin

A seminal work that shed light on the existence of an electron's spin was the Stern-Gerlach experiment [1] conducted in 1922, three years before Heisenberg [2], Born, and Jordan [3] defined modern quantum mechanics. In the Stern-Gerlach experiment, a beam of silver atoms is sent through an inhomogeneous magnetic field that acts on their magnetic moments and deflects their trajectories. If the atoms behaved as classical magnets, the magnetic field acting on their randomly orientated magnetic moments would cause continuous spreading around the central undeflected beam. However, the atomic beam splits and forms two lines on the detector screen. Thus, the result suggests the existence of quantised intrinsic angular momentum (spin) that is resolved to be either spin-up or spin-down, when passing through the inhomogeneous magnetic field.

Another experimental result hinting at the existence of spin was the observation of spectral line splitting in atomic spectra, as demonstrated by the Zeeman effect.. When investigating atomic spectra in strong magnetic fields, the actual number of observed electron states in the atom was twice the expected number predicted by the then-prevailing Bohr-Sommerfeld model. Trying to grapple with the anomaly, namely the doublet structure of the alkali spectra, Pauli realised that the phenomenon could be understood if the electron had a new quantum property that would take two values [4]. Although discussed by other physicists (e.g. Compton [5]), the idea of a spinning electron was pushed forward by Uhlenbeck and Goudsmit [6, 7] to give a classical physical explanation. Assuming the existence of a magnetic moment of an electron allowed them to explain the fine structure of the atomic spectra qualitatively. The correct quantitative explanation was provided by Thomas [8]. Pauli, deeply

discontent with the classical image, redefined the spin angular momentum in terms of the quantum-mechanical operator

$$\hat{S} = \frac{\hbar}{2}\,\vec{\sigma}_s\,, \tag{2.1}$$

where $\hbar$ is the reduced Planck constant and $\vec{\sigma}_s = (\sigma_x\,,\ \sigma_y\,,\ \sigma_z)$ is a vector containing Pauli matrices

$$\sigma_x = \begin{pmatrix} 0 & 1 \\ 1 & 0 \end{pmatrix}\ ; \qquad \sigma_y = \begin{pmatrix} 0 & -i \\ i & 0 \end{pmatrix}\ ; \qquad \sigma_z = \begin{pmatrix} 1 & 0 \\ 0 & -1 \end{pmatrix} \tag{2.2}$$

and derived his equation that describes spin-1/2 particles in a non-relativistic limit [9]:

$$\left[\frac{1}{2\,m_e}\left(\vec{\sigma}_s\,(\hat{p} - q\,\vec{A})\right)^2 + q\,V\right]|\psi\rangle = i\,\hbar\,\frac{\partial}{\partial t}|\psi\rangle\,, \tag{2.3}$$

where $m_e$ is the electron's rest mass, $\hat{p} = i\,\hbar\,\nabla$ is the momentum operator, $\vec{A}$ is the vector potential, $V$ is the electric scalar potential, and

$$|\psi\rangle = \psi_+|\uparrow\rangle + \psi_-|\downarrow\rangle \tag{2.4}$$

is the quantum state of the system expressed as a two-component spinor wave function.

Finally, Dirac derived the relativistic wave equation for massive fermions [10] and the quantum-mechanical description of the electron (and all 1/2-spin particles) was complete.

## 2.2 Spin–orbit coupling

Spin–orbit coupling (SOC) is a relativistic interaction coupling a particle's spin with its orbital motion. It is responsible for the splitting of the spectral lines in the atomic spectra. In solid-state systems, phenomena such as spin relaxation, the spin Hall effect [11], anisotropic magnetoresistance [12], magnetic anisotropy [13], and anomalous Hall effect [14, 15] emerge as a result of the SOC's effects on the electronic states. SOC induces phenomena such as spin–orbit torque [16] and spin–momentum locking [17], promising practical applications in data storage, memory, and logic devices. Therefore, understanding and controlling SOC is pivotal for spintronics.

How SOC emerges in an atom can be understood by imagining an electron with its spin magnetic dipole moment orbiting around a nucleus. An electron with charge $e$ forms a closed current loop of a diameter $r$. In the reference frame of the electron, the positively charged nucleus, with an atomic number $Z$ and charge $q = Z\,e$, orbits around the stationary electron. According to the Biot-Savart law, this closed current

loop generates a magnetic field

$$\vec{B}_{SOC} = \frac{\mu_0 \, I}{2\,r} = \frac{Z\,e\,f}{2\,\epsilon_0\,c^2\,r}\,, \tag{2.5}$$

where $\mu_0$ and $\epsilon_0$ is the permeability and permittivity of vacuum, $c$ is the speed of light, $I$ is the current flowing through the loop, and $f$ is the orbital frequency. Since the electron's orbital angular momentum vector is

$$\vec{L} = 2\,\pi\,m_e\,f\,r^2\,, \tag{2.6}$$

we can relate the induced magnetic field and orbital angular momentum

$$\vec{B}_{SOC} = \frac{Z\,e\,\vec{L}}{4\,\pi\,\epsilon_0\,m_e\,c^2\,r^3}\,. \tag{2.7}$$

The resulting magnetic field exerts a torque $\tau_B$ on the spin magnetic dipole moment of the electron

$$\vec{\mu}_s = -\frac{g_s\,e}{2\,m_e}\,\vec{S} = -\frac{g_s\,\mu_B}{\hbar}\,\vec{S}\,, \tag{2.8}$$

where $g_s$ is the electron's $g$-factor, $\mu_B$ is the Bohr magneton, and $\vec{S}$ is the spin angular momentum vector. This torque

$$\tau_B = \vec{B}_{SOC} \times \vec{\mu}_s = -\frac{Z\,e^2\,g_s}{8\,\pi\,\epsilon_0\,m_e^2\,c^2\,r^3}\,\vec{L} \times \vec{S} \tag{2.9}$$

leads to a change in the energy

$$\Delta E_{SOC} = -\vec{\mu}_s \cdot \vec{B}_{SOC} \propto \vec{S} \cdot \vec{L}\,. \tag{2.10}$$

Therefore, the interaction between the spin angular momentum and orbital angular momentum shifts the electron's energy levels in the atom.

According to Eq. 2.7, the SOC strength depends strongly on the radii of the orbiting electrons ($\sim r^3$); therefore, the electrons located in the inner shell experience stronger SOC. The other important parameter is the atomic number $Z$— SOC is small for materials composed of light elements (e.g. graphene, hexagonal boron nitride) and become stronger for materials composed of heavier elements (e.g. transition metal dichalcogenides).

Although the above semi-classical derivation of the atomic SOC is useful to illustrate its origin, its nature is inherently relativistic. The precise description of the SOC effect on a moving electron requires the addition of the following SOC Hamiltonian to the Dirac equation

$$\mathcal{H}_{SOC} = \frac{e\,\hbar}{4\,m_e^2\,c^2\sqrt{1 - v^2/c^2}}\left(\nabla V \times (\hat{p} + e\,\vec{A})\right) \cdot \vec{\sigma}_s\,, \tag{2.11}$$

where $v$ is the electron's velocity. The form of this term depends on the system in question. In crystals, Eq. 2.11 is strongly influenced by symmetry and can manifest itself, for example, as Rashba [18] or Dresselhaus SOC [19] (for details see Sec. 2.4).

## 2.3 Spin transport

As discussed in the previous sections, electrons, which facilitate electrical transport through materials, have spin in addition to charge. In the two-spin channel model of conduction, the charge current $J_c$ can be expressed as a sum of spin-up and spin-down polarised currents ($J_\uparrow$ and $J_\downarrow$)

$$J_c = J_\uparrow + J_\downarrow \,, \tag{2.12}$$

while the pure spin current is defined as

$$J_s = J_\uparrow - J_\downarrow \,. \tag{2.13}$$

In isolated NMs, there is no preferential spin orientation (i.e. $J_\uparrow = J_\downarrow$), and, therefore, the charge current is unpolarised ($J_s = 0$). However, FM materials have different densities of states (DOS) for spin-up carriers ($N_\uparrow$) and spin-down carriers ($N_\downarrow$). The imbalance in spin populations (and perhaps also mobility and scattering) may lead to distinct spin currents in the two channels ($J_\uparrow \neq J_\downarrow$) and the current becomes spin-polarised ($J_s \neq 0$).

Applying a current from an FM into an NM induces spin accumulation and spin splitting at their interface. Spin splitting in energy requires the definition of two spin-dependent electrochemical potentials, $\mu_\uparrow$ and $\mu_\downarrow$. The spin-polarised current is defined as

$$J_{\uparrow(\downarrow)} = D_s \nabla \mu_{\uparrow(\downarrow)} \,, \tag{2.14}$$

where $D_s$ is the spin diffusion constant. The pure spin current can then be expressed as

$$J_s = D_s \nabla \left(\mu_\uparrow - \mu_\downarrow\right) . \tag{2.15}$$

The nonequilibrium population of spin-polarised carriers injected into NM materials diminishes as the carriers diffuses away from the spin injection point. The spin relaxation length or spin diffusion length $\lambda_s$ is a characteristic distance quantifying how far spin information can travel in a material before it dissipates due to spin relaxation processes. Its mathematical expression is derived from the spin diffusion equation

$$\lambda_s = \sqrt{\tau_s \, D_s} \,, \tag{2.16}$$

where $\tau_s$ is the spin relaxation time. Spin relaxation processes, responsible for the randomisation of the spin polarisation, have been extensively studied in various materials, including metals, semiconductors, and superconductors [20–22]. The following section briefly introduces the two of them that are most relevant for graphene:

the Elliott-Yafet and Dyakonov-Perel mechanisms.

## 2.4 Spin relaxation

Understanding spin relaxation mechanisms is crucial in spintronics but also in future quantum technologies. It provides essential information to optimize spin transport properties and to improve quantum information processing by enhancing the coherence time of spin qubits [23].

The ***Elliott-Yafet spin relaxation mechanism*** [24, 25] dominates spin relaxation in systems conserving time-reversal and inversion symmetry, for example, in many metals. In this mechanism, spins may flip during scattering events where SOC allows spins to change orientation as they interact with lattice defects, spin-conserving impurities, and phonons. This is possible due to the mixing of the pure degenerate spin-up $|\uparrow\rangle$ and spin-down $|\downarrow\rangle$ eigenstates by the SOC (Fig. 2.1a). Eigenfunctions describing the perturbed Bloch states, i.e. spin-up band $\Psi_{\vec{k},\Uparrow}(\vec{r})$ and spin-down band $\Psi_{\vec{k},\Downarrow}(\vec{r})$, related to the former by time-reversal symmetry, are linear combinations of different spin functions

$$\begin{aligned}\Psi_{\vec{k},\Uparrow}(\vec{r}) &= [a_{\vec{k}}(\vec{r})|\uparrow\rangle + b_{\vec{k}}(\vec{r})|\downarrow\rangle]\, e^{i\vec{k}\vec{r}} \\ \Psi_{\vec{k},\Downarrow}(\vec{r}) &= [a^*_{\vec{k}}(\vec{r})|\downarrow\rangle - b^*_{\vec{k}}(\vec{r})|\uparrow\rangle]\, e^{-i\vec{k}\vec{r}}\,,\end{aligned} \tag{2.17}$$

where the coefficients $a$ and $b$ have the periodicity of the lattice [26]. The scattering probabilities preserving or flipping spin during a scattering event that changes the momentum $\vec{k} \to \vec{k}'$ are

$$\begin{aligned}P_{|\uparrow\rangle\to|\uparrow\rangle} &\propto |M_{\vec{k},\vec{k}'}|^2\, |a^*_{\vec{k}'}\, a_{\vec{k}}|^2 \\ P_{|\uparrow\rangle\to|\downarrow\rangle} &\propto |M_{\vec{k},\vec{k}'}|^2\, |b^*_{\vec{k}'}\, a_{\vec{k}}|^2\,.\end{aligned} \tag{2.18}$$

The spin-flip probability of single event alone is usually small, however, multiple scattering events eventually lead to a spin flip. As the scattering frequency increases, so does the rate of spin flips, resulting in a linear relationship between the momentum scattering time $\tau_p$ and the spin relaxation time $\tau_s$ (Fig. 2.1c)

$$\tau_s \propto \frac{\tau_p}{P_{|\uparrow\rangle\to|\downarrow\rangle}} \approx \frac{\tau_p}{\langle|b|^2\rangle}\,, \tag{2.19}$$

where $\langle\ \rangle$ denotes the average over the Fermi surface.

The ***Dyakonov-Perel spin relaxation*** [27, 28] occurs in non-centrosymmetric systems. Inversion symmetry breaking, in the presence of SOC, has an important consequence for spin physics. In contrast to inversion-symmetric materials, where the SOC causes only the mixing of the spin-up and spin-down states, in the case of inversion-asymmetric systems, SOC induces a splitting of spin-polarised bands (Fig. 2.1b).

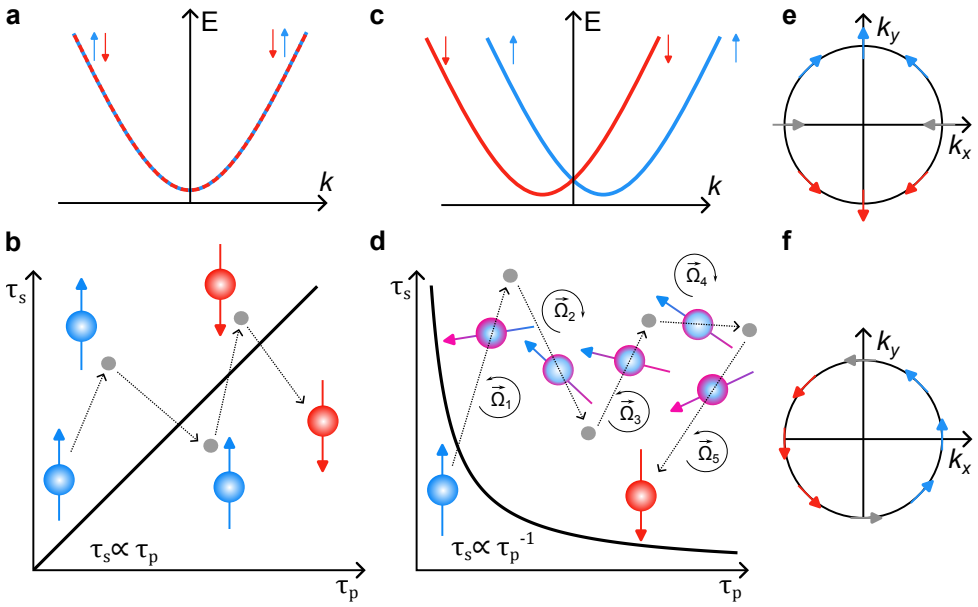


**Fig. 2.1:** Elliott-Yafet/Dyakonov-Perel spin relaxation and spin textures. **a.** In inversion symmetric systems, bands remain spin-degenerate despite SOC. **b.** During Elliott-Yafet spin relaxation, spins sometimes flip randomly, when they encounter scattering centres (grey dots). **c.** If the inversion symmetry is broken, SOC acts on the carriers as an effective magnetic field leading to spin-splitting of the bands. **d.** During Dyakonov-Perel spin relaxation, spins undergo precession between the scattering centres. **e**,**f.** Linear Dresselhaus (**e**) and Rashba (**f**) spin-texture.

The SOC acts on the spin as a $\vec{k}$-dependent effective magnetic field $\vec{\Omega}(\vec{k})$ changing the energy by

$$\mathcal{H}_{SOC} = \frac{\hbar}{2}\,\vec{\Omega}(\vec{k})\,\vec{\sigma}_s\,. \tag{2.20}$$

This results in a $\vec{k}$-dependent Larmor precession that changes every time the spin scatters. As the individual spins of the initially coherent spin population take different paths, and thus feel effective magnetic fields of varying intensity and direction. Momentum scattering resets the precession. Thus, if the momentum scattering time is shorter than the spin precession period, the scattering helps the spin population to remain coherent over a longer time and distance. This gives an inversely proportional relation between $\tau_s$ and $\tau_p$ (Fig. 2.1d)

$$\tau_s \propto \frac{1}{\Omega^2\,\tau_p}\,. \tag{2.21}$$

Experimentally, the investigation of spin transport as a function of temperature $T$ can help distinguish between the Elliot-Yafet and Dyakonov-Perel relaxation mechanisms in systems where momentum scattering dominates, due to the dependence $\tau_p \propto 1/T$. Alternatively, probing changes in spin transport induced by modulating the carrier concentration $n$ may provide insights into spin relaxation.

The specific form of $\vec{\Omega}(\vec{k})$ is strongly dependent on the crystal symmetry. For instance, in zinc-blende III-V semiconductors (such as GaAs or InSb), where bulk

inversion symmetry is broken, the SOC Hamiltonian close to the Γ point has Dresselhaus form [19]. In the case of 2D electron gas, where transport is confined in the $xy$ plane, Dresselhause SOC acquires linear form [29]

$$\mathcal{H}_{D_1} = \gamma_{\mathrm{D}}/\hbar^3 \, \langle k_z^2 \rangle \, (k_y \, \sigma_y - k_x \, \sigma_x) \, , \tag{2.22}$$

where $\gamma_{\mathrm{D}}$ is Dresselhaus SOC strength parameter. Such hamiltonian results in spin polarisation of the Bloch bands (i.e. spin texture) shown in Fig. 2.1e.

Another SOC type commonly emerges at the interfaces of vertical heterostructures, where the out-of-plane inversion symmetry is broken, as proposed by Rashba. In this case, the SOC Hamiltonian takes the following form

$$\mathcal{H}_R = (\lambda_{\mathrm{R}}/\hbar) \, (\vec{z} \times \vec{p}) \cdot \vec{\sigma_s} \, , \tag{2.23}$$

where $\lambda_{\mathrm{R}}$ is Rashba SOC strength parameter [18]. Rashba SOC manifests as a winding spin texture (Fig. 2.1f).

While SOC facilitates spin relaxation, the spin-momentum coupling it induces can act as a steering mechanism to control the direction of spin current and its polarisation through charge–spin interconversion, as introduced in the following section.

## 2.5 Charge–spin interconversion

In 1929, Mott formulated a theory of the asymmetric spin-dependent scattering of an unpolarised electron beam by a central potential, such as that of a heavy nuclei [30]. Later, in 1971, Dyakonov and Perel predicted that such spin-dependent scattering in solid-state systems leads to the generation of a transverse spin current [31, 32]. However, this charge-spin interconversion (CSI) received more attention only after the rediscovery of the effect by Hirsch in 1999 [33]. CSI phenomena have attracted great research interest in the past 20 years and are approaching practical applications in SOT MRAM [34]. CSI is a group of physical phenomena that allows for the conversion of charge to spin and vice versa. In NM materials, it involves two main effects: the spin Hall effect (SHE) and the spin galvanic effect (SGE). Their reciprocal counterparts, the inverse SHE (ISHE) and the inverse SGE (ISGE) are related to the original effects through the Onsager reciprocal relations [35, 36].

During the SHE, spin-dependent changes in the trajectories of charge carriers occur because of SOC, leading to a directed spin current. The sideways deflection arises either from the intrinsic SOC of the crystal (intrinsic SHE) [37] or from localised SOC impurities present in the material (extrinsic SHE) [38].

Two extrinsic SHE mechanisms are skew scattering and side jump. Skew scattering occurs when a gradient of the Zeeman energy exerts a spin-dependent force on electrons as they pass near a charged SOC impurity (Fig. 2.2a). In contrast, side-jump scattering involves a discontinuous spin-dependent deflection of magnitude $\delta$ when

electrons collide with the SOC impurity (Fig. 2.2b). Both mechanisms lead to a transverse spin current perpendicular to the charge current. To increase the magnitude of the extrinsic SHE, heavy metal impurities with strong SOC can be intentionally introduced into a light metal with low intrinsic SOC [39].

The intrinsic SHE is closely connected to the concept of Berry curvature. Electrons develop a spin-dependent anomalous velocity due to the Berry curvature $\vec{\Omega}_n(\vec{k})$

$$\vec{v}_n(\vec{k}) = \frac{1}{\hbar} \nabla E_n(\vec{k}) - \frac{e}{\hbar} \vec{E} \times \vec{\Omega}_n(\vec{k}) \,, \tag{2.24}$$

where $E_n$ is the energy of the electron at the band $n$ and $\vec{E}$ is the electric field. The Berry curvature deflects the trajectories of spin-up and spin-down carriers in opposite directions (Fig. 2.2c).

The intrinsic SHE strongly depends on crystal symmetry. Specifically, materials' space groups dictate the allowed SHE components. In high-symmetry systems, the charge current, spin current, and spin polarisation must be mutually perpendicular ($\vec{J}_c \perp \vec{J}_s \perp \vec{S}$). This is sometimes refer to as the ordinary SHE. However, as the symmetry is reduced, unconventional spin current and spin polarisation components may emerge. Two extreme cases of unconventional SHE are collinear SHE, where $\vec{J}_c \perp \vec{J}_s \parallel \vec{S}$, and longitudinal SHE, where $\vec{J}_c \parallel \vec{J}_s \perp \vec{S}$ [40].

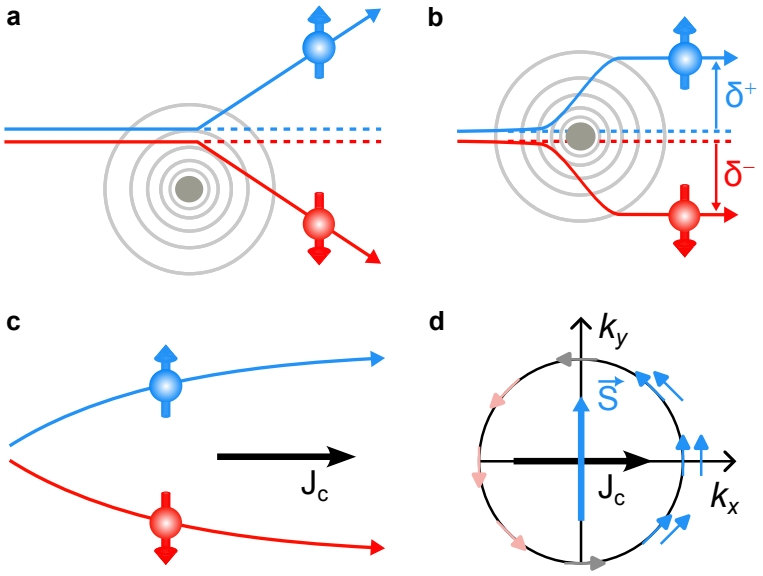


**Fig. 2.2:** Charge-to-spin conversion mechanisms. **a**,**b.** Skew scattering (**a**) and side-jump (**b**) are extrinsic SHE mechanisms involving spin-dependent deflection of electrons from a charged impurity (grey). **c.** Intrinsic SHE emerges due to the effect of Berry curvature. **d.** ISGE in a Rashba system produces spin density perpendicular to the charge current direction.

An important parameter for practical applications is the spin Hall angle, which measures the CSI conversion efficiency and gives a figure of merit to compare the CSI

efficiencies of different materials, and is defined as

$$\Theta_{ij}^{k} = \frac{J_{s,i}^{k}}{J_{c,j}}\,, \tag{2.25}$$

where $J_{s,i}^{k}$ is the spin current in the $\hat{i}$ direction, $J_{c,j}$ is the charge current in the $\hat{j}$ direction, and $\hat{k}$ is the direction of spin polarisation.

The ISGE, also called the Rashba-Edelstein effect [41], occurs in materials with spin-polarised band structure when the Fermi level is tilted by an applied electric field. The accumulation of spins with a specific polarisation can be understood by examining Fig. 2.2d, which represents the case of Rashba SOC at the interface. As the electron momentum and spin polarisation are locked, right-movers ($+k_x$) acquire spin polarisation along $y$ and left-movers ($-k_x$) acquire spin polarisation along $-y$. Therefore, spin density with opposite polarisation accumulates at the interface when the carriers flow in opposite directions. In this simple example, spin polarisation is confined in the $xy$ plane; however, in less symmetric systems, the restrictions on the spin polarisation are relaxed leading to more complex ISGE.

The previous discussion demonstrates that SHE-generated spin currents and ISGE-induced spin densities are often concurrent. Research on vdW heterostructures comprising graphene and both high- and low-symmetry heavy-metal compounds stimulated great enthusiasm in recent years [42–47], due to the combination of large spin Hall angles and the ability of spins to diffuse over long distances while maintaining their polarisation. Resolving spin currents and spin densities in low crystal symmetry systems is addressed in Chapter 7. The experimentally investigated system comprises graphene/$T_d$-$WTe_2$ vdW heterostructure.

## 2.6 Van der Waals materials

Van der Waals (vdW) materials consist of vertically stacked, atomically thin layers that are weakly coupled through van der Waals forces. As shown in Fig. 2.3 atoms within each layer are covalently bonded, and the layers exhibit either a simple planar crystal structure, as in graphite and hexagonal boron nitride (hBN), or a more complex structure, as in the case of transition metal dichalcogenides (TMDCs) including tungsten ditelluride ($WTe_2$) and palladium diselenide ($PdSe_2$), with the latter presenting a puckered crystal structure. The number of vdW materials is virtually limitless, exhibiting diverse behaviours spanning semiconductors, superconductors, semimetals, dielectrics, and, most recently, vdW magnets.

The weak nature of van der Waals (vdW) forces allows the individual sheets forming the vdW stack to peel off. Due to their two-dimensional character, the physical properties of such single-layer materials differ significantly from their three-dimensional counterparts. Indeed, since the isolation of graphene in 2004 [48], research on 2D materials (2DMs) has represented a paradigmatic shift in the field of condensed matter physics.

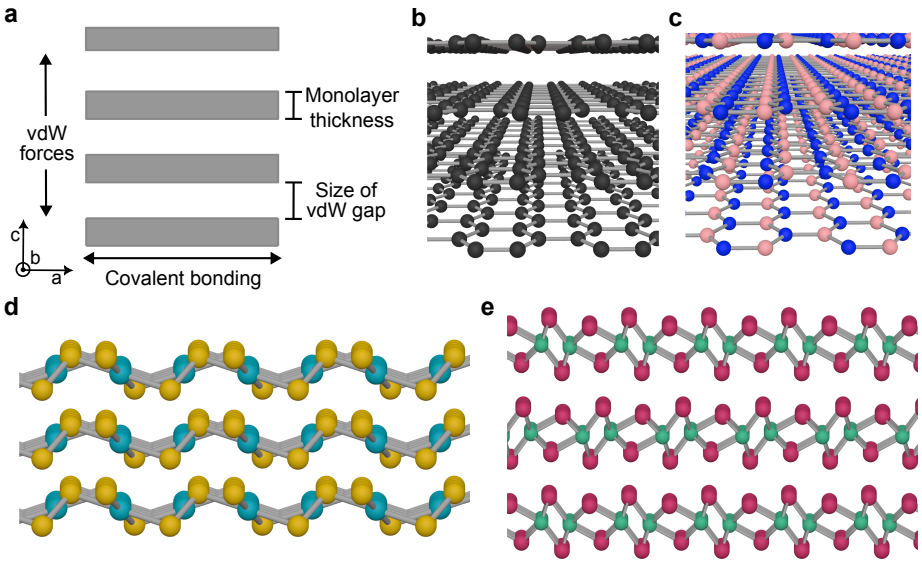


**Fig. 2.3:** Van der Waals materials. **a.** Layered structure of vdW materials. **b.** Graphite is a monoelemental vdW material made of one-atom-thick 2D carbon layers. **c.** Hexagonal boron nitride (hBN) is an isomorph of graphene. **d.** $PdSe_2$ and **e.** $WTe_2$ are examples of TMDCs consisting of 3-atom-thick 2D layers.

It was long assumed that materials could not exist in a stable 2D form due to thermodynamic instability [49]. However, in 2004, A. Geim and C. Novoselov succeeded in exfoliating a single layer of graphite — graphene[48]. The discovery of graphene stimulated significant interest in 2DMs, and soon after, many other vdW crystals were exfoliated into monolayer form[50]. This top-down approach to obtain single-layer materials is widely used for fundamental research in academic laboratories, as it yields high-quality single-crystal 2DMs. However, it has the disadvantage of producing samples with limited lateral dimensions, typically on the order of tens of micrometres. In addition to mechanical exfoliation, considerable progress has been made in developing bottom-up growth methods for high-quality 2DMs, such as chemical vapour deposition (CVD) [51] and molecular beam epitaxy (MBE) [52]. These techniques also enable the synthesis of 2DMs whose bulk counterparts do not exist, such as silicene, germanene, and stanene[53]). These efforts are crucial for applications, particularly in the microelectronics sector, where large-area 2DMs are a prerequisite for industrial-scale device fabrication.

As mentioned earlier, the available material palette is vast, with high-throughput computational methods predicting more than 1800 vdW materials that are potentially exfoliable [54]. The following sections present the materials investigated in this thesis: monolayer graphene and the transition metal dichalcogenides $PdSe_2$ and $WTe_2$.

### 2.6.1 Graphene

Graphene is a single sheet of hexagonally arranged carbon atoms. The honeycomb structure of graphene results from planar $sp^2$ hybridisation between $s$, $p_x$ and $p_y$ orbitals. Such hybridisation leads to the formation of covalent $\sigma$-bonds rotated 120°

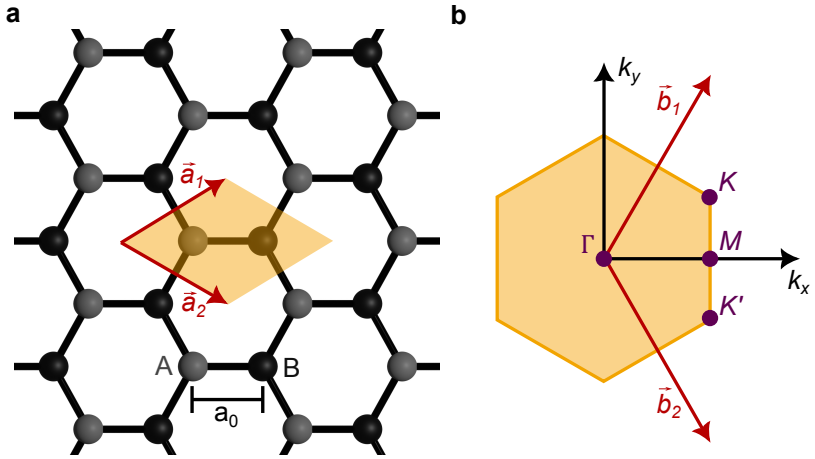


**Fig. 2.4:** Graphene. **a.** Crystal structure (orange rhombus outlines unit cell). **b.** First Brillouin zone in reciprocal space.

degrees to each other that connect the three closest carbon atoms and give graphene its exceptional mechanical strength. Three out of four valence electrons of carbon atoms are employed in the covalent bonding. Due to the full filling of the $\sigma$ bands, they are located deep in the valence band and do not contribute to the electrical properties of graphene. The electronic properties are fully determined by the remaining electrons in $p_z$ orbitals whose lobes are located above and below the graphene sheet and form delocalised (metallic) $\pi$ bonds. Electrons in $p_z$ orbitals can easily hop between neighbouring carbon atoms, making graphene electrically conducting. The valence $\pi$ and conduction $\pi^*$ bands touch at characteristic points in the momentum space $K$ and $K'$, making graphene a semimetal.

Graphene has a triangular Bravais lattice with two atoms per unit cell belonging to sublattices A and B (Fig. 2.4a). Each sublattice point of one kind is surrounded by three sublattice points of the other kind. The lattice vectors $\vec{a}_1$ and $\vec{a}_2$ are

$$\vec{a}_1 = \frac{a_0}{2}(3, \sqrt{3}) \, ; \qquad \vec{a}_2 = \frac{a_0}{2}(3, -\sqrt{3}) \, , \tag{2.26}$$

where $a_0 = 0.142$ nm is the carbon-carbon distance. Reciprocal lattice vectors are

$$\vec{b}_1 = \frac{2\,\pi}{3\,a_0}(1, \sqrt{3}) \, ; \qquad \vec{b}_2 = \frac{2\,\pi}{3\,a_0}(1, -\sqrt{3}) \, . \tag{2.27}$$

and the positions of $K$, $K'$, and $M$ points in the momentum space (Fig. 2.4b) are

$$\vec{K} = \frac{2\,\pi}{3\,a_0}\left(1, \frac{1}{\sqrt{3}}\right) ; \qquad \vec{K}' = \frac{2\,\pi}{3\,a_0}\left(1, -\frac{1}{\sqrt{3}}\right) ; \qquad \vec{M} = \frac{2\,\pi}{3\,a_0}(1, 0) \, . \tag{2.28}$$

The electronic dispersion relation can be derived using the tight-binding approximation [55]. Assuming only the nearest neighbour hopping $t \approx 2.8$ eV and second nearest neighbour hopping $0.02\,t \lesssim t' \lesssim 0.2\,t$, the energy bands are defined by [56]

$$E_{\pm}(\vec{k}) = \pm t \, \sqrt{3 + f(\vec{k})} - t' \, f(\vec{k}) \, , \tag{2.29}$$

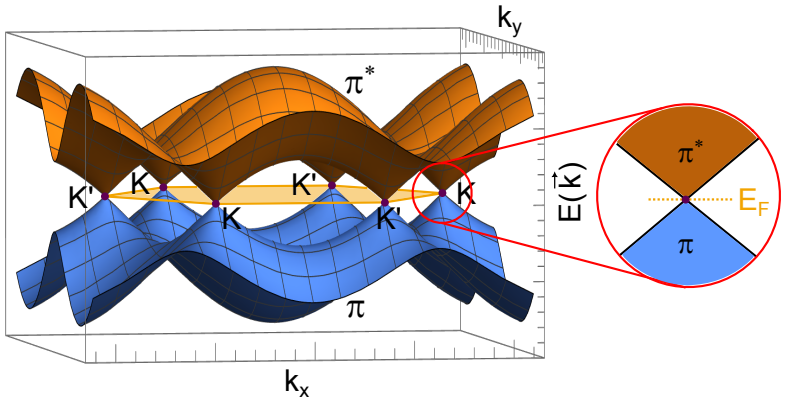


**Fig. 2.5:** Electronic bands of graphene consist of six pairs of Dirac cones per Brillouin zone (left). One pair of Dirac cones is zoomed (right).

where $+$ $(-)$ marks the $\pi^*$ $(\pi)$ band and

$$f(\vec{k}) = 2\cos\left(\sqrt{3}\,k_y\,a_0\right) + 4\cos\left(\frac{\sqrt{3}}{2}\,k_y\,a_0\right)\cos\left(\frac{3}{2}\,k_x\,a_0\right). \tag{2.30}$$

A nonzero value of $t'$ induces a small electron-hole asymmetry in the spectrum. The Hamiltonian for states near the $K$ and $K'$ points is

$$\mathcal{H}_0 = \hbar\,v_{\mathrm{F}}\,(\kappa\,\sigma_x\,k_x + \sigma_y\,k_y)\,, \tag{2.31}$$

where $\kappa = +1\,(-1)$ at $K\,(K')$, $v_{\mathrm{F}}$ is the Fermi velocity

$$v_{\mathrm{F}} = \frac{3\,a_o\,t}{2\,\hbar} \approx 10^6\ \mathrm{m/s}\,, \tag{2.32}$$

and $\sigma_x, \sigma_y$ are the Pauli matrices acting on the pseudospin space formed by the two triangular sublattices. Interestingly, the electronic structure of graphene shows linear rather than parabolic band dispersion close to the $K$ and $K'$ points (Fig. 2.5), and charge transport is governed by the massless Dirac equation. The carrier mobility $\mu$ near the charge neutrality point (CNP), where the $\pi$ and $\pi^*$ conical bands touch, is extremely high exceeding $10^5$ cm$^2$ V$^{-1}$ s$^{-1}$ under ideal conditions (flat substrate, minimal surface contamination) at room temperature [57, 58]. In addition, the Dirac cone electronic structure gives graphene a unique ambipolar characteristic. In contrast to conventional semiconductors where conduction is usually limited to one carrier type with mobilities in the range $\sim 10^3$-$10^4$ cm$^2$ V$^{-1}$ s$^{-1}$, the electronic conduction in graphene can be switched between electrons ($e^-$) and holes ($h^+$) under an external electric field. Despite these exceptional properties, graphene's gapless nature prohibits its use as a transistor because of the associated small on-off ratio.

For spintronic applications, the weak intrinsic SOC and the lack of hyperfine interaction ensure that spins propagate coherently through the crystal lattice over long distances [59]. However, these properties also make controlling and manipulating spins in pristine graphene impossible. Nevertheless, owing to their atomically thin

nature, when combined with other 2DMs that inherently exhibit large SOC, it is possible to imprint such properties in graphene through proximity-induced effects. One of the central ideas of this thesis is to investigate spin transport and spin-charge interconversion phenomena in hybrid systems that combine graphene with 2DMs exhibiting strong SOC, specifically TMDCs.

### 2.6.2 Transition metal dichalcogenides

TMDCs have a chemical structure $MX_2$, where $M$ stands for a transition metal (e.g., Nb, Mo, Pd, Ta, W, Re, Pt) and $X$ represents a chalcogen atom (S, Se or Te). Abundant structural phases include the hexagonal (2H) and the trigonal structure (1T); however, other phases of TMDCs exist, such as monoclinic (1T′) and orthorhombic ($T_d$). The rich chemical and structural representation of TMDCs translates into a variety of electronic properties, including semiconducting (e.g. $MoS_2$ and $WSe_2$) [60], semimetallic (e.g. bulk $PdSe_2$, $MoTe_2$ and $T_d$-$WTe_2$) [61–63], and, at low temperatures, superconducting behaviours ($NbSe_2$ and $TaS_2$) [64, 65].

The electronic band structure of TMDCs is highly dependent on their thickness [66]. For example, $WSe_2$ (Fig. 2.6a) and similar 2H-TMDCs are direct band gap semiconductors in the monolayer limit, exhibiting strong photoluminescence. In contrast, the band gap becomes indirect for bilayer and thicker flakes [67, 68]. Other TMDCs, such as $PdSe_2$ and $PtSe_2$, show a transition from semimetals to semiconductors as their thickness is reduced from bulk to a few layers [61, 69]. In addition, $T_d$-$WTe_2$ (Fig. 2.6b), a type-II Weyl semimetal, becomes a 2D topological insulator in the single layer limit [70].

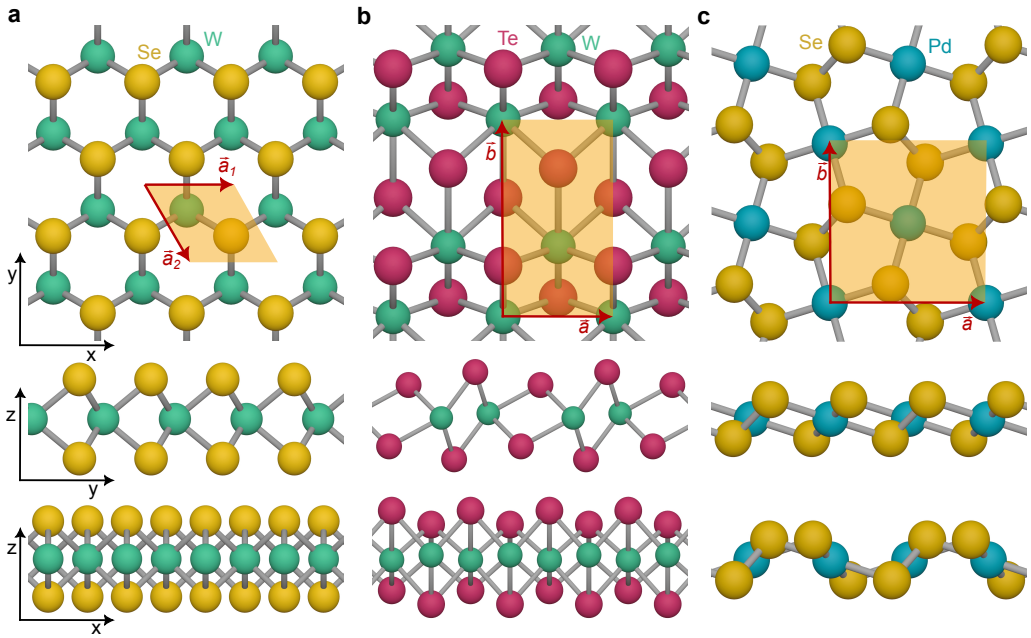


**Fig. 2.6:** Examples of TMDC monolayers with different lattice structures. **a.** Hexagonal $WSe_2$. **b.** $T_d$-$WTe_2$. **c.** Pentagonal $PdSe_2$. Orange areas depict unit cells. The first row shows a top view and the second and third rows show two respective side views.

The high-crystal symmetry 2H-TMDCs have a hexagonal lattice akin to graphene; however, the sublattice points A and B are occupied by $M$ and $X$ atoms, respectively. They have threefold rotational symmetry and are inversion symmetric in the bulk form. In 2H-TMDC monolayers, the inversion symmetry is broken and interesting spin-valley locking emerges due to the strong SOC stemming from $d$-orbitals of the transition metal atoms [71]. The conduction (valence) band minima (maxima) are located at the $K$ and $K'$ points and the bands are spin-polarised out-of-plane with the opposite polarisation at the opposing valleys to preserve time-reversal symmetry [72]. This strong spin-valley locking makes 2H-TMDCs particularly interesting for opto-spintronics [73], as the accumulation of spin-up or spin-down carriers can be generated by circularly-polarised light with opposite helicity [74].

Low-symmetry TMDCs like $T_d$-$WTe_2$ and $T_d$-$MoTe_2$ are noncentrosymmetric even in the bulk form. Therefore, their electronic bands can be spin-polarised. They have recently attracted much attention from the spintronic community due to the large spin Hall angles and the possibility of generating unconventional CSI components [43, 75, 76]. Chapter 7 investigates CSI phenomena in a graphene/$T_d$-$WTe_2$ heterostructure.

In addition, a new class of low-symmetry 2DMs with pentagonal structure has been recently established, promising intriguing properties, such as piezoelectricity, ferroelectricity, negative Poisson's ratio and topological states [77]. The family of TMDCs offers some pentagonal 2DMs, such as $PdS_2$ and $PdSe_2$. They crystallise in the orthorhombic phase and the Se atoms have a tilted square-plane coordination around Pd atoms leading to a buckled structure and unique pentagonal Cairo tiling in the plane (Fig. 2.6c). In bulk, they are inversion symmetric; however, their combination with other 2DMs with distinct crystallography in vdW heterostructures may result in completely symmetry-free interfaces, giving rise to intriguing physical phenomena. Chapter 6 investigates SOC in graphene induced by $PdSe_2$ proximity through spin relaxation anisotropy measurements.

## 2.7 Spin transport in graphene

Out of all known materials, graphene has the longest spin lifetime and spin diffusion length at room temperature. The long $\lambda_s$ is predominantly the consequence of weak intrinsic SOC which has a magnitude of mere $\lambda_I \sim 12$ µeV and opens a band gap with magnitude $2\,\lambda_I$ in the dispersion spectra [78]. The weak nature of intrinsic SOC led to theoretical predictions of $\lambda_s \approx 100$ µm and $\tau_s = 1$ ms for an ideal graphene layer [79]. The intrinsic SOC Hamiltonian $\mathcal{H}_I$ in pristine graphene adds up with the $\mathcal{H}_0$ term in Eq. 2.31 describing linear dispersion, i.e. $\mathcal{H} = \mathcal{H}_0 + \mathcal{H}_I$, where

$$\mathcal{H}_I = \lambda_I \, \sigma_z \, \kappa \, s_z \, . \tag{2.33}$$

Another mechanism that can potentially relax spins is the hyperfine interaction of an electron spin with the nuclear magnetic moment of the $^{13}C$ atoms. However, natural

graphene is predominantly composed of isotope $^{12}C$ (99%) that lacks nuclear spin, therefore, this interaction is negligible. Moreover, a study of artificial (CVD-grown) graphene explicitly composed of the $C^{13}$ isotope has demonstrated that hyperfine interaction does not play an important role in spin relaxation, regardless of the isotope concentration [80].

A free-standing pristine flat graphene sheet is inversion-symmetric, and the Elliott-Yafet mechanism is expected to govern the spin relaxation. However, such a flat graphene sheet cannot exist under real-life conditions, as it is well known that thermal fluctuations lead to the rippling [81]. Thus, even in suspended graphene, the inversion symmetry is slightly broken by the ripples [82]. The rippling leads to spatially varying gauge fields [83] that act on spins as randomly distributed effective out-of-plane magnetic fields [84]. However, the calculated spin relaxation time, caused only by the ripples, is on the order of hundreds of nanoseconds [85], which is in stark contrast to experimentally measured $\tau_s \approx 0.2$ ns in suspended graphene samples [86, 87]. The low $\tau_s$ is somewhat understandable, as sample fabrication is expected to deteriorate the quality of graphene due to the introduction of adatoms and polymer residues.

In disordered graphene, the Elliot-Yafet spin relaxation (see Sec. 2.4) induced by collisions with random spin-independent scatterers (e.g. nonmagnetic impurities, vacancies) was calculated to be quadratically dependent on the position of the Fermi level [26]

$$\tau_s^{\mathrm{EY}} \approx \frac{E_{\mathrm{F}}^2}{\Omega^2}\,\tau_p\,, \tag{2.34}$$

where $\Omega$ is a Rashba-like SOC energy term that splits bands with opposite chirality.

Placing graphene on a substrate mechanically stabilises the 2D sheet, limiting its thermal fluctuations; however, it breaks the out-of-plane inversion symmetry. Thus, graphene experiences a substrate-induced out-of-plane electric field that leads to Rashba SOC

$$\mathcal{H}_R = \frac{\lambda_{\mathrm{R}}}{2}\left(\kappa\,\sigma_x\,s_y - \sigma_y\,s_x\right). \tag{2.35}$$

In most cases, the substrate-induced Rashba field dominates over the curvature-induced gauge fields. Rashba SOC acts on the spins as an effective momentum-dependent in-plane magnetic field. The momentum-dependent spin precession between the scattering events leads to the Dyakonov-Perel spin relaxation (see Sec. 2.4) [84]

$$\tau_s^{\mathrm{DP}} \propto \frac{1}{\Delta^2\,\tau_p}\,. \tag{2.36}$$

Due to the confinement of the Rashba field in the graphene plane, spins are expected to relax anisotropically, with out-of-plane spins relaxing twice as fast as in-plane spins. However, in standard graphene samples on $SiO_2$ substrates, this anisotropy is not observed, implying that other processes dominate the spin relaxation, such as spin interaction with magnetic impurities or random spin-orbit fields (SOFs) and electric potentials [88]. Indeed, an inhomogeneous $SiO_2$ surface leads to

electron-hole puddles in graphene [89], significantly reducing $\tau_s$ [90]. The longest room-temperature spin lifetimes in graphene to date were measured in partially or fully hBN-encapsulated samples, typically reaching several nanoseconds [91–93], underlying the importance of protecting graphene from residues and solvents during sample fabrication.

Such long spin lifetimes and diffusion lengths in clean graphene samples with high carrier mobility make graphene promising for spintronics applications. However, the lack of appreciable SOC in graphene makes it challenging to manipulate the spin, limiting the application of pristine graphene to spin interconnects. Increasing the SOC in graphene, while preserving relatively long $\lambda_s$ and $\tau_s$, would allow electrical injection, detection, and control of the spins paving the way for active spintronic devices. Remarkably, SOC can be engineered in graphene through proximity effects [73].

## 2.8 Spin transport in proximitized graphene

Proximity effects are short-range interactions across interfaces that imprint physical properties absent in the pristine form of the material. They involve the hybridisation of overlapping orbitals and quantum tunnelling of electrons between interface layers. In the case of magnetism and SOC, proximity effects decay exponentially with the distance from the interface; therefore, only properties of a few first atomic layers away from the interface are influenced. In the case of vdW heterostructures, proximity effects are boosted by the atomically thin nature of 2DMs, strongly modifying their properties.

First-principles methods based on density functional theory accurately predicted the possibility of inducing a relatively strong SOC (in the meV range) in graphene by interfacing it with high spin-orbit 2DMs like TMDCs [94–96]. Interfacing graphene with a TMDC breaks the out-of-plane inversion symmetry, leading to the familiar Rashba SOC (Eq. 2.35). Moreover, since the sublattice symmetry of TMDC is broken (sublattice points A and B are occupied by chalcogen and transition metal, respectively), the carbon atoms at different sublattices experience different electrostatic potentials and the sublattice symmetry in graphene is likewise broken. The effective orbital energy difference on A and B sublattices of proximitized graphene opens a gap in the electronic spectrum, and it is described by the staggered potential [94]

$$\mathcal{H}_\Delta = \Delta\, \sigma_z\, s_0\,, \tag{2.37}$$

where $\Delta$ is the proximity-induced gap, $\sigma_z$ is the pseudospin Pauli matrix and $s_0$ is the unit spin matrix. Pseudospin symmetry breaking requires redefining the intrinsic SOC

$$\mathcal{H}_I = \frac{1}{2}\left[\lambda_{\mathrm{I}}^{\mathrm{A}}\,(\sigma_z + \sigma_0) + \lambda_{\mathrm{I}}^{\mathrm{B}}\,(\sigma_z - \sigma_0)\right]\kappa\, s_z\,, \tag{2.38}$$

where $\lambda_{\mathrm{I}}^{\mathrm{A}}$ and $\lambda_{\mathrm{I}}^{\mathrm{B}}$ are intrinsic SOC strength parameters on sublattices A and B, respectively. Breaking the sublattice symmetry in the presence of SOC lifts the spin degeneracy. The change in the Hamiltonian due to the pseudospin inversion asymmetry (PIA) is described by the term [95]

$$\mathcal{H}_{PIA} = \frac{a}{2}\left[\lambda_{\mathrm{PIA}}^{\mathrm{A}}\,(\sigma_z + \sigma_0) + \lambda_{\mathrm{PIA}}^{\mathrm{B}}\,(\sigma_z - \sigma_0)\right](k_x\, s_y - k_y\, s_x)\,, \tag{2.39}$$

where $a = 0.246$ nm is the lattice constant of graphene and $\lambda_{\mathrm{PIA}}^{\mathrm{A}}$ and $\lambda_{\mathrm{PIA}}^{\mathrm{B}}$ are PIA-induced SOC parameters on sublattices A and B, respectively. Both, $\mathcal{H}_I$ and $\mathcal{H}_{PIA}$ describe the nearest-neighbour hopping, but the latter also involves spin-flip. The sum

$$\mathcal{H} = \mathcal{H}_0 + \mathcal{H}_I + \mathcal{H}_R + \mathcal{H}_{PIA} \tag{2.40}$$

describes graphene's bands at $K$ and $K'$. The Eq. 2.40 accurately describes the electronic structure of graphene proximitized with hexagonal 2H-TMDC, such as $MoS_2$, $MoSe_2$, $WS_2$, and $WSe_2$. The magnitude of $\Delta$, $\lambda_{\mathrm{I}}^{\mathrm{A/B}}$ and $\lambda_{\mathrm{PIA}}^{\mathrm{A/B}}$ depends on many parameters, such as the chemical composition of the TMDC and the distance and alignment between the TMDC and the graphene lattices, that is, the twist angle. Thus, the nature and strength of SOC in graphene are highly tunable. Figure 2.7b shows

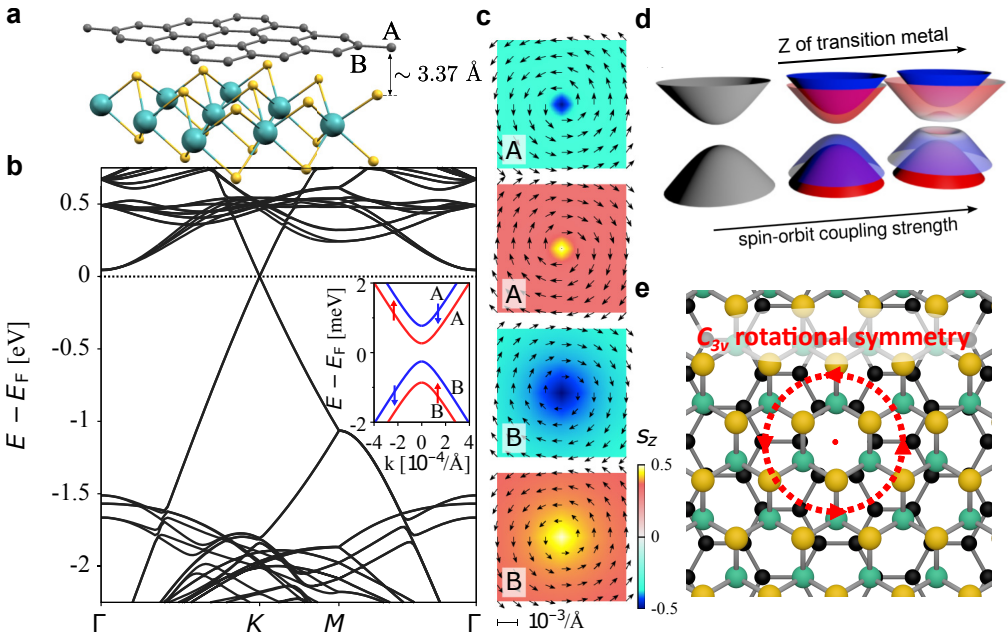


**Fig. 2.7:** Graphene/2H-TMDC heterostructures. **a.** Illustration of a graphene/$MoS_2$ heterostructure. **b.** Its band structure. The inset shows valley-Zeeman SOC-induced splitting of spin bands (fine structure). **c.** Rashba SOC-induced winding spin texture for bands away from $K$ and $K'$ points. **d.** Graphene bands under the influence of valley-Zeeman SOC. As the strength of SOC increases spin degeneracy is lifted and band inversion can occur for large SOC (right). **e.** Graphene/2H-TMDC heterostructures have $\mathcal{C}_{3v}$ rotational symmetry. Adapted from Ref. [94] (**a, b, c**) and Ref. [95] (**d**).

the band structure of a graphene/$MoS_2$ heterostructure. The $E_F$ is located close to the conduction band of $MoS_2$ and crosses the CNP of graphene. The proximity of heavy $d$ orbitals of $MoS_2$ induces energy splitting of the spin bands that is opposite at $K$ and $K'$. This vertical splitting of spin bands, opposite at the two valleys, is called

valley-Zeeman splitting. The valley-Zeeman SOC gives graphene an out-of-plane spin texture (inset of Fig. 2.7b). Since the carriers away from $K$ and $K'$ also experience Rashba SOC, bands have in-plane winding spin-texture (Fig. 2.7c). The strength of proximity-induced SOC in graphene grows with the atomic number $Z$ of the transition metal and, for strong enough SOC ($WSe_2$), it can induce band inversion (Fig. 2.7d).

Another degree of freedom that should be considered, when determining the strength of induced SOC, is the twist angle between graphene and TMDC. Graphene on 2H-TMDCs has threefold rotational symmetry. Fig. 2.7e shows a graphene/2H-TMDC heterostructure for twist angle 30° where the valley-Zeeman SOC is expected to disappear. In contrast, 20° twist angle was calculated to give maximum valley-Zeeman SOC for $MoS_2$ and $MoSe_2$ [97]. Another important consequence of twisting is the emergence of a radial Rashba component that appears for twist angles other than 0° and 30°. The radial Rashba component measures the deviation of spin texture from ordinary tangential orientation and it was predicted to reach up to 40° for a twist angle of 20° in graphene/$MoS_2$ heterostructure [96].

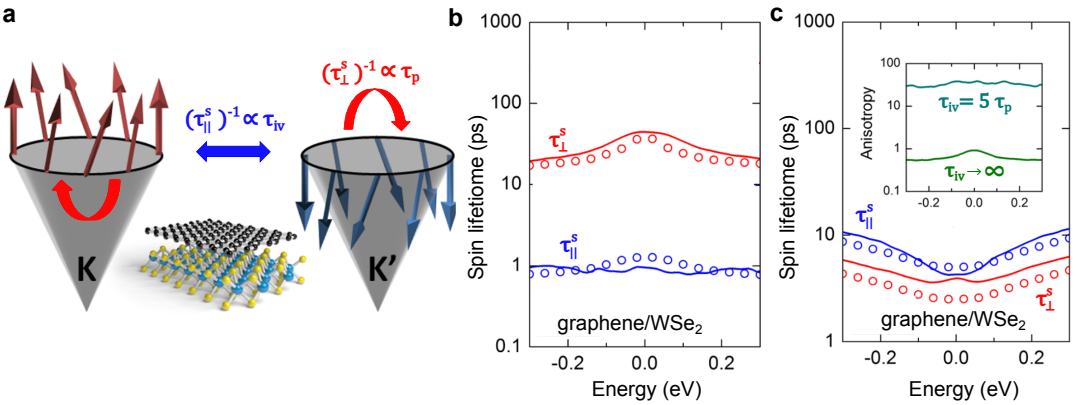


**Fig. 2.8:** Spin relaxation in graphene/2H-TMDC heterostructures. **a.** SOFs at $K$ and $K'$ valleys in graphene/2H-TMDC heterostructure. The in-plane spin lifetime ($\tau_{||}^s$) depends on the intervalley scattering time ($\tau_{iv}$), while the out-of-plane lifetime ($\tau_z^s$) is governed by the momentum scattering time ($\tau_p$). **b.** Spin lifetimes in the strong intervalley scattering regime. **c.** Spin lifetimes without intervalley scattering. Inset shows the resulting spin lifetime anisotropy in the case of strong (top) and weak (bottom) intervalley scattering. Adapted from Ref. [98].

The proximity-induced spin textures described above have strong implications for spin dynamics in graphene, leading to spin lifetime anisotropy, which can be quantified by the ratio between the spin lifetimes for perpendicular and parallel spin components to the graphene plane ($\zeta_{z,||} = \tau_z^s/\tau_{||}^s$). Dyakonov-Perel spin relaxation becomes dominant, as the diffusing spins precess around the strong SOFs and dephase over time. The in-plane spin relaxation remains isotropic ($\tau_x^s = \tau_y^s = \tau_{||}^s$) because the out-of-plane SOFs ($\Omega_z^2$) act equally on all spins in the $xy$ plane and the in-plane Rashba SOFs ($\Omega_x^2$ and $\Omega_y^2$) have a radial symmetry around $K$ and $K'$ points. Importantly, as there are momentum-independent out-of-plane SOFs whose sign depends on the valley, the intervalley scattering time $\tau_{iv}$ becomes a key parameter for correctly determining the spin-lifetime anisotropy.

In a system with intervalley scattering and out-of-plane SOFs, $(\tau_{\parallel}^{s})^{-1} \propto \tau_{\mathrm{iv}}$ and $(\tau_{z}^{s})^{-1} \propto \tau_{p}$ (Fig. 2.8a) and the spin lifetime anisotropy is [98]

$$\zeta_{z,\parallel} = \frac{\tau_{z}^{s}}{\tau_{\parallel}^{s}} = \left(\frac{\lambda_{\mathrm{VZ}}}{\lambda_{\mathrm{R}}}\right)^{2} \left(\frac{\tau_{\mathrm{iv}}}{\tau_{p}}\right) + \frac{1}{2}\,, \tag{2.41}$$

where $\lambda_{\mathrm{VZ}}$ is the valley-Zeeman SOC parameter $\lambda_{\mathrm{VZ}} = (\lambda_{\mathrm{I}}^{\mathrm{A}} - \lambda_{\mathrm{I}}^{\mathrm{B}})/2$. Assuming $\tau_{\mathrm{iv}} \sim 5\,\tau_{p}$ and DFT values of $\lambda_{\mathrm{VZ}} = 1.2$ meV and $\lambda_{\mathrm{R}} = 0.56$ meV, the spin lifetime anisotropy is $\zeta_{z,\parallel} \sim 20$ but depends also on the position of the Fermi level (Fig 2.8b). On the other hand, in the absence of intervalley scattering ($\tau_{\mathrm{iv}} \to \infty$), the spin lifetime anisotropy is reduced to $\zeta_{z,\parallel} = 1/2$ (Fig. 2.8c) as for a standard Rashba 2D electron gas. Proximity-induced SOC in graphene/2H-TMDC heterostructures has been extensively investigated experimentally, showing that the observed spin lifetime anisotropy is driven by such intervalley scattering mechanism [99–101].

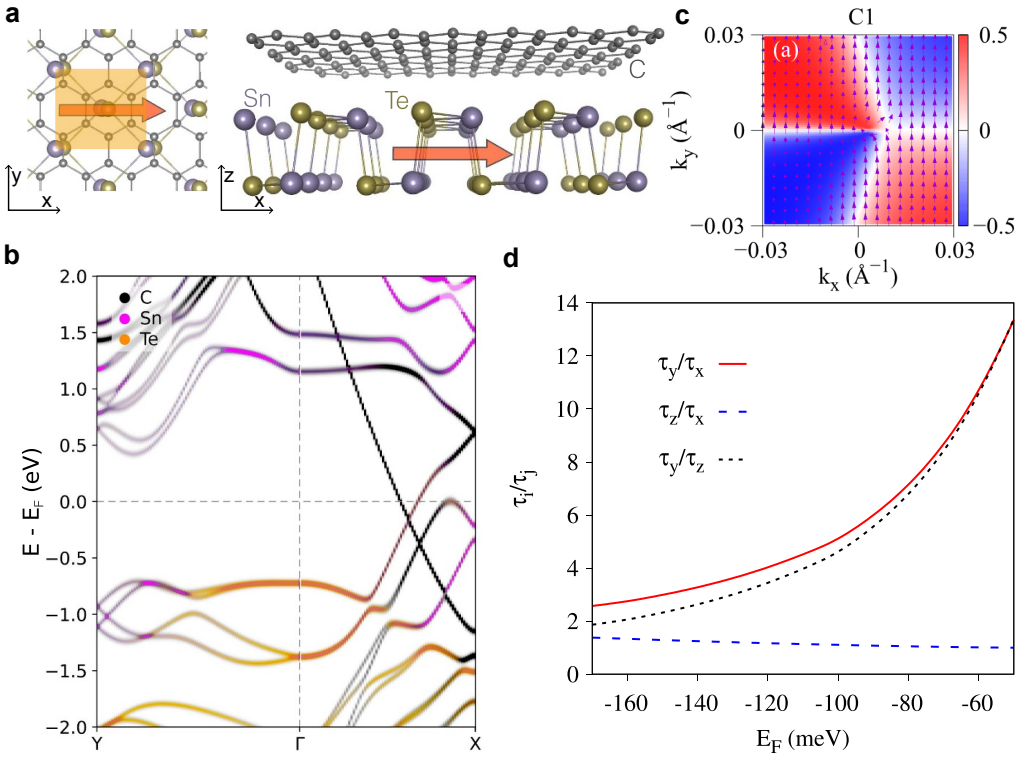


**Fig. 2.9:** Graphene/SnTe low symmetry heterostructure. **a.** Top view (left) and side view (right) of a graphene/SnTe heterostructure. SnTe has a rectangular unit cell and displays pronounced buckling and ferroelectricity (denoted by the orange arrow) along $\hat{x}$. **b.** Calculated band structure of a graphene/SnTe heterostructure showing strong hybridisation of the graphene right-movers' band with SnTe band parallel to it. **c.** Representative spin texture of one spin-split graphene band when proximitized with SnTe. Arrows indicate the persistent spin texture along $\hat{y}$ and the colour scale denotes the $s_z$ component of the SOF. **d.** Spin lifetime anisotropy in graphene/SnTe as a function of Fermi level position. Adapted from Ref. [102].

Although graphene/2H-TMDC heterostructures show spin lifetime anisotropy between in-plane and out-of-plane directions, in-plane lifetimes remain isotropic due to the inherent threefold rotational symmetry ($\mathcal{C}_{3v}$). Lowering the symmetry by combining 2DMs with mutually incompatible lattices could result in anisotropic behaviour

along all three spatial directions, as predicted for graphene/SnTe heterostructures [102]. SnTe has a rectangular lattice and displays pronounced buckling (Fig. 2.9a) and strong in-plane ferroelectricity. Therefore, instead of ordinary in-plane Rashba SOF induced by the out-of-plane electric field, a more complex Rashba SOC can be expected. For an arbitrary twist angle between graphene and SnTe, the gradient of crystal potential $\nabla V(\vec{r})$ has all three spatial components and the Rashba Hamiltonian has to be modified [102]

$$\mathcal{H}_R^* = \sum_{i=0}^{3} \kappa^{\delta_{i,2}} \sigma_i \left[\beta_1^i k_x s_z + \beta_2^i k_y s_z + \lambda_R^i (k_x s_y - k_y s_x)\right], \tag{2.42}$$

where $\delta_{i,2}$ is Kronecker delta function [102] and $\beta_1^i, \beta_2^i, \lambda_R^i$ are pseudospin-dependent Rashba SOC parameters. The interaction $\propto k_x s_z$ and $k_y s_z$ results in unconventional out-of-plane Rashba SOFs. In addition, a strong momentum-independent hybridisation of right-movers of graphene´s Dirac cone with the SnTe bands (Fig. 2.9b) gives rise to persistent spin texture described by the hybridization-induced SOC term [102]

$$\mathcal{H}_{HI} = \sum_{i=0}^{3} \kappa^{1+\delta_{i,2}} \sigma_i (\alpha_1^i s_x + \alpha_2^i s_y), \tag{2.43}$$

where $\alpha_1^i$ and $\alpha_2^i$ are pseudospin-dependent components of SOF. Fig. 2.9c shows the final spin texture, calculated for 3°-twisted graphene/SnTe heterostructure (Fig. 2.9c). As the persistent field is directed in the $k_y$ direction, the spins along $\hat{x}$ have a much shorter spin lifetime. Interestingly, the spin lifetime anisotropy $\zeta = \tau_y/\tau_x \sim \tau_z/\tau_x$ was also predicted to be highly tunable by an external electric field (Fig. 2.9d). Investigation of proximity-induced SOC through spin relaxation anisotropy measurements in a related symmetry-free heterostructure comprising $PdSe_2$ and graphene is the subject of Chapter 6.

## References

[1] W. Gerlach and O. Stern; "Der experimentelle Nachweis der Richtungsquantelung im Magnetfeld". *Zeitschrift für Physik* 1922**, 9**, pp. 349–352. DOI: 10.1007/BF01326983.

[2] W. Heisenberg; "Über quantentheoretische Umdeutung kinematischer und mechanischer Beziehungen." *Zeitschrift für Physik* 1925**, 33**, pp. 879–893. DOI: 10.1007/BF01328377.

[3] M. Born and P. Jordan; "Zur Quantenmechanik". *Zeitschrift für Physik* 1925**, 34**, pp. 858–888. DOI: 10.1007/BF01328531.

[4] W. Pauli; "Über den Einfluß der Geschwindigkeitsabhängigkeit der Elektronenmasse auf den Zeemaneffekt". *Zeitschrift für Physik* 1925**, 31**, pp. 373–385. DOI: 10.1007/BF02980592.

[5] A. H. Compton; "The magnetic electron". *Journal of the Franklin Institute* 1921**, 192**, pp. 145–155. DOI: 10.1016/S0016-0032(21)90917-7.

[6] G. E. Uhlenbeck and S. Goudsmit; "Ersetzung der Hypothese vom unmechanischen Zwang durch eine Forderung bezüglich des inneren Verhaltens jedes einzelnen Elektrons". *Die Naturwissenschaften* 1925**, 13**, pp. 953–954. DOI: 10.1007/BF01558878.

[7] G. E. Uhlenbeck and S. Goudsmit; "Spinning Electrons and the Structure of Spectra". *Nature* 1926**, 117**, pp. 264–265. DOI: 10.1038/117264a0.

[8] L. H. Thomas; "The Motion of the Spinning Electron". *Nature* 1926**, 117**, pp. 514–514. DOI: 10.1038/117514a0.

[9] W. Pauli; "Zur Quantenmechanik des magnetischen Elektrons". *Zeitschrift für Physik* 1927**, 43**, pp. 601–623. DOI: 10.1007/BF01397326.

[10] P. A. M. Dirac; "The quantum theory of the electron". *Proceedings of the Royal Society of London. Series A, Containing Papers of a Mathematical and Physical Character* 1928**, 117**, pp. 610–624. DOI: 10.1098/rspa.1928.0023.

[11] J. Sinova et al.; "Spin Hall effects". *Reviews of Modern Physics* 2015**, 87**, pp. 1213–1260. DOI: 10.1103/RevModPhys.87.1213.

[12] T. McGuire and R. Potter; "Anisotropic magnetoresistance in ferromagnetic 3d alloys". *IEEE Transactions on Magnetics* 1975**, 11**, pp. 1018–1038. DOI: 10.1109/TMAG.1975.1058782.

[13] M. T. Johnson et al.; "Magnetic anisotropy in metallic multilayers". *Reports on Progress in Physics* 1996**, 59**, pp. 1409–1458. DOI: 10.1088/0034-4885/59/11/002.

[14] R. Karplus and J. M. Luttinger; "Hall Effect in Ferromagnetics". *Physical Review* 1954**, 95**, pp. 1154–1160. DOI: 10.1103/PhysRev.95.1154.

[15] N. Nagaosa et al.; "Anomalous Hall effect". *Reviews of Modern Physics* 2010**, 82**, pp. 1539–1592. DOI: 10.1103/RevModPhys.82.1539.

[16] P. Gambardella and I. M. Miron; "Current-induced spin–orbit torques". *Philosophical Transactions of the Royal Society A: Mathematical, Physical and Engineering Sciences* 2011**, 369**, pp. 3175–3197. DOI: 10.1098/rsta.2010.0336.

[17] A. Manchon et al.; "New perspectives for Rashba spin–orbit coupling". *Nature Materials* 2015**, 14**, pp. 871–882. DOI: 10.1038/nmat4360.

[18] Y. A. Bychkov and E. I. Rashba; "Oscillatory effects and the magnetic susceptibility of carriers in inversion layers". *Journal of Physics C: Solid State Physics* 1984**, 17**, pp. 6039–6045. DOI: 10.1088/0022-3719/17/33/015.

[19] G. Dresselhaus; "Spin-Orbit Coupling Effects in Zinc Blende Structures". *Physical Review* 1955**, 100**, pp. 580–586. DOI: 10.1103/PhysRev.100.580.

[20] J. Fabian and S. D. Sarma; "Spin relaxation of conduction electrons". *Journal of Vacuum Science & Technology B: Microelectronics and Nanometer Structures Processing, Measurement, and Phenomena* 1999**, 17**, pp. 1708–1715. DOI: 10.1116/1.590813.

[21] J. Bass and W. P. Pratt; "Spin-diffusion lengths in metals and alloys, and spin-flipping at metal/metal interfaces: an experimentalist's critical review". *Journal of Physics: Condensed Matter* 2007**, 19**, p. 183201. DOI: 10.1088/0953-8984/19/18/183201.

[22] K. Ohnishi et al.; "Spin-transport in superconductors". *Applied Physics Letters* 2020**, 116**, p. 130501. DOI: 10.1063/1.5138905.

[23] E. D. Herbschleb et al.; "Ultra-long coherence times amongst room-temperature solid-state spins". *Nature Communications* 2019**, 10**, p. 3766. DOI: 10.1038/s41467-019-11776-8.

[24] R. J. Elliott; "Theory of the Effect of Spin-Orbit Coupling on Magnetic Resonance in Some Semiconductors". *Physical Review* 1954**, 96**, pp. 266–279. DOI: 10.1103/PhysRev.96.266.

[25] Y. Yafet. "$g$ Factors and Spin-Lattice Relaxation of Conduction Electrons". Vol. 14 (Jan. 1, 1963). Ed. by F. Seitz and D. Turnbull, pp. 1–98. URL: https://www.sciencedirect.com/science/article/pii/S0081194708602593.

[26] H. Ochoa, A. H. Castro Neto, and F. Guinea; "Elliot-Yafet Mechanism in Graphene". *Physical Review Letters* 2012**, 108**, p. 206808. DOI: 10.1103/PhysRevLett.108.206808.

[27] M. Dyakonov and V. Perel; "Spin orientation of electrons associated with the interband absorption of light in semiconductors". *Soviet Physics JETP* 1971**, 33**, pp. 1053–1059.

[28] M. Dyakonov and V. Kachorovskii; "Spin relaxation of two-dimensional electrons in noncentrosymmetric semiconductors". *Semiconductors* 1986**, 20**, p. 110.

[29] E. Santana-Suárez and F. Mireles; "Impact of the p-cubic Dresselhaus term on the spin Hall effect". *Condensed Matter Physics* 2023**, 26**, p. 13504. DOI: 10.5488/CMP.26.13504.

[30] N. F. Mott; "The scattering of fast electrons by atomic nuclei". *Proceedings of the Royal Society of London. Series A, Containing Papers of a Mathematical and Physical Character* 1929**, 124**, pp. 425–442. DOI: 10.1098/rspa.1929.0127.

[31] M. I. Dyakonov and V. I. Perel; "Current-induced spin orientation of electrons in semiconductors". *Physics Letters A* 1971**, 35**, pp. 459–460. DOI: 10.1016/0375-9601(71)90196-4.

[32] M. I. D'yakonov and V. I. Perel'; "Possibility of orienting electron spins with current". *ZhETF Pis. Red.* 1971**, 13**, pp. 657–660.

[33] J. E. Hirsch; "Spin Hall Effect". *Physical Review Letters* 1999**, 83**, pp. 1834–1837. DOI: 10.1103/PhysRevLett.83.1834.

[34] *SOT-MRAM for high-density last-level cache memory | imec*. URL: https://www.imec-int.com/en/articles/novel-sot-mram-architecture-opens-doors-high-density-last-level-cache-memory-applications.

[35] L. Onsager; "Reciprocal Relations in Irreversible Processes. II." *Physical Review* 1931**, 38**, pp. 2265–2279. DOI: 10.1103/PhysRev.38.2265.

[36] L. Onsager; "Reciprocal Relations in Irreversible Processes. I." *Physical Review* 1931**, 37**, pp. 405–426. DOI: 10.1103/PhysRev.37.405.

[37] J. Sinova et al.; "Universal Intrinsic Spin Hall Effect". *Physical Review Letters* 2004**, 92**, p. 126603. DOI: 10.1103/PhysRevLett.92.126603.

[38] M. Gradhand et al.; "Extrinsic Spin Hall Effect from First Principles". *Physical Review Letters* 2010**, 104**, p. 186403. DOI: 10.1103/PhysRevLett.104.186403.

[39] Y. Niimi et al.; "Extrinsic Spin Hall Effect Induced by Iridium Impurities in Copper". *Physical Review Letters* 2011**, 106**, p. 126601. DOI: 10.1103/PhysRevLett.106.126601.

[40] A. Roy, M. H. D. Guimarães, and J. Sławińska; "Unconventional spin Hall effects in nonmagnetic solids". *Physical Review Materials* 2022**, 6**, p. 045004. DOI: 10.1103/PhysRevMaterials.6.045004.

[41] V. Edelstein; "Spin polarization of conduction electrons induced by electric current in two-dimensional asymmetric electron systems". *Solid State Communications* 1990**, 73**, pp. 233–235. DOI: 10.1016/0038-1098(90)90963-C.

[42] T. S. Ghiasi et al.; "Charge-to-Spin Conversion by the Rashba–Edelstein Effect in Two-Dimensional van der Waals Heterostructures up to Room Temperature". *Nano Letters* 2019**, 19**, pp. 5959–5966. DOI: 10.1021/acs.nanolett.9b01611.

[43] C. K. Safeer et al.; "Large Multidirectional Spin-to-Charge Conversion in Low-Symmetry Semimetal $MoTe_2$ at Room Temperature". *Nano Letters* 2019**, 19**, pp. 8758–8766. DOI: 10.1021/acs.nanolett.9b03485.

[44] C. K. Safeer et al.; "Room-Temperature Spin Hall Effect in Graphene/$MoS_2$ van der Waals Heterostructures". *Nano Letters* 2019**, 19**, pp. 1074–1082. DOI: 10.1021/acs.nanolett.8b04368.

[45] L. A. Benítez et al.; "Tunable room-temperature spin galvanic and spin Hall effects in van der Waals heterostructures". *Nature Materials* 2020**, 19**, pp. 170–175. DOI: 10.1038/s41563-019-0575-1.

[46] B. Zhao et al.; "Unconventional Charge–Spin Conversion in Weyl-Semimetal $WTe_2$". *Advanced Materials* 2020**, 32**, p. 2000818. DOI: 10.1002/adma.202000818.

[47] N. Ontoso et al.; "Unconventional Charge-to-Spin Conversion in Graphene/$MoTe_2$ van der Waals Heterostructures". *Physical Review Applied* 2023, **19**, p. 014053. DOI: 10.1103/PhysRevApplied.19.014053.

[48] K. S. Novoselov et al.; "Electric Field Effect in Atomically Thin Carbon Films". *Science* 2004, **306**, pp. 666–669. DOI: 10.1126/science.1102896.

[49] N. D. Mermin; "Crystalline Order in Two Dimensions". *Physical Review* 1968, **176**, pp. 250–254. DOI: 10.1103/PhysRev.176.250.

[50] R. Mas-Ballesté et al.; "2D materials: to graphene and beyond". *Nanoscale* 2011, **3**, pp. 20–30. DOI: 10.1039/C0NR00323A.

[51] Z. Cai et al.; "Chemical Vapor Deposition Growth and Applications of Two-Dimensional Materials and Their Heterostructures". *Chemical Reviews* 2018, **118**, pp. 6091–6133. DOI: 10.1021/acs.chemrev.7b00536.

[52] L. A. Walsh and C. L. Hinkle; "van der Waals epitaxy: 2D materials and topological insulators". *Applied Materials Today* 2017, **9**, pp. 504–515. DOI: 10.1016/j.apmt.2017.09.010.

[53] S. Balendhran et al.; "Elemental Analogues of Graphene: Silicene, Germanene, Stanene, and Phosphorene". *Small* 2015, **11**, pp. 640–652. DOI: 10.1002/smll.201402041.

[54] N. Mounet et al.; "Two-dimensional materials from high-throughput computational exfoliation of experimentally known compounds". *Nature Nanotechnology* 2018, **13**, pp. 246–252. DOI: 10.1038/s41565-017-0035-5.

[55] P. R. Wallace; "The Band Theory of Graphite". *Physical Review* 1947, **71**, pp. 622–634. DOI: 10.1103/PhysRev.71.622.

[56] A. H. Castro Neto et al.; "The electronic properties of graphene". *Reviews of Modern Physics* 2009, **81**, pp. 109–162. DOI: 10.1103/RevModPhys.81.109.

[57] A. S. Mayorov et al.; "Micrometer-Scale Ballistic Transport in Encapsulated Graphene at Room Temperature". *Nano Letters* 2011, **11**, pp. 2396–2399. DOI: 10.1021/nl200758b.

[58] C. R. Dean et al.; "Boron nitride substrates for high-quality graphene electronics". *Nature Nanotechnology* 2010, **5**, pp. 722–726. DOI: 10.1038/nnano.2010.172.

[59] Z. M. Gebeyehu et al.; "Spin communication over 30 µm long channels of chemical vapor deposited graphene on $SiO_2$". *2D Materials* 2019, **6**, p. 034003. DOI: 10.1088/2053-1583/ab1874.

[60] X. Duan et al.; "Two-dimensional transition metal dichalcogenides as atomically thin semiconductors: opportunities and challenges". *Chemical Society Reviews* 2015, **44**, pp. 8859–8876. DOI: 10.1039/C5CS00507H.

[61] A. D. Oyedele et al.; "$PdSe_2$: Pentagonal Two-Dimensional Layers with High Air Stability for Electronics". *Journal of the American Chemical Society* 2017**, 139**, pp. 14090–14097. DOI: 10.1021/jacs.7b04865.

[62] J. Jiang et al.; "Signature of type-II Weyl semimetal phase in $MoTe_2$". *Nature Communications* 2017**, 8**, p. 13973. DOI: 10.1038/ncomms13973.

[63] C.-H. Lee et al.; "Tungsten Ditelluride: a layered semimetal". *Scientific Reports* 2015**, 5**, p. 10013. DOI: 10.1038/srep10013.

[64] X. Xi et al.; "Ising pairing in superconducting $NbSe_2$ atomic layers". *Nature Physics* 2016**, 12**, pp. 139–143. DOI: 10.1038/nphys3538.

[65] B. Sipos et al.; "From Mott state to superconductivity in 1T-$TaS_2$". *Nature Materials* 2008**, 7**, pp. 960–965. DOI: 10.1038/nmat2318.

[66] Q. H. Wang et al.; "Electronics and optoelectronics of two-dimensional transition metal dichalcogenides". *Nature Nanotechnology* 2012**, 7**, pp. 699–712. DOI: 10.1038/nnano.2012.193.

[67] A. Splendiani et al.; "Emerging Photoluminescence in Monolayer $MoS_2$". *Nano Letters* 2010**, 10**, pp. 1271–1275. DOI: 10.1021/nl903868w.

[68] K. F. Mak et al.; "Atomically Thin $MoS_2$: A New Direct-Gap Semiconductor". *Physical Review Letters* 2010**, 105**, p. 136805. DOI: 10.1103/PhysRevLett.105.136805.

[69] R. A. B. Villaos et al.; "Thickness dependent electronic properties of Pt dichalcogenides". *npj 2D Materials and Applications* 2019**, 3**, pp. 1–8. DOI: 10.1038/s41699-018-0085-z.

[70] X. Qian et al.; "Quantum spin Hall effect in two-dimensional transition metal dichalcogenides". *Science* 2014**, 346**, pp. 1344–1347. DOI: 10.1126/science.1256815.

[71] D. Xiao et al.; "Coupled Spin and Valley Physics in Monolayers of $MoS_2$ and Other Group-VI Dichalcogenides". *Physical Review Letters* 2012**, 108**, p. 196802. DOI: 10.1103/PhysRevLett.108.196802.

[72] X. Xu et al.; "Spin and pseudospins in layered transition metal dichalcogenides". *Nature Physics* 2014**, 10**, pp. 343–350. DOI: 10.1038/nphys2942.

[73] J. F. Sierra et al.; "Van der Waals heterostructures for spintronics and opto-spintronics". *Nature Nanotechnology* 2021**, 16**, pp. 856–868. DOI: 10.1038/s41565-021-00936-x.

[74] Y. K. Luo et al.; "Opto-Valleytronic Spin Injection in Monolayer MoS2/Few-Layer Graphene Hybrid Spin Valves". *Nano Letters* 2017**, 17**, pp. 3877–3883. DOI: 10.1021/acs.nanolett.7b01393.

[75] B. Zhao et al.; "Observation of charge to spin conversion in Weyl semimetal $WTe_2$ at room temperature". *Physical Review Research* 2020**, 2**, p. 013286. DOI: 10.1103/PhysRevResearch.2.013286.

[76] P. Song et al.; "Coexistence of large conventional and planar spin Hall effect with long spin diffusion length in a low-symmetry semimetal at room temperature". *Nature Materials* 2020**, 19**, pp. 292–298. DOI: 10.1038/s41563-019-0600-4.

[77] Y. Shen and Q. Wang; "Pentagon-based 2D materials: Classification, properties and applications". *Physics Reports* 2022**, 964**, pp. 1–42. DOI: 10.1016/j.physrep.2022.03.003.

[78] M. Gmitra et al.; "Band-structure topologies of graphene: Spin-orbit coupling effects from first principles". *Physical Review B* 2009**, 80**, p. 235431. DOI: 10.1103/PhysRevB.80.235431.

[79] C. Ertler et al.; "Electron spin relaxation in graphene: The role of the substrate". *Physical Review B* 2009**, 80**, p. 041405. DOI: 10.1103/PhysRevB.80.041405.

[80] M. Wojtaszek et al.; "Absence of hyperfine effects in $^{13}$C-graphene spin-valve devices". *Physical Review B* 2014**, 89**, p. 035417. DOI: 10.1103/PhysRevB.89.035417.

[81] A. Fasolino, J. H. Los, and M. I. Katsnelson; "Intrinsic ripples in graphene". *Nature Materials* 2007**, 6**, pp. 858–861. DOI: 10.1038/nmat2011.

[82] J. C. Meyer et al.; "The structure of suspended graphene sheets". *Nature* 2007**, 446**, pp. 60–63. DOI: 10.1038/nature05545.

[83] M. A. H. Vozmediano, M. I. Katsnelson, and F. Guinea; "Gauge fields in graphene". *Physics Reports* 2010**, 496**, pp. 109–148. DOI: 10.1016/j.physrep.2010.07.003.

[84] D. Huertas-Hernando, F. Guinea, and A. Brataas; "Spin-Orbit-Mediated Spin Relaxation in Graphene". *Physical Review Letters* 2009**, 103**, p. 146801. DOI: 10.1103/PhysRevLett.103.146801.

[85] D. Huertas-Hernando, F. Guinea, and A. Brataas; "Spin relaxation times in disordered graphene". *The European Physical Journal Special Topics* 2007**, 148**, pp. 177–181. DOI: 10.1140/epjst/e2007-00238-0.

[86] M. H. D. Guimarães et al.; "Spin Transport in High-Quality Suspended Graphene Devices". *Nano Letters* 2012**, 12**, pp. 3512–3517. DOI: 10.1021/nl301050a.

[87] I. Neumann et al.; "Electrical Detection of Spin Precession in Freely Suspended Graphene Spin Valves on Cross-Linked Poly(methyl methacrylate)". *Small* 2013**, 9**, pp. 156–160. DOI: 10.1002/smll.201201194.

[88] B. Raes et al.; "Determination of the spin-lifetime anisotropy in graphene using oblique spin precession". *Nature Communications* 2016**, 7**, p. 11444. DOI: 10.1038/ncomms11444.

[89] J. Martin et al.; "Observation of electron–hole puddles in graphene using a scanning single-electron transistor". *Nature Physics* 2008**, 4**, pp. 144–148. DOI: 10.1038/nphys781.

[90] D. Van Tuan et al.; "Spin dynamics and relaxation in graphene dictated by electron-hole puddles". *Scientific Reports* 2016**, 6**, p. 21046. DOI: 10.1038/srep21046.

[91] S. Singh et al.; "Nanosecond spin relaxation times in single layer graphene spin valves with hexagonal boron nitride tunnel barriers". *Applied Physics Letters* 2016**, 109**, p. 122411. DOI: 10.1063/1.4962635.

[92] J. C. Leutenantsmeyer et al.; "Efficient spin injection into graphene through trilayer hBN tunnel barriers". *Journal of Applied Physics* 2018**, 124**, p. 194301. DOI: 10.1063/1.5050874.

[93] M. Gurram, S. Omar, and B. J. v. Wees; "Electrical spin injection, transport, and detection in graphene-hexagonal boron nitride van der Waals heterostructures: progress and perspectives". *2D Materials* 2018**, 5**, p. 032004. DOI: 10.1088/2053-1583/aac34d.

[94] M. Gmitra and J. Fabian; "Graphene on transition-metal dichalcogenides: A platform for proximity spin-orbit physics and optospintronics". *Physical Review B* 2015**, 92**, p. 155403. DOI: 10.1103/PhysRevB.92.155403.

[95] M. Gmitra et al.; "Trivial and inverted Dirac bands and the emergence of quantum spin Hall states in graphene on transition-metal dichalcogenides". *Physical Review B* 2016**, 93**, p. 155104. DOI: 10.1103/PhysRevB.93.155104.

[96] K. Zollner et al.; "Twist- and gate-tunable proximity spin-orbit coupling, spin relaxation anisotropy, and charge-to-spin conversion in heterostructures of graphene and transition metal dichalcogenides". *Physical Review B* 2023**, 108**, p. 235166. DOI: 10.1103/PhysRevB.108.235166.

[97] T. Naimer et al.; "Twist-angle dependent proximity induced spin-orbit coupling in graphene/transition metal dichalcogenide heterostructures". *Physical Review B* 2021**, 104**, p. 195156. DOI: 10.1103/PhysRevB.104.195156.

[98] A. W. Cummings et al.; "Giant Spin Lifetime Anisotropy in Graphene Induced by Proximity Effects". *Physical Review Letters* 2017**, 119**, p. 206601. DOI: 10.1103/PhysRevLett.119.206601.

[99] T. S. Ghiasi et al.; "Large Proximity-Induced Spin Lifetime Anisotropy in Transition-Metal Dichalcogenide/Graphene Heterostructures". *Nano Letters* 2017**, 17**, pp. 7528–7532. DOI: 10.1021/acs.nanolett.7b03460.

[100] L. A. Benítez et al.; "Strongly anisotropic spin relaxation in graphene–transition metal dichalcogenide heterostructures at room temperature". *Nature Physics* 2018**, 14**, pp. 303–308. DOI: 10.1038/s41567-017-0019-2.

[101] J. Ingla-Aynés et al.; "Electrical Control of Valley-Zeeman Spin-Orbit-Coupling–Induced Spin Precession at Room Temperature". *Physical Review Letters* 2021**, 127**, p. 047202. DOI: 10.1103/PhysRevLett.127.047202.

[102] M. Milivojevic et al.; "Giant asymmetric proximity-induced spin–orbit coupling in twisted graphene/SnTe heterostructure". *2D Materials* 2024**, 11**, p. 035036. DOI: 10.1088/2053-1583/ad59b4.

# Chapter 3

# Experimental design

This chapter details the design of spin devices studied in this thesis, focusing on the investigation of proximity-induced effects in graphene-based heterostructures through spin transport and CSI phenomena. The chapter begins by describing the basic geometry of lateral devices, nonlocal measurement schemes and the mechanism of spin injection and detection. It then discusses spin precession experiments under different magnetic field configurations. Finally, it presents the modified geometry of the lateral devices used to investigate proximity-induced anisotropic spin transport and CSI.

## 3.1 Graphene spin valve

The experimental design of the samples used in this thesis to investigate proximity effects is based on the device geometry proposed by Johnson and Silsbee [1, 2]. They were the first to inject a spin-polarised current into one end of a paramagnetic (metallic) material and to measure the spin accumulation on the other end using ferromagnetic (FM) electrodes. This device geometry is called lateral spin valve. In contrast to vertical spin valves, the dominant spin current in lateral devices propagates in the horizontal direction. Lateral spin valves enable measurements in a nonlocal configuration, where the region of the device through which current flows is spatially separated from the voltage leads, i.e., the detection region. Charge contributions, such as the anisotropic magnetoresistance and the Hall effect normally dwarf the spin signal in local measurements. The benefit of the nonlocal configuration is the removal [3] or significant reduction [4] of charge contributions to the signal ($J_c \approx 0$), making the measurement predominantly sensitive to spin. In other words, the nonlocal configuration enables measurements of pure spin currents $J_s$.

The graphene lateral spin valve consists of a narrow graphene channel connected by several FM and NM electrodes (Fig. 3.1a). The geometry of the graphene channel is defined by its width $W$ and length $L$ measured from the FM injector to the FM detector electrode. FM electrodes are designed as thin narrow wires so that their easy axis magnetisation $\vec{M}$ is determined by shape anisotropy, *i.e* along their long axis. Moreover, electrodes are chosen to have different widths $w$, which result in varying coercive fields and thereby allow their relative magnetization to be set to parallel (P)

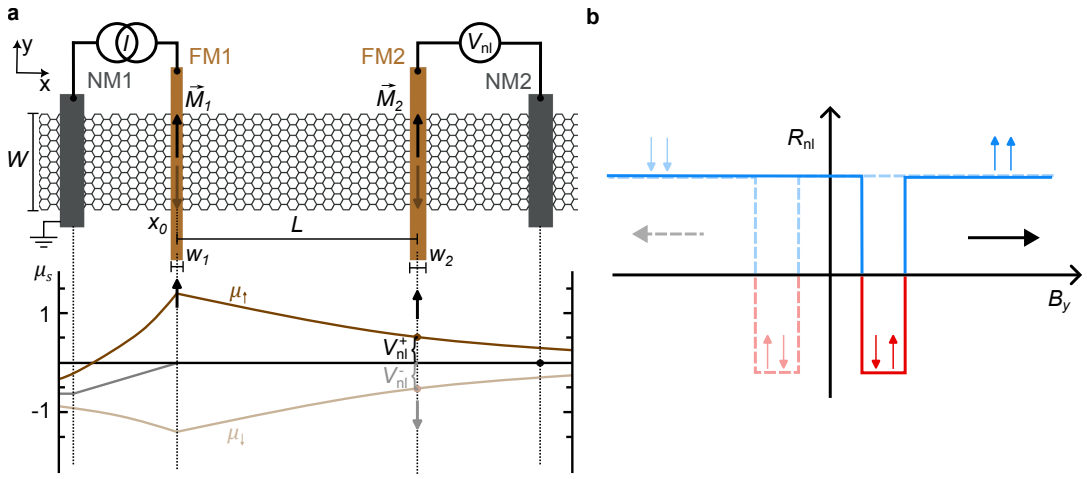


**Fig. 3.1:** Nonlocal measurements of graphene spin valves. **a.** Graphene spin valve with 2 FM electrodes and the spin-dependent electrochemical potential across the sample (below). **b.** The device outputs $\pm V_{nl}$ depending on the relative magnetization of the injector and detector — parallel ($\uparrow\uparrow, \downarrow\downarrow$) or antiparallel ($\uparrow\downarrow, \downarrow\uparrow$) — leading to the signal with two stable states

and antiparallel (AP) configurations, using an external magnetic field applied along their long axis. The NM electrodes are defined at the outer ends of the graphene channel. In the non-local configuration represented in Fig. 3.1a, the electrical current is applied between the FM1-NM1 electrodes, and the voltage is measured between the FM2-NM2 electrodes.

Spin injection into semiconductors and semimetals is more challenging than for metals. The spin injection efficiency of FM electrodes in direct contact with a semiconductor is severely reduced due to the impedance mismatch [5]. The conductivity of graphene is much smaller than that of FM (metallic) electrodes, which leads to spin absorption in the FM and increased spin relaxation rate at the FM/graphene interface. The problem can be addressed by intercalating a tunnel barrier between the FM and graphene [6]. The tunnel barrier also improves the injection of spins, as it provides high spin-dependent resistance and limits the spin-sinking into the FM. The addition of a tunnel barrier enabled the first room-temperature spin transport measurements in mesoscopic lateral devices made of metallic Al [7] and semiconducting GaAs [8] wires.

Electronic spin transport in graphene-based spin valves was demonstrated for the first time by Tombros *et al.* [9] using $Al_2O_3$ tunnel barriers. Since then, different thin insulators have been used to improve spin injection/detection efficiency into graphene, including $TiO_2$ [10], MgO [11] or $TiO_2$ seeded with MgO [12], amorphous carbon [13], fluorinated graphene [14], SrO [15] and 2-3 layers of hBN [16, 17]. The approach in this thesis is based on the intercalation of a $TiO_x$ tunnel barrier and the use of FM Co as a spin-sensitive injector/detector. Details of the fabrication process are presented in Chapter 4.

Having described the basic elements of the graphene spin valve, let us examine spin injection and detection in detail. In FM materials, spin-up and spin-down electrons have different density of states (DOS). Therefore, an electrical current passing

through an FM material is likely to be spin-polarised. When the spin-polarised current $J_c$ flows from the FM to the graphene channel, a nonequilibrium spin accumulation is created underneath the FM contact (Fig. 3.2). The injected spin current $J_s$ is

$$J_s = \frac{\eta\, \mu_B\, J_c}{e}\,, \tag{3.1}$$

where $\eta$ is the polarisation of the FM and $\mu_B$ is the Bohr magneton. The FM's polarisation depends on the relative difference between the (effective) spin-up $N_\uparrow(E_\mathrm{F})$ and spin-down $N_\downarrow(E_\mathrm{F})$ DOS at the Fermi level ($E_\mathrm{F}$)

$$\eta = \frac{N_\uparrow(E_\mathrm{F}) - N_\downarrow(E_\mathrm{F})}{N_\uparrow(E_\mathrm{F}) + N_\downarrow(E_\mathrm{F})}\,. \tag{3.2}$$

The actual spin injection efficiency (injector's polarisation) $P_\mathrm{i}$ is indeed smaller than the theoretically achievable one ($P_\mathrm{i} < \eta\,\mu_B/e$) and depends on the quality of the tunnel barrier, its thickness, bias voltage, and tunnelling matrix for the various bands contributing to the DOS, etc.

The population of spin-polarised carriers then diffuses away from the injection point ($x_0 = 0$) to both sides of the channel. The spin population diffusing to the right side of the sample results in spin accumulation at the detection point ($x \to L$) and induces a nonlocal voltage

$$V_\mathrm{nl} = P_\mathrm{d}\,\frac{\mu_s(L)}{2}\,, \tag{3.3}$$

where $P_\mathrm{d}$ is the spin detection efficiency (detector's polarisation) and $\mu_s(L) = \mu_\uparrow(L) - \mu_\downarrow(L)$ is the spin accumulation beneath the detector colinear with the magnetization of the FM detector. In other words, the detector serves as a spin analyser, as it is sensitive only to the spin component parallel (antiparallel) to the magnetization of the FM, leading to a positive (negative) $V_\mathrm{nl}$. The mechanism of $V_\mathrm{nl}$ detection can be understood by examining Fig. 3.2b and c. The Fermi level of the FM2 contact tends to align with the spin-dependent electrochemical potential in graphene so it is displaced by $\pm P_\mathrm{d}\ \mu_s(L)/2$. In contrast, the NM electrode is insensitive to spin, therefore its potential is aligned with the Fermi level of graphene. Consequently, the $V_\mathrm{nl}$ measured between floating contacts FM2 and NM2 depends only on the spin accumulation below FM2. This is the advantage of having an NM as one of the detector's electrodes.

The measured $V_\mathrm{nl}$ divided by the applied current $I$ at the injector defines the nonlocal resistance $R_\mathrm{nl} = V_\mathrm{nl}/I$. The spin accumulation in the graphene channel as a function of distance from the injector is governed by the Boltzmann equation of diffusion

$$\nabla^2\,\mu_s = \frac{1}{\lambda_s^2}\,\mu_s\,, \tag{3.4}$$

where $\lambda_s$ is the spin diffusion length. If the diffusion is confined to one dimension, which is satisfied provided a high ratio between $L$ and $W$ of the graphene channel,

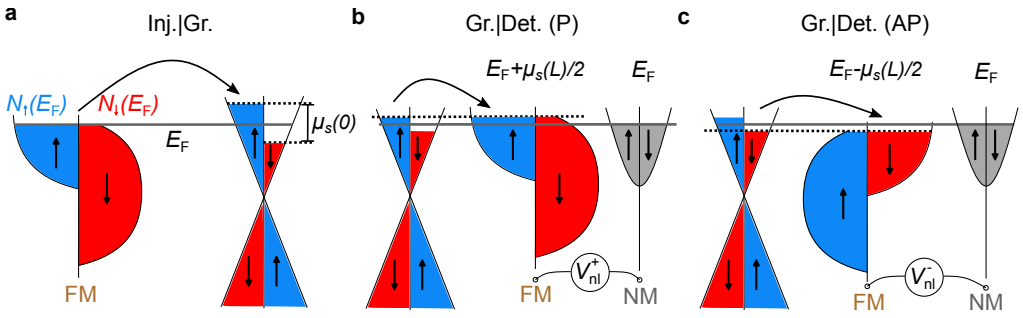


**Fig. 3.2:** Electrical spin injection and detection. **a.** Spin injection from FM electrode. **b**,**c.** Spin detection in P (**b**) and AP (**c**) configuration using one FM and one NM electrode.

the solution of the Boltzmann equation gives

$$\mu_s(x) = \mu_s(0)\,\exp\left[-\frac{x}{\lambda_s}\right], \tag{3.5}$$

where $\mu_s(0)$ is the spin accumulation below the injector. Considering the effect of the injector's and detector's polarisation and their relative magnetisation alignment we obtain

$$R_{\mathrm{nl}} = \pm\frac{1}{2}\,P_{\mathrm{i}}\,P_{\mathrm{d}}\,\frac{\lambda_s}{\sigma\,W}\exp\left[-\frac{x}{\lambda_s}\right], \tag{3.6}$$

where $\sigma$ is the conductivity of graphene. By measuring $R_{\mathrm{nl}}$ as a function of channel length, $\lambda_s$ of the investigated material can be approximately determined. In practice, different $L$ are achieved by attaching different FMs with dissimilar spacing. Therefore, the method is valid if all the used FM electrodes have approximately the same polarisation ($P_j \approx const.$, where $j$ is the index of the FM contact).

The measurement of the $R_{\mathrm{nl}}$ while sweeping the external magnetic field $B_y$ along the long axis of the FM electrodes will display sharp transitions between $+R_{\mathrm{nl}}$ and $-R_{\mathrm{nl}}$ as the relative magnetization between the FM1 and FM2 electrodes changes from parallel ($\uparrow\uparrow$ or $\downarrow\downarrow$) to antiparallel ($\uparrow\downarrow$ or $\downarrow\uparrow$). This type of measurements are commonly referred to as spin valve configuration. Spin valve measurements with two FM electrodes give rise to two switches during the one-directional magnetic field sweep (Fig. 3.1b). The spin valve measurement is used to determine the amplitude of the spin signal and to set the magnetisation of the FM electrodes for precession measurements.

## 3.2 Hanle spin precession in graphene spin valves

The main advantage of lateral spin valves measured in nonlocal configuration is the possibility of performing sensitive spin precession measurements. These allow for the direct determination of spin transport parameters, namely spin relaxation time $\tau_s$ and spin diffusion constant $D_s$, which define the spin diffusion length $\lambda_s = \sqrt{\tau_s\,D_s}$ and the product of injection and detection efficiencies $P_{\mathrm{i}}\,P_{\mathrm{d}}$. Unambiguous determination of the polarisation $P_j$ of a specific FM requires three consecutive

precession measurements with three different FMs (which gives us three equations with three unknown parameters).

In spin precession measurements, an external magnetic field $\vec{B}$ exerts a torque $\vec{\tau}$ on the diffusing spins $\vec{\mu_s} = (\mu_x\ ,\ \mu_y\ ,\ \mu_z)$ making them precess. The torque exerted is

$$\vec{\tau} = \gamma_c\ \vec{\mu_s} \times \vec{B}\ , \tag{3.7}$$

where $\gamma_c$ is a gyromagnetic ratio. For an electron with mass $m_e$ and effective Landé factor $g_e$, the gyromagnetic ratio is

$$\gamma_c = \frac{e\ g_e}{2\,m_e} = \frac{g_e\ \mu_B}{\hbar}\ . \tag{3.8}$$

The Larmor precession frequency is independent of the angle between angular momentum and external magnetic field $\omega_L = |\gamma_c\ B|$, however, no precession occurs for the case $\vec{B} \| \vec{\mu_s}$.

Neglecting the rotation of FM's magnetisation (correct for $B \ll B^{\text{sat}}$, where $B^{\text{sat}}$ is the FM's magnetisation saturation field in the direction of $\vec{B}$) and neglecting the contact-induced relaxation processes (i.e., in the high contact resistance regime), the analytical expression for the precession lineshape when applying the magnetic field perpendicular to the FM is [18]

$$R_{\text{nl}}(B) = \pm\frac{P_{\text{i}}\ P_{\text{d}}}{e^2\ N(E_{\text{F}})\ W}\int_0^{\infty}\frac{1}{\sqrt{4\,\pi\ D_s\ t}}\ \exp\Big[-\frac{L^2}{4\,D_s\ t}\Big]\cos(\omega_L\ t)\ \exp[-\frac{t}{\tau_s}]\ dt\ . \tag{3.9}$$

The first term $\pm\frac{P_{\text{i}}\ P_{\text{d}}}{e^2\ N(E_{\text{F}})\ W}$ captures the magnitude of the spin signal in the absence of an external magnetic field and relaxation processes ($\pm$ corresponds to P and AP configuration, respectively). The second term $\frac{1}{\sqrt{4\,\pi\ D_s\ t}}\exp\Big[-\frac{L^2}{4\,D_s\ t}\Big]$ describes the probability distribution for spins to reach the detector in a time $t$. Note, that we are integrating within the interval $< 0, \infty >$. This means that the time window over which we measure is long enough to capture the contributions of all spins, even those scattered many times on their way to the detector. The third term $\cos(\omega_L\ t)$ accounts for the projection of the spin component colinear with the detector's magnetisation as the spins undergo Larmor precession. The last term $\exp[-\frac{t}{\tau_s}]$ captures the spin relaxation. Fitting the experimental data to the above equation yields the spin transport parameters $D_s, \tau_s, \lambda_s$, and $P_{\text{i}}\ P_{\text{d}}$.

Fig. 3.3 shows a graphical representation of spin precession in a graphene spin valve and a typical Hanle precession curve described by Eq. 3.9. The Hanle curve is symmetric, with a maximum at $B = 0$ and two local minima at $\pm B_{\text{min}}$ corresponding to the field that forces the aggregate spin orientation to precess 180° so the magnetic moment reaches the detector antiparallel to its magnetisation. Diffusive broadening causes the spin signal to die away for fields above $\pm B_{\text{dp}}$, where the spin population completely dephases.

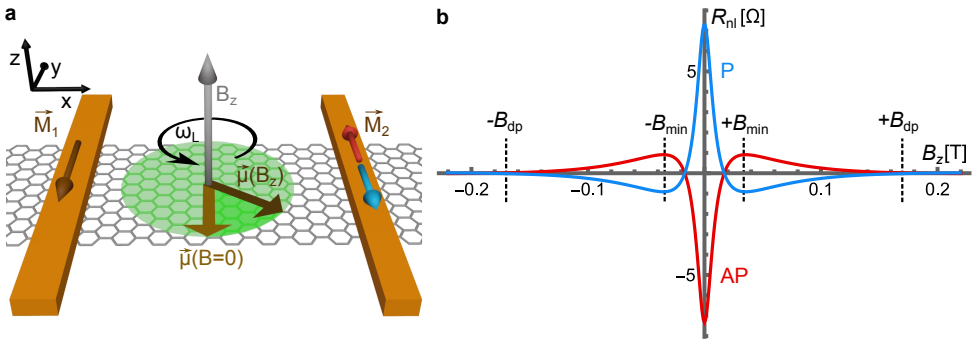


**Fig. 3.3:** Spin precession in a graphene spin valve. **a.** In-plane precession of the magnetic dipole moment $\vec{\mu}$ of an electron caused by the out-of-plane magnetic field $B_z$. **b.** Simulated Hanle precession curves for P and AP configuration using Eq. 3.9.

So far, a generic $\tau_s$ has been introduced. However, spin relaxation might be anisotropic and spin lifetimes can differ for spins pointing in different directions. It is possible to get insights into anisotropic spin dynamics by investigating spin lifetimes along different orientations. One can define the spin lifetime anisotropy as $\zeta_{i,j} = \tau_i^s / \tau_j^s$, where $i \neq j$ and $i, j \in x, y, z$.

Spin lifetime anisotropy provides information about SOFs that dominate spin relaxation in the investigated system. For example, inversion symmetry breaking at the interface induces an electric field across the interface, leading to a $\vec{k}$-dependent in-plane effective magnetic field (i.e. winding spin texture). This Rashba-type SOC relaxes out-of-plane spins twice as fast as in-plane spins $\zeta_{z,\parallel} = \tau_z^s / \tau_\parallel^s < 1$, where $\tau_\parallel^s = \tau_x^s = \tau_y^s$ marks the in-plane spin lifetimes. Conversely, sublattice symmetry breaking leads to the emergence of an in-plane electric field and a valley-contrasting out-of-plane effective magnetic field. This Ising-type SOC relaxes in-plane spins faster than out-of-plane spins $\zeta_{z,\parallel} = \tau_z^s / \tau_\parallel^s > 1$.

Determination of spin lifetime anisotropy is therefore a powerful method for gaining an understanding of SOC in the investigated system. How SOC and the resulting SOFs govern spin relaxation is explained in detail in Section 2.4.

Determination of spin lifetimes along the three spatial directions requires systematic investigation of spin precession under selected magnetic field configurations. Equation 3.9 provides excellent fits to the Hanle precession measurements performed with a magnetic field perpendicular to the sample plane. Here, the spins precess in the graphene plane and $\tau_x^s$ and $\tau_y^s$ can be determined. In our regular graphene devices, with selected dimensions and typical spin diffusion parameters, the spins fully dephase for $B$ of less than a few hundred mT. The out-of-plane magnetisation saturation field of thin FM electrodes made of cobalt is sufficiently large ($B_z^{\text{sat}} \gtrsim 1$ T), therefore the condition $B \ll B^{\text{sat}}$ is easily met and the equation generally gives good fits to the data. The Eq. 3.9 can also be used when the magnetic field is oriented along the spin diffusion direction. In this case, the spins precess in the plane perpendicular to graphene ($yz$ plane) and $\tau_z^s$ and $\tau_y^s$ can be determined. However, the saturation field for the Co electrodes in this direction is much lower, typically $B_x^{\text{sat}} \approx 0.15$ T; therefore,

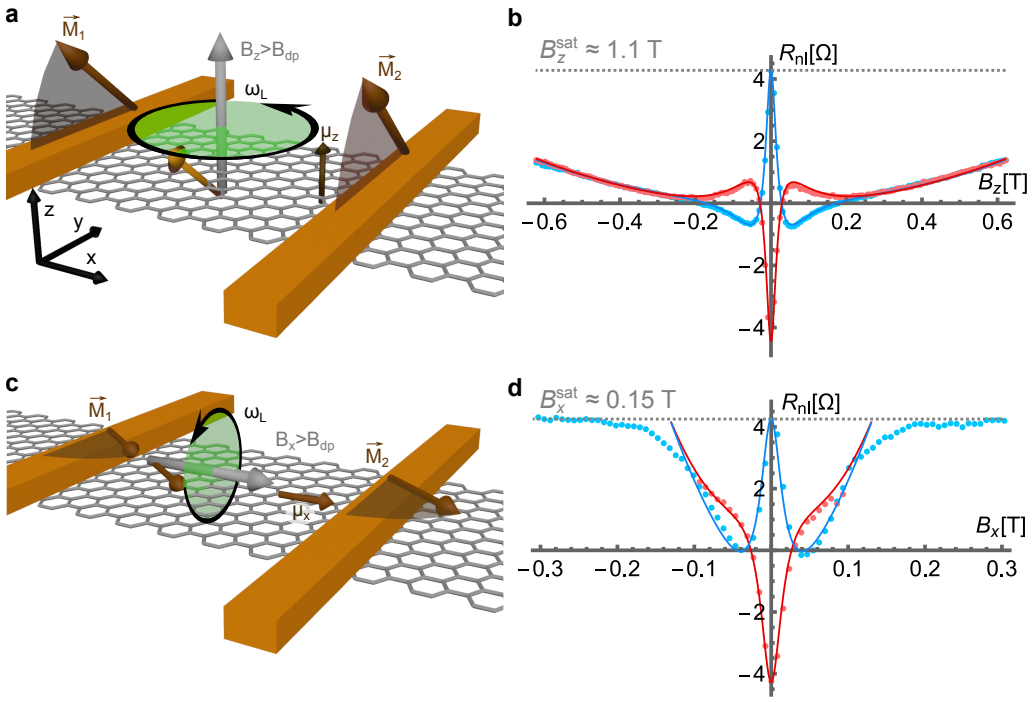


**Fig. 3.4:** Spin precession modelling after including the effect of magnetisation rotation. **a.** Strong $B_z$ tilts the $\vec{M}$ of the FMs out-of-plane, therefore the orientation of injected spins changes. For $B_z > |B_{dp}|$, only the component of magnetic moment parallel to the external field ($\mu_z$ ) contributes to the signal. **b.** Spin precession under an out-of-plane magnetic field considering the tilting of the $\vec{M}$ of the injector and detector contacts. **c.** Already a relatively weak $B_x$ tilts the $\vec{M}$ of the FMs, changing the orientation of the injected spins. For $B_x > |B_{dp}|$, only the spin component $\mu_x$ contributes to the signal. **d.**

the signal deviates from the above equation even for low fields. The problem can be mitigated by increasing the length of the graphene channel to observe the complete precession curve for even lower fields. Different saturation fields are a consequence of the shape anisotropy of the FMs, whose heights, widths, and lengths (measured along $\hat{z}$, $\hat{x}$ and $\hat{y}$, respectively) have an approximate aspect ratio of $1:10:100$.

An improvement in the fits (Fig. 3.4) can be achieved by adding a term that accounts for the rotation of the FM's magnetisation derived using the Stoner-Wohlfarth model

$$R^*_{nl}(B) = R_{nl}(B)\cos^2\Big(\arcsin(B/B^{sat})\Big) + R^0_{nl}\sin^2\Big(\arcsin(B/B^{sat})\Big)\,, \tag{3.10}$$

where $R^0_{nl}$ is the value of the $R_{nl}$ at $B = 0$. Importantly, fitting the experimental data to this modified equation enables the determination of $B^{sat}$. Knowledge of $B^{sat}$ is required to accurately determine $\zeta$ (for details see the next section).

Unfortunately, the magnetisation tilting in the plane tends to deviate from the Stoner-Wohlfarth model. Moreover, the exact behaviour of FM's in-plane magnetisation tilting is often sample-dependent because of, for example, particular domain wall pinning, which limits the use of the method [19]. Therefore, an alternative method to probe $\tau_z^s$ is required.

## 3.3 Oblique spin precession

A better protocol for determining spin relaxation anisotropy was proposed by Raes *et al.* [20] The method relies on the application of oblique magnetic fields in the plane perpendicular to the substrate and parallel to the FMs ($yz$ plane). The oblique angle $\beta$ is defined so that $\beta = 0°$ corresponds to the spin valve configuration (where no precession occurs) and $\beta = 90°$ corresponds to the out-of-plane magnetic field configuration (where spins precess only in-plane). As depicted in Fig. 3.5a, magnetic fields at oblique angles ranging between these two extrema force the spins to precess conically in an oblique plane perpendicular to $\vec{B} = (0\ ,\ B\cos(\beta)\ ,\ B\sin(\beta))$.

The evolution of the spin density is derived by solving the steady-state Bloch diffusion equation in 1D:

$$D_s \frac{\partial^2}{\partial x^2}\vec{\mu}_s - \gamma_c\, \vec{\mu}_s \times \vec{B} - \overline{\tau_s^{-1}} \cdot \vec{\mu}_s = 0\ , \tag{3.11}$$

where tensor $\overline{\tau_s^{-1}}$ is a diagonal matrix containing the spin relaxation times in the three spatial directions

$$\overline{\tau_s^{-1}} = \begin{pmatrix} (\tau_x^s)^{-1} & 0 & 0 \\ 0 & (\tau_y^s)^{-1} & 0 \\ 0 & 0 & (\tau_z^s)^{-1} \end{pmatrix}\ . \tag{3.12}$$

In the case of a *homogeneous spin channel*, boundary conditions to the Bloch diffusion equation are

$$\begin{Bmatrix} x = 0: & \vec{\mu}_{s_I} = \vec{\mu}_{s_{II}} & \vec{J}_{s_I} = \vec{J}_{s_{II}} + \vec{J}_{s_0} \\ x \to \pm\infty: & \vec{\mu}_s = 0 & \vec{J}_s = 0 \end{Bmatrix}, \tag{3.13}$$

where Roman numbers mark the specific region of the sample and $\vec{J}_{s_0} = (0, J_{y_0}, 0)$ is the injected spin current along $\hat{y}$. The last boundary condition ensures complete spin relaxation at a large distance from the injector. A homogeneous spin channel implies that the same spin transport parameters govern the spin diffusion throughout the whole sample through which the spins diffuse.

In their original paper, Raes *et al.* focused solely on the non-precessing spin component, which largely simplifies the data analysis [20]. The spin components misaligned with the external magnetic field completely dephase for $B \geq |\pm B_{\mathrm{dp}}|$. For larger $B$, only the non-precessing component $R_{\mathrm{dp}}^{\beta} = R_{\mathrm{nl}}^{\beta}(\pm B_{\mathrm{dp}})$ parallel to $\vec{B}$ contributes to the measured spin signal

$$R_{\mathrm{dp}}^{\beta} = \overline{R}_{\mathrm{nl}}(\zeta, \beta)\cos^2(\beta^*)\ , \tag{3.14}$$

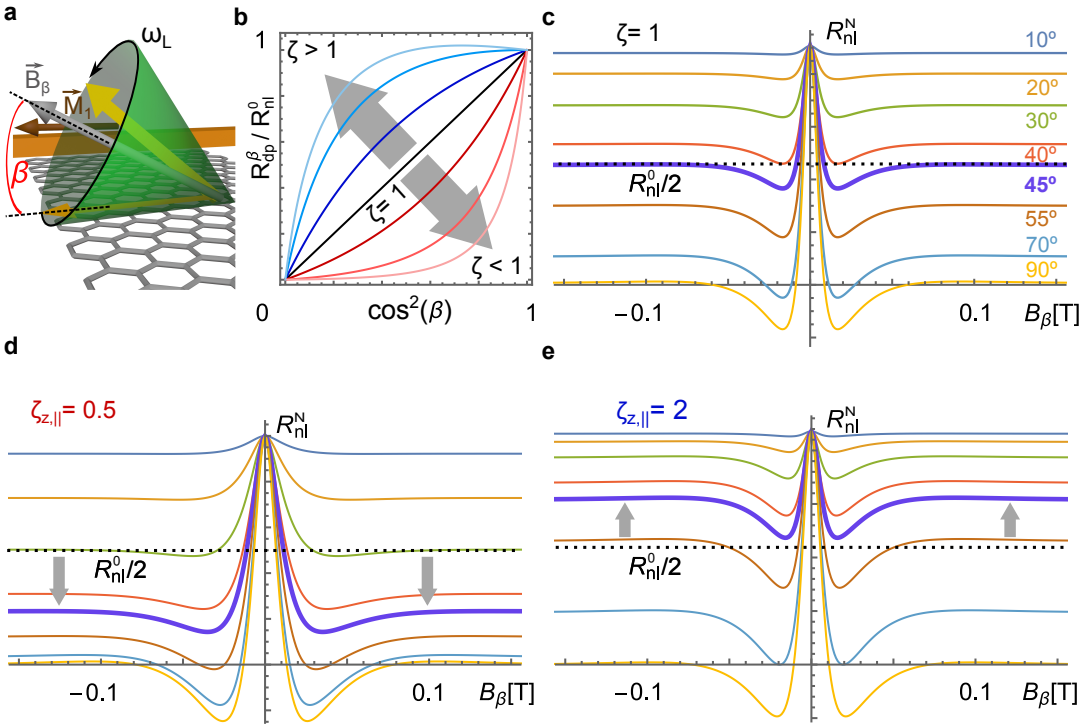


**Fig. 3.5:** Oblique spin precession. **a.** A magnetic field $\vec{B}_\beta$ at an oblique angle $\beta$ induces conical spin precession. **b.** Trends in $R^\beta_{\rm dp}/R^0_{\rm nl}$ vs $\cos^2(\beta)$ for various $\zeta$. **c**,**d**,**e.** Oblique spin precession curves at various angles $\beta$ change shape depending on the value of $\zeta$. Spin relaxation is isotropic in (**c**) and anisotropic with spins out-of-plane (**d**) and in-plane (**e**) relaxing faster.

where $\beta^* = \beta - \gamma(\beta, B)$ is the angle between the axis of injection/detection at $B$ and $\vec{B}$. The axis of injection and detection is defined by the tilted $\vec{M}$ of the FM electrodes

$$\gamma(\beta, B) = \arcsin\left(\frac{B\,\sin(\beta)}{B^{\rm sat} + B\,\cos(\beta)}\right), \tag{3.15}$$

similar to the term $\arcsin(B/B^{\rm sat})$ in the Eq. 3.10, where $\beta = 90°$ but generalized for an arbitrary oblique angle $\beta$. The term $\overline{R}_{\rm nl}(\zeta, \beta)$ is

$$\overline{R}_{\rm nl}(\zeta, \beta) = \sqrt{\frac{\tau_{s,\beta}}{\tau_{s,\|}}}\exp\left[-\frac{L}{\lambda_s^\|}\left(\sqrt{\frac{\tau_{s,\|}}{\tau_{s,\beta}}} - 1\right)\right] R^0_{\rm nl}\,, \tag{3.16}$$

where $\lambda_s^\|$ is the spin diffusion length for spins in the graphene plane.

Realising that

$$\frac{\tau_{s,\beta}}{\tau_{s,\|}} = \left(\cos^2(\beta) + \zeta^{-1}\sin^2(\beta)\right)^{-1}, \tag{3.17}$$

we can extract the parameter $\zeta$ by plotting $R^\beta_{\rm dp}/R^0_{\rm nl}$ vs $\cos^2(\beta)$. Figure 3.5b shows how the $R^\beta_{\rm dp}/R^0_{\rm nl}$ vs $\cos^2(\beta)$ curves deviate from the identity function ($\zeta = 1$) when the out-of-plane spin lifetime is larger ($\zeta > 1$) and smaller ($\zeta < 1$) than the in-plane spin lifetime.

To accurately determine $\zeta$ using the equations above, the value of $B_{\rm dp}$ must be sufficiently low ($B_{\rm dp} \lesssim 0.15$) because, for larger $B$, magnetoresistive effects start to

affect the measured signal. Therefore the applicability of the method is conditioned by a sufficiently large $L$. The required value of $L$ depends on $\lambda_s$ and hence varies from sample to sample. A good guiding principle is to design devices with $L \geq \sqrt{2}\lambda_s$.

Alternatively, instead of focusing solely on the component parallel to $\vec{B}$ (i.e. $R^{\beta}_{\mathrm{dp}}$), we can use the solution of the Bloch diffusion equation to obtain fits of the precession curves in the full range of $\vec{B}$. Figures 3.5c,d,e show the lineshape of normalised spin precession curves $R^{\mathrm{N}}_{\mathrm{nl}} = R^{\beta}_{\mathrm{nl}}/R^{0}_{\mathrm{nl}}$ for a few selected $\beta$ and $\zeta$. Figure 3.5c shows oblique precession curves for the case of isotropic graphene ($\zeta = 1$), thus, $R_{\mathrm{nl}}$ saturates at the value $R^{45^\circ}_{\mathrm{dp}} = R^{0}_{\mathrm{nl}}\cos^2(45^\circ) = R^{0}_{\mathrm{nl}}/2$. In Figure 3.5d out-of-plane spins relax faster ($\zeta = 0.5$), thus, $R^{45^\circ}_{\mathrm{dp}} < R^{0}_{\mathrm{nl}}/2$. In contrast, in Figure 3.5e out-of-plane spins relax slower ($\zeta = 2$), thus, $R^{45^\circ}_{\mathrm{dp}} > R^{0}_{\mathrm{nl}}/2$. Measuring the spin precession with $\beta = 45^\circ$ gives a quick insight into the hierarchy of spin lifetimes.

The spin population precessing under oblique $\vec{B}$ acquires all three spatial components $\mu_x$, $\mu_y$, $\mu_z$. Therefore, the line shape of the precession curve is sensitive to all three spin lifetimes and the method is advantageous for systems where the spin lifetimes are different also in plane ($\tau^s_x \neq \tau^s_y$).

## 3.4 Proximitized graphene spin valves

The experimental devices tested in this thesis to investigate proximity effects consist of a graphene spin channel partially covered by another vdW material. A schematic of the device with an *inhomogeneous spin channel*, having proximitized and pristine graphene zones, is shown in Fig. 3.6a, and consists of 5 different regions. Boundary conditions for the Bloch diffusion equation describing spin transport in the inhomogeneous spin channel are

$$\left\{\begin{array}{lccc} x = 0: & \vec{\mu}_{s_I} = \vec{\mu}_{s_{II}} & \vec{J}_{s_I} = \vec{J}_{s_{II}} + \vec{J}_{s_0} \\ x = l: & \vec{\mu}_{s_{II}} = \vec{\mu}_{s_{III}} & \vec{J}_{s_{II}} = \vec{J}_{s_{III}} \\ x = l + w_H: & \vec{\mu}_{s_{III}} = \vec{\mu}_{s_{IV}} & \vec{J}_{s_{III}} = \vec{J}_{s_{IV}} \\ x = L: & \vec{\mu}_{s_{IV}} = \vec{\mu}_{s_V} & \vec{J}_{s_{IV}} = \vec{J}_{s_V} \\ x \to \pm\infty: & \vec{\mu}_s = 0 & \vec{J}_s = 0 \end{array}\right\}, \tag{3.18}$$

where $l$ is the distance from the injector (FM2) to the beginning of the proximitized region, and $w_H$ is the width of the proximitized region.

This device geometry is chosen to investigate proximity-induced effects for the following reasons:

1. Spin transport parameters (such as $\tau_s$ and $D_s$ of graphene and $P_j$ of FMs) vary from sample to sample. Therefore, it is essential first to characterise the bare graphene channel and only then examine the heterostructure and compare the spin transport properties. The possibility of characterising the spin transport parameters of bare graphene regions is ensured by adding at least one more FM electrode on both sides of the graphene channel (to region I and region V).

2. The spin diffusion length in the investigated graphene heterostructures is usually significantly reduced by proximity-induced effects (e.g. SOC, exchange interaction). Therefore, FM electrodes must be placed closer together to measure appreciable spin signals. Doing so, however, would increase the contribution of spurious effects to the signal (e.g. charge contributions and contact-induced relaxation). By proximitizing only a narrow region of the graphene channel, we ensure that a sufficiently large spin population remains polarised after passing through the heterostructure.

3. Finally, new characteristic features of the precession curve emerge for the anisotropic system when the injector and detector are placed at different distances from the proximitized region (different lengths of region II and region IV in Fig. 3.6). These features help to identify the spin relaxation anisotropy and dominant SOFs in proximitized graphene (see Chapter 5).

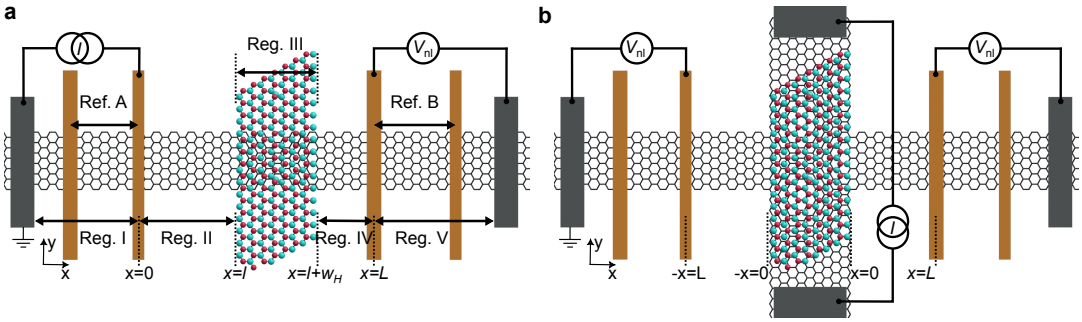


**Fig. 3.6:** Geometries of graphene/2DM heterostructures to investigate anisotropic spin transport (**a**) and charge-spin interconversion (**b**).

## 3.5 Device geometry for spin-charge interconversion experiments

Bare graphene has negligible SOC, thus it is impossible to interconvert charge and spin in the material alone. However, graphene proximitized by a strong SOC material (such as a TMDC) acquires a sufficiently large SOC, which enables the conversion of charge to spin currents and vice versa. Generating or detecting spin currents and spin densities in graphene becomes possible via the (inverse) spin Hall effect and the (inverse) spin galvanic (Rashba-Edelstein) effect. Apart from implications for practical applications, investigating charge-spin interconversion (CSI) mechanisms in graphene-based heterostructures can serve as a complementary method for determining emerging spin textures in proximitized graphene.

The design of the devices used to investigate CSI depends on whether the material proximitizing graphene conducts electrical current. If the 2DM is conducting, two NM electrodes directly contact the metallic material. In this case, a spin-polarised population is generated by applying a charge current through the 2DM alone. If the

2DM proximitizing graphene is insulating or semiconducting, Hall bars of graphene that protrude from below the material are required (Fig. 3.6b). The geometry was first described in [21]. Two NM electrodes are used to contact the sides of the graphene Hall bar and a spin-polarised population is generated by applying current between them (charge-to-spin conversion). The CSI-generated spins diffuse from the proximitized region and induce $V_{nl}$ between the FM and NM detector contact, as for the conventional lateral spin devices (see Section 3.1). Alternatively, current source and voltage probes can be swapped, spins injected by the FM diffuse towards the proximitized region, and induce a $V_{nl}$ across the Hall bar (spin-to-charge conversion). The relationship between these two reciprocal effects is governed by Onsager relations [22, 23].

Although the first type of device, with conducting 2DM, is easier to fabricate, data analysis is more complicated, because the spin population in the heterostructure may be generated by both the proximitized graphene and the 2DM. In contrast, charge current cannot flow through an insulating 2DM, and the only possible source of spin population is the charge converted by passing through proximitized graphene. In the case of semiconducting material, it is important to perform the experiments within its band gap to prevent current shunting, which would also result in contributions from the bulk.

## References

[1] M. Johnson and R. H. Silsbee; "Interfacial charge-spin coupling: Injection and detection of spin magnetization in metals". *Physical Review Letters* 1985**, 55**, pp. 1790–1793. DOI: 10.1103/PhysRevLett.55.1790.

[2] M. Johnson and R. H. Silsbee; "Spin-injection experiment". *Physical Review B* 1988**, 37**, pp. 5326–5335. DOI: 10.1103/PhysRevB.37.5326.

[3] S. O. Valenzuela and M. Tinkham; "Direct electronic measurement of the spin Hall effect". *Nature* 2006**, 442**, pp. 176–179. DOI: 10.1038/nature04937.

[4] F. Volmer et al.; "Charge-Induced Artifacts in Nonlocal Spin-Transport Measurements: How to Prevent Spurious Voltage Signals". *Physical Review Applied* 2022**, 18**, p. 014028. DOI: 10.1103/PhysRevApplied.18.014028.

[5] G. Schmidt et al.; "Fundamental obstacle for electrical spin injection from a ferromagnetic metal into a diffusive semiconductor". *Physical Review B* 2000**, 62**, R4790–R4793. DOI: 10.1103/PhysRevB.62.R4790.

[6] E. I. Rashba; "Theory of electrical spin injection: Tunnel contacts as a solution of the conductivity mismatch problem". *Physical Review B* 2000**, 62**, R16267–R16270. DOI: 10.1103/PhysRevB.62.R16267.

[7] F. J. Jedema et al.; "Electrical detection of spin precession in a metallic mesoscopic spin valve". *Nature* 2002**, 416**, pp. 713–716. DOI: 10.1038/416713a.

[8] X. Lou et al.; "Electrical detection of spin transport in lateral ferromagnet–semiconductor devices". *Nature Physics* 2007**, 3**, pp. 197–202. DOI: 10.1038/nphys543.

[9] N. Tombros et al.; "Electronic spin transport and spin precession in single graphene layers at room temperature". *Nature* 2007**, 448**, pp. 571–574. DOI: 10.1038/nature06037.

[10] J. F. Sierra et al.; "Thermoelectric spin voltage in graphene". *Nature Nanotechnology* 2018**, 13**, pp. 107–111. DOI: 10.1038/s41565-017-0015-9.

[11] W. Han et al.; "Electrical detection of spin precession in single layer graphene spin valves with transparent contacts". *Applied Physics Letters* 2009**, 94**, p. 222109. DOI: 10.1063/1.3147203.

[12] W. Han et al.; "Tunneling Spin Injection into Single Layer Graphene". *Physical Review Letters* 2010**, 105**, p. 167202. DOI: 10.1103/PhysRevLett.105.167202.

[13] I. Neumann et al.; "Enhanced spin accumulation at room temperature in graphene spin valves with amorphous carbon interfacial layers". *Applied Physics Letters* 2013**, 103**, p. 112401. DOI: 10.1063/1.4820586.

[14] A. L. Friedman et al.; "Homoepitaxial tunnel barriers with functionalized graphene-on-graphene for charge and spin transport". *Nature Communications* 2014**, 5**, p. 3161. DOI: 10.1038/ncomms4161.

[15] S. Singh et al.; "Strontium Oxide Tunnel Barriers for High Quality Spin Transport and Large Spin Accumulation in Graphene". *Nano Letters* 2017**, 17**, pp. 7578–7585. DOI: 10.1021/acs.nanolett.7b03543.

[16] M. V. Kamalakar et al.; "Enhanced Tunnel Spin Injection into Graphene using Chemical Vapor Deposited Hexagonal Boron Nitride". *Scientific Reports* 2014**, 4**, p. 6146. DOI: 10.1038/srep06146.

[17] M. Gurram, S. Omar, and B. J. v. Wees; "Bias induced up to 100% spin-injection and detection polarizations in ferromagnet/bilayer-hBN/graphene/hBN heterostructures". *Nature Communications* 2017**, 8**, p. 248. DOI: 10.1038/s41467-017-00317-w.

[18] W. S. Torres et al.; "Spin precession and spin Hall effect in monolayer graphene/Pt nanostructures". *2D Materials* 2017**, 4**, p. 041008. DOI: 10.1088/2053-1583/aa8823.

[19] B. Raes et al.; "Spin precession in anisotropic media". *Physical Review B* 2017**, 95**, p. 085403. DOI: 10.1103/PhysRevB.95.085403.

[20] B. Raes et al.; "Determination of the spin-lifetime anisotropy in graphene using oblique spin precession". *Nature Communications* 2016**, 7**, p. 11444. DOI: 10.1038/ncomms11444.

[21] D. Van Tuan et al.; "Spin Hall Effect and Origins of Nonlocal Resistance in Adatom-Decorated Graphene". *Physical Review Letters* 2016**, 117**, p. 176602. DOI: 10.1103/PhysRevLett.117.176602.

[22] L. Onsager; "Reciprocal Relations in Irreversible Processes. I." *Physical Review* 1931**, 37**, pp. 405–426. DOI: 10.1103/PhysRev.37.405.

[23] L. Onsager; "Reciprocal Relations in Irreversible Processes. II." *Physical Review* 1931**, 38**, pp. 2265–2279. DOI: 10.1103/PhysRev.38.2265.

# Chapter 4

# Sample fabrication and characterisation

This chapter describes the device fabrication and characterisation methods used in this thesis. Sample fabrication starts with the exfoliation of 2DMs, followed by the identification of thin flakes with an optical microscope and their characterisation with Raman spectroscopy and atomic force microscopy. Selected 2DMs are stacked in vertical van der Waals heterostructures using deterministic transfer techniques. Annealing of the stacks in ultra-high vacuum is done to improve the quality of the interface between the 2DMs. The electrodes are subsequently defined using electron-beam lithography and metallisation. The final devices are then wired to a chip carrier and loaded in a cryostat, where the transport measurements are performed. Finally, when finalising the electrical characterisation, the devices are imaged by scanning electron microscopy. The following pages describe each step and the characterisation method in detail.

## 4.1 Mechanical exfoliation

The first successfully isolated and characterised 2DM, graphene, was obtained by mechanical exfoliation by Geim and Novoselov in 2004 [1]. Since then, researchers have been commonly using mechanical exfoliation to yield high-quality 2D single crystals on a laboratory scale. The ease and inexpensiveness of the process surely contributed to the rapid expansion of the 2DM family over the last 20 years.

Mechanical exfoliation relies on overcoming weak interlayer vdW forces. Thinner flakes of vdW materials can be detached from the bulk by peeling off the vdW layers using adhesive tape. Several exfoliation steps are usually needed to obtain thin layers. However, excessive exfoliation diminishes the size of the flakes, as the crystals tend to fragment during the process. Once the tape contains thin layers, the last exfoliation is performed to transfer the 2DM, though this time between the tape and the highly doped silicon substrate with a thin $SiO_2$ overlayer (i.e. $SiO_2/Si^{++}$ substrate).

Each material exfoliates in its unique way; therefore, different strategies are needed, depending on the material in question. The success of the process depends, for example, on the right choice of adhesive, which may include Scotch, Kapton,

Nitto tapes, or polydimethylsiloxane (PDMS) film. Other important parameters include the geometry and kinetics of exfoliation [2], such as the pressure applied to the tape, the speed and angle of peeling, the roughness of the substrate, and its temperature. Proper pre-treatment of the substrates is also crucial for successful exfoliation. Oxygen plasma treatment of the substrates before exfoliation helps to remove adsorbed hydrocarbons, water and other undesired species from the surface [3]. Their presence would otherwise prevent 2DM from adhering to the substrate and cause a low yield of thin layers.

Graphene, hBN, and most TMDCs are stable in ambient environment, therefore, they can be exfoliated in air, although it is better to do so in a cleanroom atmosphere to limit dust contamination and have control over humidity. However, many other 2DMs degrade under ambient conditions through oxidation and hydrolysis, so their exfoliation in $O_2$ and $H_2O$-free environment is necessary. The interior of an argon-filled glovebox provides such an inert environment while allowing the manipulation of the samples.

## 4.2 Optical microscopy

The substrates with exfoliated 2DMs are examined under an optical microscope. Optical contrast between flakes of varying thicknesses on $SiO_2$ substrate emerges due to the light interference [4]. A fraction of light is reflected from the surface of the 2DM, another faction is reflected from the 2DM/$SiO_2$ interface, and finally, the last fraction is reflected from the interface between $SiO_2$ and Si. Therefore, optical contrast depends on the wavelength and angle of the incident light, the thickness and refractive index of 2DM, and the exact $SiO_2$ thickness [5]. Optimal contrast for different 2DMs is achieved by carefully choosing a substrate with ideal $SiO_2$ thicknesses [6]. Typically, 90-nm thick $SiO_2$ is used to identify thin hBN and 300-nm or 440-nm thick $SiO_2$ is used to identify graphene and few-layer TMDCs. In addition to standard bright-field microscopy, dark-field microscopy excludes unscattered light from the image increasing the visibility of cracks in 2DMs and localized contaminants on their surface.

## 4.3 Raman spectroscopy

The capacity to correctly determine the thickness of thin 2DMs is based on the previous calibration of optical contrast with Raman spectroscopy. This is achieved by acquiring Raman spectra of flakes, whose images were captured beforehand with the optical microscope.

Raman spectroscopy is a simple and nondestructive characterisation tool to determine the type of material, the presence of strain, disorder, and damage. It relies on inelastic scattering of incident laser light from the investigated sample. Photons interacting with the phonons or molecular vibrations gain or lose small quanta of

energy leading to frequency shift (anti-Stokes vs Stokes). Raman spectra display several peaks corresponding to different vibrational modes of the material. The thickness determination of thin flakes relies on changes in Raman shifts of peaks and their shape and intensity with the number of 2D layers. For instance, graphite and thin graphene flakes display two characteristic peaks in the Raman spectra [7], one at around 1582 $cm^{-1}$ (G) and one at around 2680 $cm^{-1}$ (2D). The shape of the 2D peak and the ratio between the two peaks change with the varying number of 2D layers as shown in Fig. 4.1a.

In addition, polarised Raman spectroscopy can determine the crystallographic directions of anisotropic materials such as $PdSe_2$ [8] and $WTe_2$ [9]. The intensity of characteristic vibrational modes varies with the changing angle between the light's polarisation and crystallographic directions (see Chapters 7 and 6).

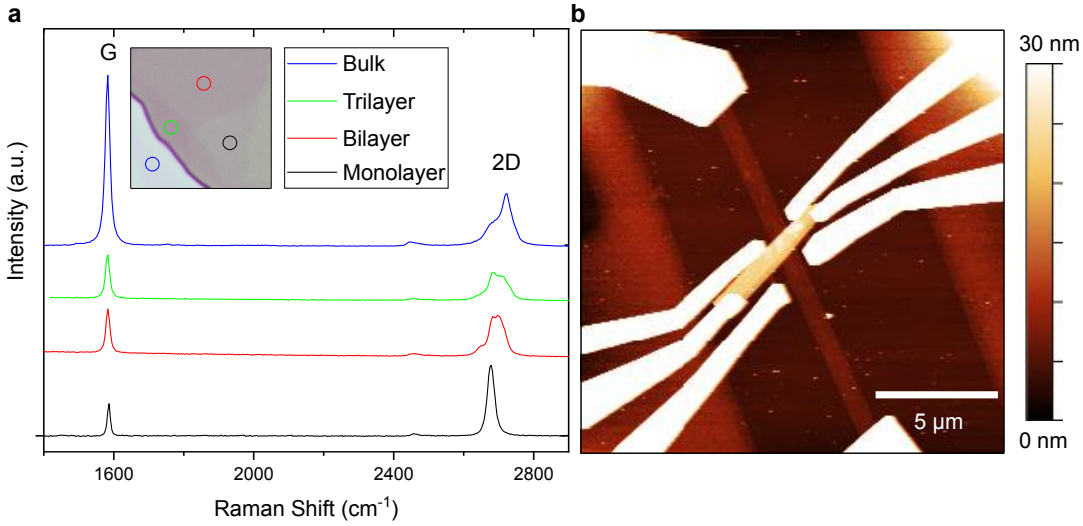


**Fig. 4.1:** Raman spectroscopy and AFM. **a.** Raman spectra of mono-, bi- and trilayer graphene and bulk graphite. The inset shows the focus points of incident laser light on graphene of varying thickness on a 440-nm $SiO_2/Si^{++}$ substrate. **b.** AFM measurement of graphene-based heterostructure. The graphene was etched into a Hall bar and contacted by NM electrodes.

## 4.4 Atomic force microscopy

Atomic force microscopy (AFM) is a technique that captures detailed topographic images of the investigated samples by scanning the surface line-by-line with an atomically sharp tip on a cantilever. Fig. 4.1b shows an AFM image of a sample under fabrication. During AFM measurement, the attractive/repulsive forces of various kinds (e.g. mechanical, electrostatic, van der Waals, and other forces) between the sample and the piezoelectrically controlled tip deflect the cantilever. The tapping mode is the most commonly used AFM measurement mode during which the cantilever is set to oscillate at a constant frequency near its resonance. The interaction of the tip with the specimen changes the set amplitude of the cantilever's oscillation. An electronic servo then adjusts the tip's distance from the surface to recover the set amplitude. A laser beam is directed at and reflected by the cantilever, and the

photodiode detects the deflection. Because the magnitude of the deflection depends on the distance between the tip and the surface of the sample, the height profile can be measured.

AFM is useful for determining the approximate thickness of 2DMs and displaying and sweeping away [10] the surface contaminants or even pushing out residues that are trapped at the interface of vdW heterostructures [11].

## 4.5 Deterministic transfer of 2DMs

Once the individual 2D flakes are identified and characterised, they are assembled in vertical van der Waals heterostructures. This is achieved by employing the viscoelastic stamping method [12]. The technique relies on transparent stamps made of elastic polymeric films, such as bare PDMS, polycarbonate (PC)-PDMS bilayer, polypropylcarbonate (PPC)-PDMS bilayer and many more [13]. The stamp is placed on a microscope slide and fixed on a transfer arm controlled by a micromanipulator. The flake of interest is then localised on the substrate and the stamp is brought in contact with the sample using the transfer arm. The transparent nature of the stamp allows for visual control of the process using an optical microscope. The substrate is heated to 40°C when using a PPC-based stamp and to about 150°C when using a PC-based stamp. The polymer becomes more viscose at elevated temperatures, promoting adhesion between the stamp and the selected flake. The stamp with the 2DM is then detached from the substrate by lifting the transfer arm. A second 2DM, exfoliated on a separate substrate, is then aligned with the flake on the stamp using the microscope, and the two materials are brought in contact by moving the transfer arm down. Stacking the 2DMs at an elevated temperature (approximately above 110°) promotes the cleanliness of the interface, as the residues become more mobile and can be pushed out during the stamping [14]. Then, the temperature is increased above the polymer's melting point and the arm is lifted again. The PPC (or PC) layer detaches from the PDMS layer and remains on the substrate with the desired heterostructure. Finally, the polymer is quickly dissolved by immersing the sample in chloroform and then the sample is washed in acetone and isopropyl alcohol (IPA).

## 4.6 Thermal annealing

High vacuum annealing removes residues from the surface of assembled vdW heterostructures, remaining from the exfoliation process and transfer steps and, even more importantly, improves the interface quality between the individual 2DMs by reducing air bubbles and blisters. High temperature increases the mobility of residues trapped in the vdW sandwich leading to the formation of pockets containing the accumulated residues. Some pockets are pushed out of the heterostructure and others remain trapped at the interface. The formation of contamination-free regions leads to a significant enhancement of proximity effects. The annealing step is always

conducted at a pressure of $10^{-8}$ mbar. The exact temperature and duration of the annealing typically range from 250°C to 400°C and 1 to 4 hours, depending on the 2DM being processed and their thermal stability.

## 4.7 E-beam lithography, plasma etching, e-beam evaporation and sample installation

After the assembly of the heterostructures, electrodes that contact the 2DMs are fabricated in several electron-beam (e-beam) lithography and e-beam evaporation steps, as illustrated in Fig. 4.2. A double layer of standard positive lithography resists, methyl methacrylate (MMA) EL6 and polymethyl methacrylate (PMMA) A4 is spin-coated onto the samples. The design of the electrodes is prepared with the software *KLayout* and the writing is done with a high-resolution e-beam lithography system *Raith 150 Two*. After the e-beam writing, the exposed polymer is removed by soaking the samples in a solution of methyl isobutyl ketone (MIBK) and IPA — MIBK: IPA (1:3) developer — for 90 s and the reaction is quenched with IPA. The metallization of the contact is done by e-beam evaporation. In this thesis, an *AJA Intercontinental* evaporator system with a base pressure of $10^{-8}$ mbar was used. Usually, two (or three) lithography-evaporation steps are required to define all necessary electrodes. First, NM electrodes made of Ti/Pd (1 nm/40 nm) are defined to contact the graphene and the TMDC. Environmentally unstable TMDCs form a superficial oxide layer when exposed to air, therefore, an additional lithography-evaporation cycle is required to contact it separately from graphene. In this step, argon plasma etching is performed *in-situ* to remove the oxidised surface of the material and only then the metal is evaporated. After all the NM electrodes have been evaporated, FM electrodes are defined on the graphene channel. The tunnel barrier, consisting of $TiO_2$, is prepared by a two-step evaporation-oxidation process. First, 5 Å thick layer of Ti is evaporated, followed by 40 min of oxidation in $O_2$ gas at a partial pressure of $10^{-2}$ mbar. The same evaporation-oxidation process is repeated to grow a tunnel barrier with a total thickness of approximately 1 nm. Subsequently, a 30 nm thick layer of Co is evaporated. FM electrodes with different widths are designed (ranging from 120 to 250 nm) to ensure different coercivity of individual contacts and to gain external (magnetic) control over their relative magnetisation orientation. The resist mask is lifted off in acetone for 30 min, and the final device is soaked in IPA and dried with a nitrogen gun.

Devices are then glued to the chip carrier with silver paste and wired using an ultrasonic aluminium wire bonder. The ultrasonic force is optimized to make strong bonds while avoiding the breakage of the $SiO_2$ dielectric layer, which would result in an undesired leakage current between the device and the highly p-doped silicon substrate ($Si^{++}$) used for global gating. The chip carrier with the sample ready for testing is loaded in a cryostat and vacuum-pumped to a pressure of about $10^{-6}$ mbar.

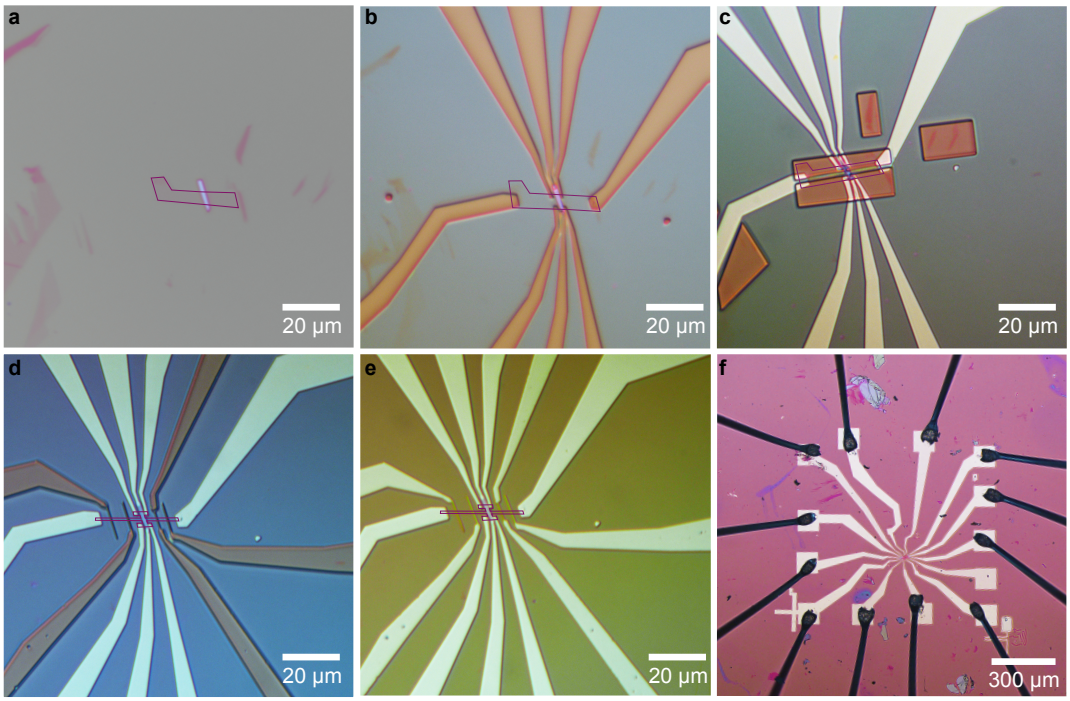


**Fig. 4.2:** Optical image of **a.** TMDC/graphene heterostructure assembled by viscoelastic stamping. **b.** E-beam-patterned mask designed to evaporate NM electrodes. **c.** Mask to etch graphene layer into a channel with hall bars. **d.** Mask for evaporation of FM electrodes. **e.** Final device. **f.** Wire-bonding of the device. Violet lines in the images outline graphene.

## 4.8 Measurement setups

The experiments were performed in three different measurement setups. The setups comprise a cryostat, a switch box, an electromagnet, and a rack with temperature controller, current and voltage sources, and multimeters. One of the setups allows us to set an arbitrary orientation of the sample relative to the external magnetic field without breaking the vacuum. It is a wet $^3He$ cryostat and 9 T magnet. At room temperature, rotation about one axis is achieved by rotating the whole probe in a small electromagnet. The rotation around the second axis is done with an externally manipulated rack and pinion actuator. Although this setup is suitable for measurements down to 300 mK, we have only run room-temperature experiments. Two other setups were used to perform low-temperature measurements. The continuous-flow nitrogen cryostat (Fig. 4.3) relies on continuous replenishment of liquid nitrogen from a storage dewar as the cryogen boils away within the cryostat. Cooling power is determined by the flow rate of the cryogen, which is controlled with a needle valve. The base temperature of the nitrogen cryostat is 77 K. The closed-cycle helium cryostat relies on the circulation of a high-purity (99.999 %) helium gas between the compressor and cold head (expander) through two high-pressure tubes. Our system can reach a base temperature of about 5 K. In addition, any temperature from base to room temperature can be set with a local heater using a proportional-integral-derivative (PID) temperature controller.


**Fig. 4.3:** Measurement setup. **a.** Motorised rotation stage. **b.** Electromagnet. **c.** Cryostat. **d.** Liquid nitrogen input line. **e.** Turbomolecular pump. **f.** PID temperature controller. **g.** Current and voltage sources and multimeters. **i.** Switch box.

The desired measurement configuration is set with an electrical switch box. Alternatively, the sample is grounded between the measurements to protect it from electrostatic discharge. The electromagnet consists of two solenoids with two poles on each side of the cryostat. In the case of the two low-temperature setups, the electromagnet is placed on a rotatory stage to allow for precise control of the angle between the magnetic field and the device's FMs in one coordinate plane determined by how the sample is installed. Magnetic fields up to 0.4, 0.6 and 1 T can be applied depending on the setup used. Current and voltage sources and multimeters are Keithley 6221, Keithley 2400, and Keithley 2182A.

## 4.9 Electrical measurements

A three-point measurement configuration is used to determine the contact resistance. Ideally, the contact resistance of the NM electrodes should be as low as possible. Ti/Pd electrodes in our samples typically display a contact resistance of a few hundred Ω. The contact resistance of the magnetic electrodes must be higher to mitigate the problem of impedance mismatch between cobalt and graphene. Therefore, a thin tunnel barrier between the two materials is introduced. Our approximately 1 nm thick $TiO_2$ tunnel barrier typically has a resistance of a few 10s of kΩ. Crucially, both types of contact must display stable resistance values; otherwise, noise will hide the spin signal. This is an issue especially for the highly resistive tunnel contacts, as noise usually manifests as a percentual fluctuation around a given resistance. The quality of tunnelling contacts can be determined by performing IV sweeps in a two-point configuration. Contrary to transparent contacts, where Ohm's law governs transport, tunnelling contacts display nonlinear IV curves. The deviation from linear behaviour increases with the quality of the tunnel barrier. Therefore, in the case of a barrier with high pinhole density, the characteristic IV curve displays only a slight deviation

from linear behaviour, which leads to a small spin signal. The electrical current applied across the $TiO_2$ tunnel barrier typically has to be limited to around 10 µA; otherwise, the barrier is irreversibly damaged and the magnitude of the spin signal drops considerably.

After all contacts are characterised, the graphene's charge neutrality point (CNP) is determined by changing the position of the Fermi level. This is achieved by sweeping the back-gate voltage $V_g$ between $Si^{++}$ and graphene while measuring longitudinal resistance $R_{xx}$ in a two-point or four-point configuration. The advantage of a four-point configuration over a two-point configuration is that it removes contact resistance, so only $R_{xx}$ of graphene is measured. The relationship between $V_g$ and the carrier density at fixed gate value $n(V_g)$ is

$$V_g - V_{CNP} = \frac{e\, n(V_g)}{C_{SiO_2}}, \tag{4.1}$$

where $C_{SiO_2}$ is the capacitance estimated with the $SiO_2$ dielectric layer; for 440 nm thick $SiO_2$, $C_{SiO_2}/e = 4.9 \times 10^{10}$ $V^{-1}cm^{-2}$.

The $R_{xx}$ vs $V_g$ curve allows us to determine the charge carrier mobility $\mu$ and the residual carrier density $n_0$ at CNP by fitting the experimental data to the expression

$$R_{xx} = \frac{L}{W\, e\, \mu\, n_{\text{total}}}, \tag{4.2}$$

where $L$ is the length and $W$ is the width of the graphene channel. The total carrier density $n_{total}$ is given by [15]

$$n_{total} = \sqrt{n_0^2 + n^2(V_g)}. \tag{4.3}$$

Deviation from $n_0 = 0$, normally expected for pristine graphene, is caused by charged impurities at the graphene/$SiO_2$ interface or in the dielectric itself. Impurities, introduced mainly during the sample fabrication, are also responsible for the shift of $V_{CNP}$ away from 0 V. The position of $V_{CNP}$ indicates whether the doping is of a p-type (positive offset of the CNP) or $n$-type (negative offset of the CNP).

After characterising the graphene channel, the charge transport properties of the 2DM proximitizing graphene and the properties of the graphene-2DM interface are examined. If the material is fairly conductive, the $R_{xx}$ vs $V_g$ curve is measured in a similar way as in the case of graphene. However, semiconducting materials require a different approach. In this case, the 2DM or the interface is voltage-biased with the drain-source voltage $V_{ds}$ and a small current $I_{ds}$ is measured, amplified, converted into voltage and detected with the nanovoltmeter. These measurements allow us to determine the threshold voltage $V_T$ above which the current can flow through the 2DM and the interface. For $V_g \lesssim |V_T|$, the Fermi level is located within the material's band gap, and electronic transport through the material is quenched.

Spin transport experiments are conducted using the current-reversal method. The

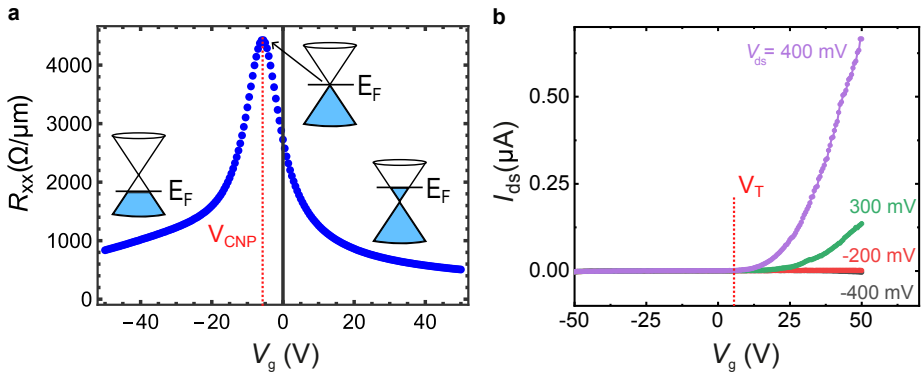


**Fig. 4.4:** Back gate measurements. **a.** $R_{xx}$ vs $V_g$. Resistance reaches a maximum at $V_{CNP}$ where the carrier density is the lowest. Transport is dominated by holes for $V_g < V_{CNP}$, and by electrons for $V_g > V_{CNP}$. **b.** $I_{ds}$ vs $V_g$ for different values of $V_{ds}$. Conduction occurs only for $V_g > V_T$ and positive $V_{ds}$.

advantage of this method over a simple DC measurement is the removal of thermally generated voltage $V_{EMF}$ from the signal. The polarity of a bias current is switched between $I^+$ and $I^-$ repeatedly and voltages $V^+$ and $V^-$ are measured

$$V^+ = V_{EMF} + IR \quad V^- = V_{EMF} - IR \tag{4.4}$$

By combining the two measurements, thermoelectric contribution to the signal can be removed

$$V = \frac{V^+ - V^-}{2} = IR. \tag{4.5}$$

## 4.10 Scanning electron microscopy

Once the device testing is complete, the chip is unloaded from the cryostat, and scanning electron microscopy (SEM) images are taken. In general, the actual distances might slightly deviate from the designed ones due to inaccuracies in the lithography process (e.g. shift or distortion of the mask due to non-ideal beam alignment and sample charging issues). Therefore, it is better to determine the distances between FMs and the proximitized graphene region from the SEM image (Fig. 4.5). In this way, more accurate modelling of the spin transport in the samples is achieved.

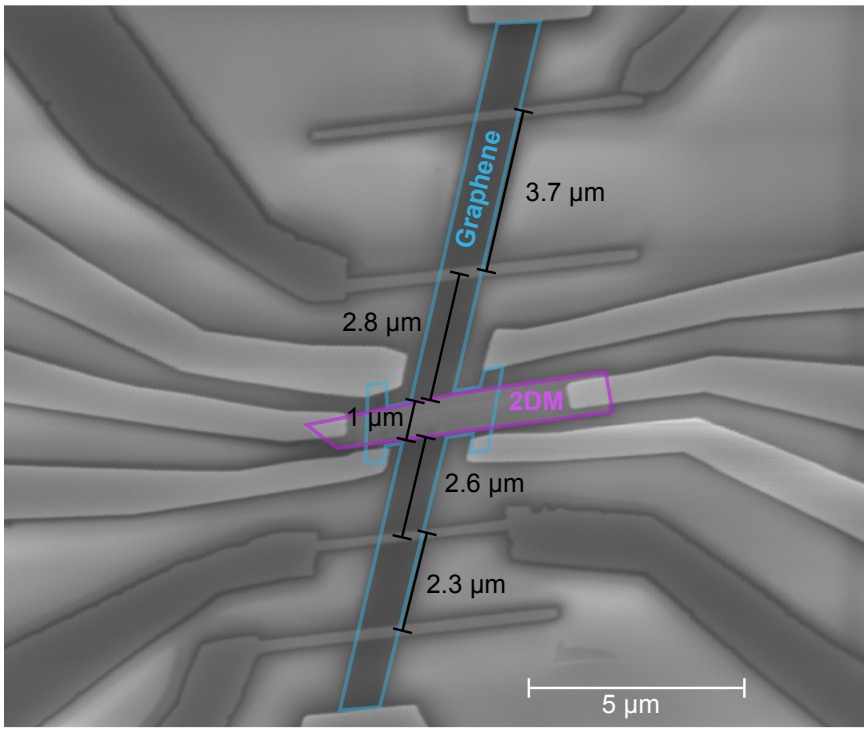


**Fig. 4.5:** SEM image of a representative graphene/2DM device designed to investigate spin transport and charge-spin interconversion. Graphene and 2DM are outlined for clarity. The darker contacts are FM electrodes, and the lighter contacts are NM electrodes.

## References

[1] K. S. Novoselov et al.; "Electric Field Effect in Atomically Thin Carbon Films". *Science* 2004**, 306**, pp. 666–669. DOI: 10.1126/science.1102896.

[2] E. Gao et al.; "Mechanical exfoliation of two-dimensional materials". *Journal of the Mechanics and Physics of Solids* 2018**, 115**, pp. 248–262. DOI: 10.1016/j.jmps.2018.03.014.

[3] Y. Huang et al.; "Reliable Exfoliation of Large-Area High-Quality Flakes of Graphene and Other Two-Dimensional Materials". *ACS Nano* 2015**, 9**, pp. 10612–10620. DOI: 10.1021/acsnano.5b04258.

[4] P. Blake et al.; "Making graphene visible". *Applied Physics Letters* 2007**, 91**, p. 063124. DOI: 10.1063/1.2768624.

[5] D. Bing et al.; "Optical contrast for identifying the thickness of two-dimensional materials". *Optics Communications* 2018**, 406**, pp. 128–138. DOI: 10.1016/j.optcom.2017.06.012.

[6] H. Li et al.; "Rapid and Reliable Thickness Identification of Two-Dimensional Nanosheets Using Optical Microscopy". *ACS Nano* 2013**, 7**, pp. 10344–10353. DOI: 10.1021/nn4047474.

[7] A. C. Ferrari and D. M. Basko; "Raman spectroscopy as a versatile tool for studying the properties of graphene". *Nature Nanotechnology* 2013**, 8**, pp. 235–246. DOI: 10.1038/nnano.2013.46.

[8] J. Yu et al.; "Direct Observation of the Linear Dichroism Transition in Two-Dimensional Palladium Diselenide". *Nano Letters* 2020**, 20**, pp. 1172–1182. DOI: 10.1021/acs.nanolett.9b04598.

[9] Q. Song et al.; "The In-Plane Anisotropy of $WTe_2$ Investigated by Angle-Dependent and Polarized Raman Spectroscopy". *Scientific Reports* 2016**, 6**, p. 29254. DOI: 10.1038/srep29254.

[10] N. Lindvall, A. Kalabukhov, and A. Yurgens; "Cleaning graphene using atomic force microscope". *Journal of Applied Physics* 2012**, 111**, p. 064904. DOI: 10.1063/1.3695451.

[11] M. R. Rosenberger et al.; "Nano-"Squeegee" for the Creation of Clean 2D Material Interfaces". *ACS Applied Materials & Interfaces* 2018**, 10**, pp. 10379–10387. DOI: 10.1021/acsami.8b01224.

[12] A. Castellanos-Gomez et al.; "Deterministic transfer of two-dimensional materials by all-dry viscoelastic stamping". *2D Materials* 2014**, 1**, p. 011002. DOI: 10.1088/2053-1583/1/1/011002.

[13] A. J. Watson et al.; "Transfer of large-scale two-dimensional semiconductors: challenges and developments". *2D Materials* 2021**, 8**, p. 032001. DOI: 10.1088/2053-1583/abf234.

[14] F. Pizzocchero et al.; "The hot pick-up technique for batch assembly of van der Waals heterostructures". *Nature Communications* 2016**, 7**, p. 11894. DOI: 10.1038/ncomms11894.

[15] S. Kim et al.; "Realization of a high mobility dual-gated graphene field-effect transistor with $Al_2O_3$ dielectric". *Applied Physics Letters* 2009**, 94**, p. 062107. DOI: 10.1063/1.3077021.

# Chapter 5

# Modelling anisotropic spin transport

In this chapter, we present the modelling of spin diffusion and precession that are needed in the following chapters to determine the spin lifetime anisotropy in hybrid graphene-TMDC devices. The simulations presented here have been performed by solving analytically the Bloch diffusion equation for spins using the software Wolfram Mathematica ©. The presented modelling results are in preparation for publication "Spin Dynamics in Heterogeneous Nonlocal Spin Devices: Interplay of Isotropic and Anisotropic Spin Relaxation.".

## 5.1 Solution of the Bloch diffusion equation

Spin transport in proximitized graphene devices can be described by the 1D diffusive Bloch equation

$$D_s \frac{\partial^2}{\partial x^2} \vec{\mu}'_s - \gamma_c \, \vec{\mu}'_s \times \vec{B}' - \overline{(\tau'_s)^{-1}} \cdot \vec{\mu}'_s = 0 \, , \tag{5.1}$$

where $\vec{\mu}'_s = (\mu_{x'} \, , \, \mu_{y'} \, , \, \mu_z)$ is the spin-dependent electrochemical potential, $\vec{B}'$ is the magnetic field, and $\overline{(\tau'_s)^{-1}}$ is the diagonal matrix containing the spin relaxation times

$$\overline{(\tau'_s)^{-1}} = \begin{pmatrix} (\tau^s_{x'})^{-1} & 0 & 0 \\ 0 & (\tau^s_{y'})^{-1} & 0 \\ 0 & 0 & (\tau^s_z)^{-1} \end{pmatrix} \tag{5.2}$$

in a rotated coordinate system

$$\begin{aligned} x' &= x \cos(\phi) + y \sin(\phi) \\ y' &= -x \sin(\phi) + y \cos(\phi) \, , \end{aligned} \tag{5.3}$$

where $\phi$ is the angle between $\hat{x}$ and $\hat{x}'$. The need for a rotated coordinate system comes from the possible misalignment between the direction of the injected spins $\hat{y}$ and the two directions in which the spin lifetime is the longest (defined as $\hat{x}'$) and the shortest (defined as $\hat{y}'$). The angle $\phi$ is unknown before measuring the device because

the conscious alignment of $\hat{y}$ with $\hat{x}'$ or $\hat{y}'$ during sample fabrication is not possible and $\phi \neq 0°, 90°$ is expected in most cases.

In the new coordinate system the spin injection along $\hat{y}$, $\vec{J}_{s_0} = (0\ ,\ J_{y_0}\ ,\ 0)$, and the oblique magnetic field defined by the angle $\beta$ in the $yz$ plane, $\vec{B} = \big(0\ ,\ B\cos(\beta)\ ,\ B\sin(\beta)\big)$, are then expressed as follow:

$$\vec{J}'_{s_0} = \Big(J'_{x_0}\ ,\ J'_{y_0}\ ,\ 0\Big) = \Big(J_{y_0}\sin(\phi)\ ,\ J_{y_0}\cos(\phi)\ ,\ 0\Big) \tag{5.4}$$

$$\vec{B}' = \Big(B'_x\ ,\ B'_y\ ,\ B_z\Big) = \Big(B\sin(\phi)\cos(\beta)\ ,\ B\cos(\phi)\cos(\beta)\ ,\ B\sin(\beta)\Big)\ . \tag{5.5}$$

Equation 5.1 can be written as

$$D_s\,\frac{\partial^2}{\partial x^2}\,\vec{\mu}'_s = \begin{pmatrix} (\tau^s_{x'})^{-1} & -\gamma_c\,B_z & \gamma_c\,B'_y \\ \gamma_c\,B_z & (\tau^s_{y'})^{-1} & -\gamma_c\,B'_x \\ -\gamma_c\,B'_y & \gamma_c\,B'_x & (\tau^s_z)^{-1} \end{pmatrix} \vec{\mu}'_s = A\,\vec{\mu}'_s\ . \tag{5.6}$$

whose mathematical solution has the form $\vec{\mu}'_s = e^{k\,x}\,\vec{v}$, with $k$ a constant, and $\vec{v}$ a vector. The second derivative of Eq. 5.6 after substitution is

$$D_s\,k^2\,e^{k\,x}\,\vec{v} = A\,e^{k\,x}\,\vec{v}\ , \tag{5.7}$$

which can be reduced to

$$(A - \lambda\,I)\,\vec{v} = 0\ , \tag{5.8}$$

where $\lambda = D_s\,k^2$ and $I$ is the $3\times 3$ identity matrix. For every root of Eq. 5.8, there is a linearly independent solution of the form $\vec{\mu}'_s = e^{k\,x}\,\vec{v}$. A linear combination of all the independent solutions provides a general solution

$$\vec{\mu}'_s = \sum_{n=1}^{3}\Big(c_n^+\,e^{k_n^+\,x} + c_n^-\,e^{k_n^-\,x}\Big)\,\vec{v}_n\ , \tag{5.9}$$

where $\lambda_n$ and $\vec{v}_n$ are eigenvalues and eigenvectors of $A$ and $k_n^\pm = \pm\sqrt{\lambda_n/D_s}$. Constants $c_n^\pm$ can be determined by setting the boundary conditions, as there are 18 equations for 18 unknown constants.

Boundary conditions for the partially proximitized graphene spin valve, characterised by 5 different regions (see Fig. 5.1a), are

$$\left\{\begin{array}{lll} x = 0: & \vec{\mu}'_{s_I} = \vec{\mu}'_{s_{II}} & \vec{J}'_{s_I} = \vec{J}'_{s_{II}} + \vec{J}'_{s_0} \\ x = l: & \vec{\mu}'_{s_{II}} = \vec{\mu}'_{s_{III}} & \vec{J}'_{s_{II}} = \vec{J}'_{s_{III}} \\ x = l + w_H: & \vec{\mu}'_{s_{III}} = \vec{\mu}'_{s_{IV}} & \vec{J}'_{s_{III}} = \vec{J}'_{s_{IV}} \\ x = L: & \vec{\mu}'_{s_{IV}} = \vec{\mu}'_{s_V} & \vec{J}'_{s_{IV}} = \vec{J}'_{s_V} \\ x \to \pm\infty: & \vec{\mu}'_s = 0 & \vec{J}'_s = 0 \end{array}\right\}\ . \tag{5.10}$$

Regions I, II, IV, and V correspond to pristine graphene, characterised by isotropic

spin relaxation times ($\tau^s_{x'} = \tau^s_{y'} = \tau^s_z$) [1]. Region III is graphene proximitized with another 2DM of width $w_H$, which induces anisotropic spin lifetimes ($\tau^s_{x'} \neq \tau^s_{y'} \neq \tau^s_z$). The FM injector generates the spin current $\vec{J}_{s_0}$ at the border of regions I and II ($x = 0$) and diffuses to both sides. The spin current has a magnitude $J_{y_0} \propto P_\mathrm{i}\, J_c$, where $P_\mathrm{i}$ and $J_c$ are the injector's polarisation and charge current, respectively. An inverse transformation of the coordinate system is performed to obtain $\vec{\mu}_s$ in the original coordinates

$$\begin{aligned} x &= x' \cos(\phi) - y \sin(\phi) \\ y &= x' \sin(\phi) + y \cos(\phi)\ . \end{aligned} \tag{5.11}$$

Thus,

$$\vec{\mu}_s = \Big(\mu_x\ ,\ \mu_y\ ,\ \mu_z\Big) = \Big(\mu_{x'} \cos(\phi) - \mu_{y'} \sin(\phi)\ ,\ \mu_{x'} \sin(\phi) + \mu_{y'} \cos(\phi)\ ,\ \mu_z\Big)\ . \tag{5.12}$$

The detector, located at the border of regions IV and V (at $x = L$), is sensitive only to the component of $\vec{\mu}'_s$ collinear with the FM's magnetisation, which is along $\hat{y}$. Therefore,

$$V_\mathrm{nl} = \frac{P_\mathrm{d}\ \mu_y(L)}{e} = \frac{P_\mathrm{d}\ \Big(\mu_{x'}(L) \sin(\phi) + \mu_{y'}(L) \cos(\phi)\Big)}{e}\ . \tag{5.13}$$

Finally, the effect of the tilting of the FMs' magnetisation under an external magnetic field should be considered. Due to the tilted $\vec{M}$ of the FMs, spins are injected and detected in the $yz$ plane. Injection is defined by

$$\vec{J}^{\prime *}_{s_0} = \left(J'_{x_0} \cos\Big(\gamma(\beta, B)\Big)\ ,\ J'_{y_0} \cos\Big(\gamma(\beta, B)\Big)\ ,\ J_{y_0}\left(\frac{B \sin(\beta)}{B^\mathrm{sat} + B \cos(\beta)}\right)\right) \tag{5.14}$$

instead of Eq. 5.4 and detection is defined by

$$V^*_\mathrm{nl} = \frac{P_\mathrm{d}\ \mu^*_{yz}(L)}{e} \tag{5.15}$$

instead of Eq. 5.13, where

$$\mu^*_{yz}(L) = \mu_y(L) \cos\Big(\gamma(\beta, B)\Big) + \mu_z(L)\ \left(\frac{B \sin(\beta)}{B^\mathrm{sat} + B \cos(\beta)}\right)\ . \tag{5.16}$$

Here, $B^\mathrm{sat}$ is the saturation field and $\gamma(\beta, B)$ is the out-of-plane tilt of the FMs when a magnetic field of magnitude $B$ is applied at an angle $\beta$ and was defined by Eq. 3.15. In the following sections, we set $B^\mathrm{sat} = 1$ T when simulating the precession lineshapes, which approximately corresponds to the experimentally determined value in our devices (FM injector/detector made of 30 nm thick Co).

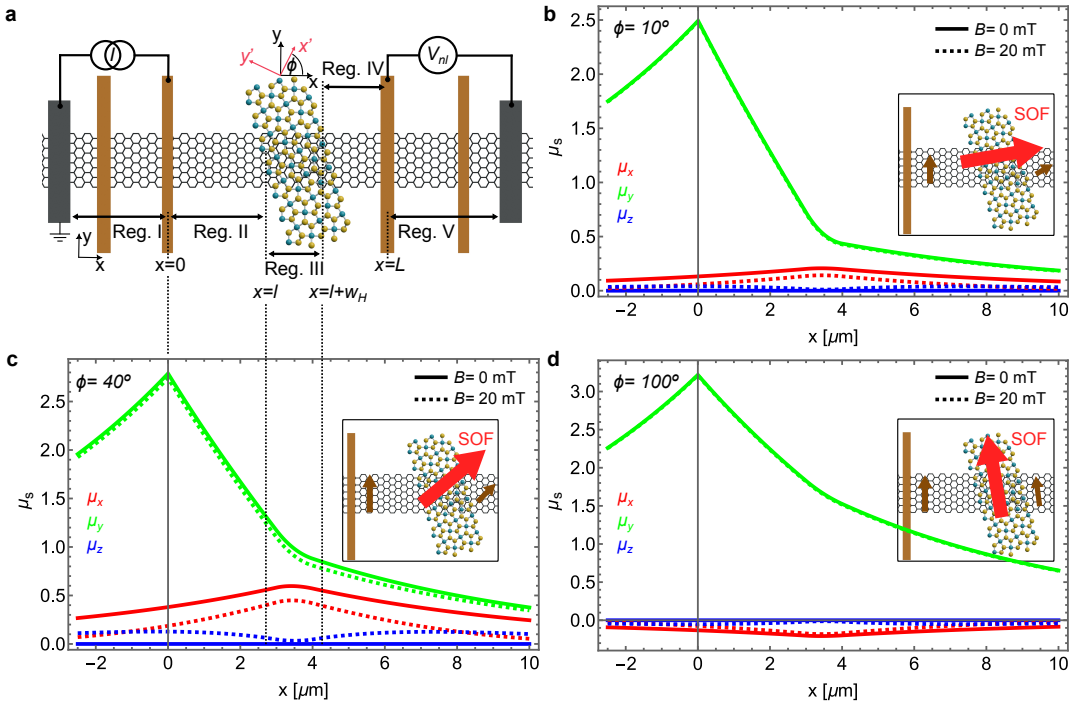


**Fig. 5.1:** Spin-dependent electrochemical potential across the graphene/$PdSe_2$ device. **a.** Schematics of the graphene/$PdSe_2$ device regions. **b**,**c**,**d.** Spin-dependent electrochemical potentials along $\hat{x}$, $\hat{y}$, and $\hat{z}$ ($\mu_x$, $\mu_y$, $\mu_z$) across the device when $\phi = 10°$ (**b**), $\phi = 40°$ (**c**), and $\phi = 100°$ (**d**). The red arrow represents the dominant SOF ($\hat{x}'$).

## 5.2 Calculated spin density across anisotropic samples

Figures 5.1b-d show the calculated $\mu_x$, $\mu_y$ and $\mu_z$ across the graphene/TMDC device for three different orientations of the dominant SOF (see the insets of Figs. 5.1b-d). The geometry of the device and set parameters are

$$\left\{\begin{array}{ll} l = 3\ \mu\text{m} & \tau^s_{x'} = 200\ \text{ps} \\ w_H = 1\ \mu\text{m} & \tau^s_{y'} = 20\ \text{ps} \\ D_s = 0.05\ \text{m}^2\text{s}^{-1} & \tau^s_z = 5\ \text{ps} \\ \tau_s = 1\ \text{ns} & \phi = var. \end{array}\right\} \tag{5.17}$$

which are typical values for our graphene/$PdSe_2$ devices.

By definition, the dominant SOF is along $\hat{x}'$ and its direction is defined by the angle $\phi$, which is varied to see its effect on $\vec{\mu}_s(x)$. In Fig. 5.1b, $\phi = 10°$, i.e. the dominant SOF is almost aligned with the graphene channel. Such an orientation of the SOF induces a sharp decrease of $\mu_y$, where the spin lifetime is significantly shorter. Moreover, since the component of $\mu_y$ parallel to $\mu_{x'}$ has a spin lifetime 10 times longer than that parallel to $\mu_{y'}$, the spins effectively rotate in the proximitized region, leading to the generation of a non-zero $\mu_x$. The generated $\mu_x$ then diffuses equally to both sides of the channel from below the TMDC. The effective rotation of the spins towards $\hat{x}$ is even more pronounced when $\phi = 40°$ (Fig. 5.1c). As the generated $\mu_x$ has a relatively large magnitude in this case, the magnetic field $B_y$

induces a noticeable out-of-plane spin precession of this component, leading to the appearance of the component $\mu_z$ (dashed blue line in Fig. 5.1c). In Fig. 5.1d, the dominant SOF is close to the spin injection direction ($\phi = 100°$) and a much less pronounced decrease in $\mu_y$ is observed compared to $\phi = 10°$ and $40°$. The small misalignment between the dominant SOF and $\hat{y}$ leads to the generation of a small (negative) $\mu_x$.

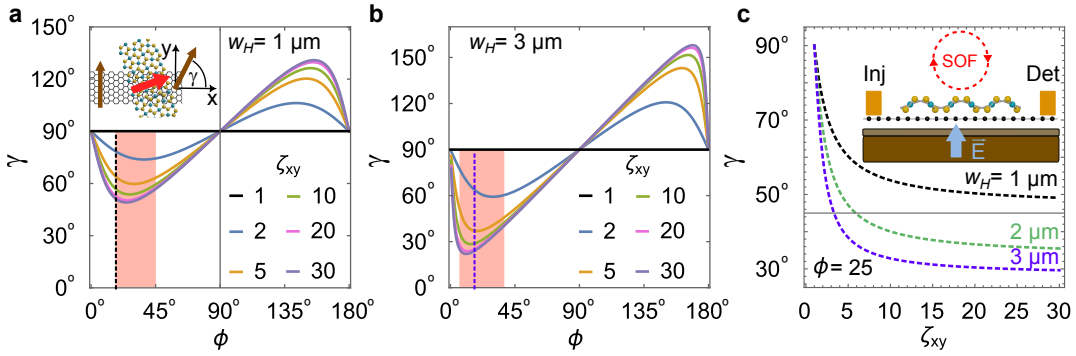


**Fig. 5.2:** Spin rotation as a function of $\phi$, $\zeta_{xy}$, and $w_H$. **a,b.** Direction of spins exiting the anisotropic region as a function of $\phi$ for different $\zeta_{xy}$ when $w_H = 1$μm (**a**) and $w_H = 3$μm (**b**), respectively. The direction is defined by an angle $\gamma$ (see inset of **a**). The red areas represent the range of $\phi$ where the spin rotation is largest. The dashed vertical lines outline $\phi = 25°$. **c.** Direction of the exiting spins as a function of $\zeta_{xy}$ at $\phi = 25°$ for $w_H = 1, 2, 3$μm. Tuning the SOF (and thus $\zeta_{xy}$) by an external electric field (inset in **c**) could be used to manipulate spins in spin-logic devices.

The extent to which spins exiting an anisotropic region are effectively rotated depends on $\phi$, $\zeta_{xy}$ and $w_H$. Figures 5.2a,b shows this effective rotation as a function of $\phi$ for different $\zeta_{xy}$ in a device with $w_H = 1$ μm and $w_H = 3$ μm, respectively. $\zeta_{xy}$ is varied by changing $\tau_x^s = 20, 40, 100, 200, 400, 600$ ps and keeping the other in-plane lifetime constant, $\tau_y^s = 20$ ps. The exiting spins point in the direction defined by angle $\gamma$ (see the inset of Fig 5.2a). Naturally, no deviation from the spin injection direction $\gamma = 90°$ is observed in the isotropic case ($\zeta_{xy} = 1$). However, spins are rotated when $\zeta_{xy} > 1$. The magnitude of the rotation grows with $\zeta_{xy}$ and $w_H$. Figure 5.2c shows $\gamma$ as a function of $\zeta_{xy}$ at $\phi = 25°$ for $w_H = 1, 2, 3$ μm and demonstrates that the direction of spin polarisation can be significantly rotated away from the spin injection axis when $\zeta_{xy}$ is large. Even for $\zeta_{xy} = 15$ spins are still rotated by $\approx 39°, 53°$, and $70°$ ($= 90° - \gamma$) when $w_H = 1, 2, 3$ μm, respectively. This means that spin orientation in the device can be manipulated by modulating $\zeta_{xy}$.

The in-plane anisotropy results from induced SOFs in graphene and can be in principle controlled by an external electric field. Thus, a graphene device showing gate-tunable in-plane anisotropy would allow for spin manipulation constituting an important step towards developing spin-logic devices. However, not that rotation must be accompanied by significant spin relaxation, along the direction with short spin lifetime.

## 5.3 Simulations of curves in spin valve configuration

Next, let us examine the effect of $\phi$ on the lineshape and magnitude of $R_{\mathrm{nl}}$ vs $B_y$ curves, i.e with the magnetic field along the orientation of the injected spins ($\tau^s_{x'} = 200$ ps, $\tau^s_{y'} = 20$ ps $\tau^s_z = 5$ ps). The injector-to-detector distance is set to $L = 11$ µm. As shown in Fig. 5.3a, the magnitude of the spin signal increases as the angle increases from 0° to 90°. The anomalous decrease in $R_{\mathrm{nl}}$ as a function of $B_y$ is seen only for intermediate angles ($\phi \neq 0°, 90°$). For $\phi = 0°$, spins are injected perpendicularly to the long spin lifetime axis $\hat{x}'$, and there is no component along $\hat{x}'$. For $\phi = 90°$ spins are injected along $\hat{x}'$ and there is no component along $\hat{y}'$. Therefore, no effective spin rotation occurs in either of the two cases.

Figures 5.3b,c show the effect of varying $\tau^s_z$ and $\tau^s_{x'}$ on the lineshape of $R_{\mathrm{nl}}$ vs $B_y$ curves for $\phi = 40°$ and constant $\tau^s_{y'} = 20$ ps. When $\tau^s_{x'} = 20$ ps is kept constant, even a large variation of $\tau^s_z$ (5 ps $\rightarrow$ 400 ps) causes only a slight change in the lineshape (Fig. 5.3b). In contrast, changing $\tau^s_{x'}$ strongly influences the lineshape and magnitude of the curves (Fig. 5.3c). As $\tau^s_{y'}$ is kept constant, the in-plane spin lifetime anisotropy $\zeta_{xy}$ changes from $\zeta_{xy} = 1$ (for $\tau^s_{x'} = 20$ ps) to $\zeta_{xy} = 20$ (for $\tau^s_{x'} = 400$ ps), which leads to a strong modulation of the lineshape.

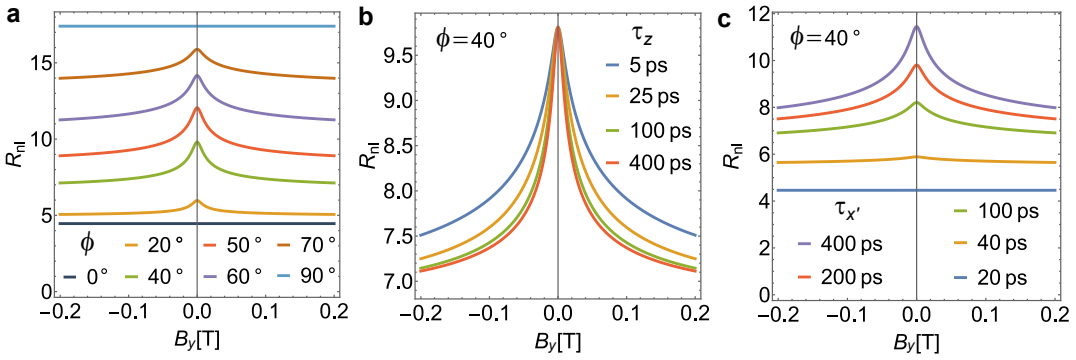


**Fig. 5.3:** Influence of $\phi$, $\tau^s_z$, and $\tau^s_x$ on the lineshape of spin valve curves. **a**,**b**,**c.** Influence of $\phi$ (**a**), $\tau^s_z$ (**b**), and $\tau^s_x$ (**c**) on the lineshape and magnitude of $R_{\mathrm{nl}}$ vs $B_y$ curves. The constant parameters have the same value as in Box 5.17.

## 5.4 Simulations of in-plane precession curves

Next, we examine the influence of geometric parameters, namely, the injector's and detector's distances from the TMDC. In the case of $R_{\mathrm{nl}}$ vs $B_y$, only the total injector-to-detector distance $L$ matters. Naturally, it influences the magnitude of the measured signal; however, it does not affect the overall shape. In contrast, for $R_{\mathrm{nl}}$ vs $B_z$ curves, the distance of the injector ($l$) and the detector ($l_d$) from the TMDC are important geometric parameters (see Fig. 5.4a).

Figure 5.4b illustrates the lineshape of the $R^{\mathrm{N}}_{\mathrm{nl}}$ vs $B_z$ curves ($R^{\mathrm{N}}_{\mathrm{nl}} = R_{\mathrm{nl}}/R^0_{nl}$) versus $l_d$. When $l_d < l$, the deeper minimum appears for negative $B_z$. When $l_d = l$, i.e. when $l_d = 3$ µm, the two minima have the same magnitude and the precession curve is

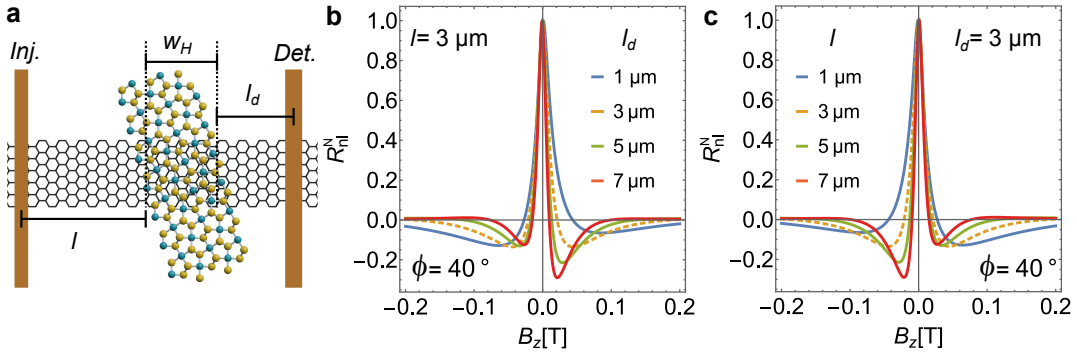


**Fig. 5.4:** Influence of the geometry on the lineshape of in-plane precession curves **a.** Geometric parameters of the device: distance of the injector ($l$) and detector ($l_d$) from the TMDC. **b**,**c.** $R_{nl}^N$ vs $B_z$ precession curves for different $l_d$ (**b**) and $l$ (**c**). In a symmetric device ($l \approx l_d$, dashed line), the precession curve is symmetric. All the other parameters are kept constant (see Box 5.17).

symmetric $R_{nl}(B_z) = R_{nl}(-B_z)$. Finally, when $l_d > l$, the deeper minimum appears for positive $B_z$. Figure 5.4c shows that changing $l_d$, while keeping $l$ constant, results in spin precession profiles that mirror the ones in Fig. 5.4b.

Experimentally, this can be observed when interchanging the role of the injector and detector in an asymmetric device. Thus, the distances of the FM electrodes from the TMDC are important parameters to consider when designing devices for experimental investigation of in-plane anisotropy. Unveiling in-plane anisotropy in devices with $l \approx l_d$ is more challenging because the precession curves remain symmetric around $B_z = 0$. In a symmetric device, changing $\phi$ influences the depth of both extrema equally (Fig. 5.5a). Therefore, it is beneficial to design devices with pronounced geometric asymmetry, as it leads to different depths of the two extrema for most $\phi$, providing a strong signature of in-plane anisotropy (Fig. 5.5b,c).

Identifying the anisotropy could still be challenging when $\phi \approx 90°$ (Fig. 5.6a). If $\phi \approx 90°$, having a device with a wider TMDC flake improves the visibility of the induced anisotropy, as it leads to a complete suppression of the negative oscillation (Fig. 5.6b).

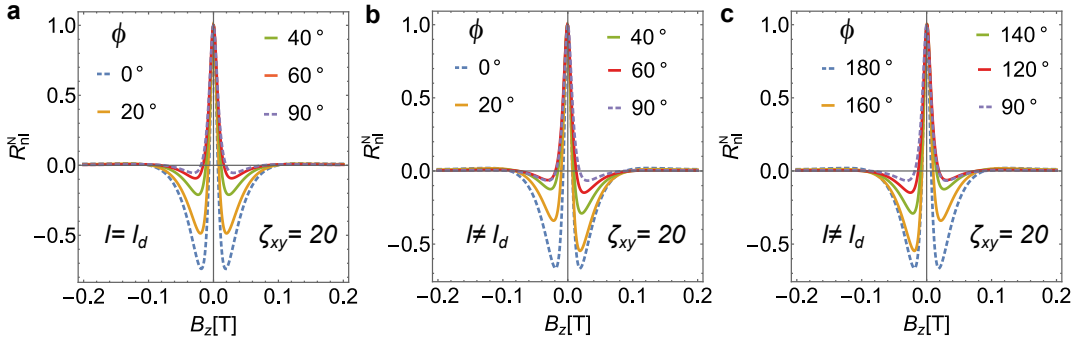


**Fig. 5.5:** Dependence of the lineshape on $\phi$ in a symmetric and asymmetric device. **a.** $R_{nl}^N$ vs $B_z$ precession curves for different $\phi$ in a symmetric device ($l = l_d$). Precession curves remain symmetric $R_{nl}^N(B_z) = R_{nl}^N(-B_z)$ irrespective of $\phi$ in a symmetric device. **b**,**c.** $R_{nl}^N$ vs $B_z$ precession curves for different $\phi$ in an asymmetric device ($l \neq l_d$) in the range <0°, 90°> (**b**) and <90°, 180°> (**c**). Notice the symmetry $R_{nl}^N(B_z, \phi) = R_{nl}^N(-B_z, (180° - \phi))$. Precession curves are symmetric even in an asymmetric device when $\phi = 0°$ or 90° (dashed lines).

In contrast, when $\phi \approx 0°$, the in-plane anisotropy is still noticeable even for narrower TMDC (Fig. 5.6c), with the anisotropy becoming more visible in devices with wider TMDC (Fig. 5.6d). Nevertheless, it is important to note that an increase in the TMDC's width significantly reduces the magnitude of the spin signal (not apparent here as all curves are normalised). Thus, spin transport can only be experimentally investigated in graphene channels partially covered with a relatively narrow TMDC flake to measure appreciable spin signals.

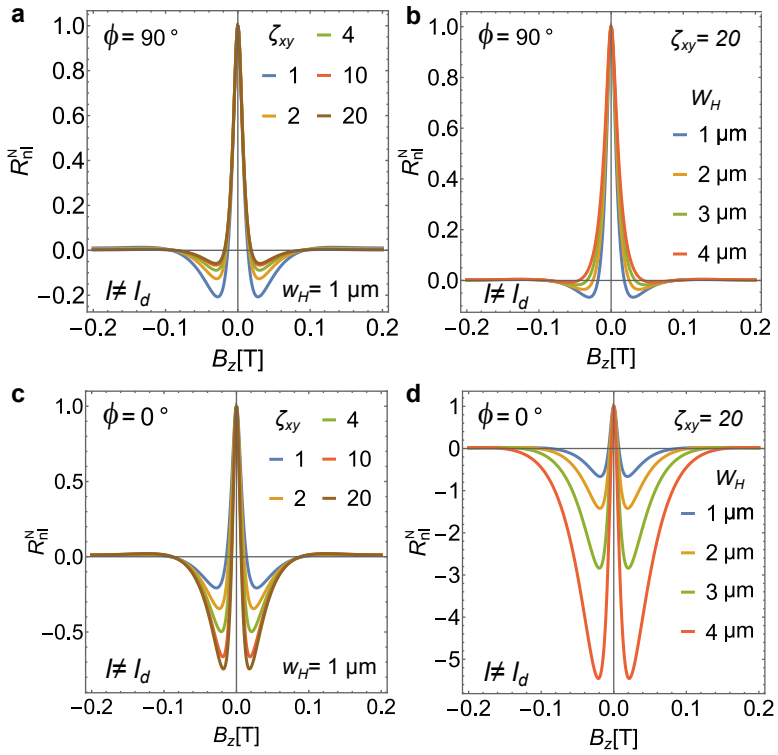


**Fig. 5.6:** Dependence of the in-plane precession lineshape on $\zeta_{xy}$ and $w_H$ for $\phi = 90°$ and $0°$. **a**,**b.** $R^N_{nl}$ vs $B_z$ precession curves for $\phi = 90°$ when $\zeta_{xy}$ (**a**) and $w_H$ (**b**) are modulated. **c**,**d.** $R^N_{nl}$ vs $B_z$ precession curves for $\phi = 0°$ when $\zeta_{xy}$ (**c**) and $w_H$ (**d**) is modulated.

## 5.5 Simulations of oblique precession curves

The out-of-plane precession can be induced by an in-plane magnetic field applied perpendicularly to the easy axis of the FMs. However, a small saturation field and inhomogeneous rotation of the magnetisation of the FMs complicate the data analysis [2]. The out-of-plane lifetime $\tau^s_z$ is most accurately determined using oblique precession measurements (see Sec. 3.3). Figure 5.7 shows the precession curves for representative angles $\beta = 0°, 20°, 30°, 40°, 60°, 90°$ (top to bottom) when $\tau^s_{x'} = 200$ ps, $\tau^s_{y'} = 20$ ps, $\tau^s_z = 5$ ps and $\phi = 10°, 40°$, and $100°$, respectively. Figures. 5.7a,b,c and Figures 5.7d,e,f display oblique precession curves for symmetric ($l = l_d = 5$ µm) and asymmetric ($l = 1$ µm, $l_d = 9$ µm) devices, respectively, and $w_H = 1$ µm. As the spins acquire all three spatial components under oblique magnetic fields, the

lineshape of the curves is also sensitive to $\tau^s_{x'}$ and $\tau^s_{y'}$. This is why the lineshape of the curves is sensitive to $\phi$ even for oblique magnetic fields. In an asymmetric device, the oblique precession curves remain asymmetric. Fitting a set of oblique data (especially those displaying asymmetric features) accurately determines the spin lifetimes $\tau^s_{x'}$, $\tau^s_{y'}$, $\tau^s_z$ and angle $\phi$.

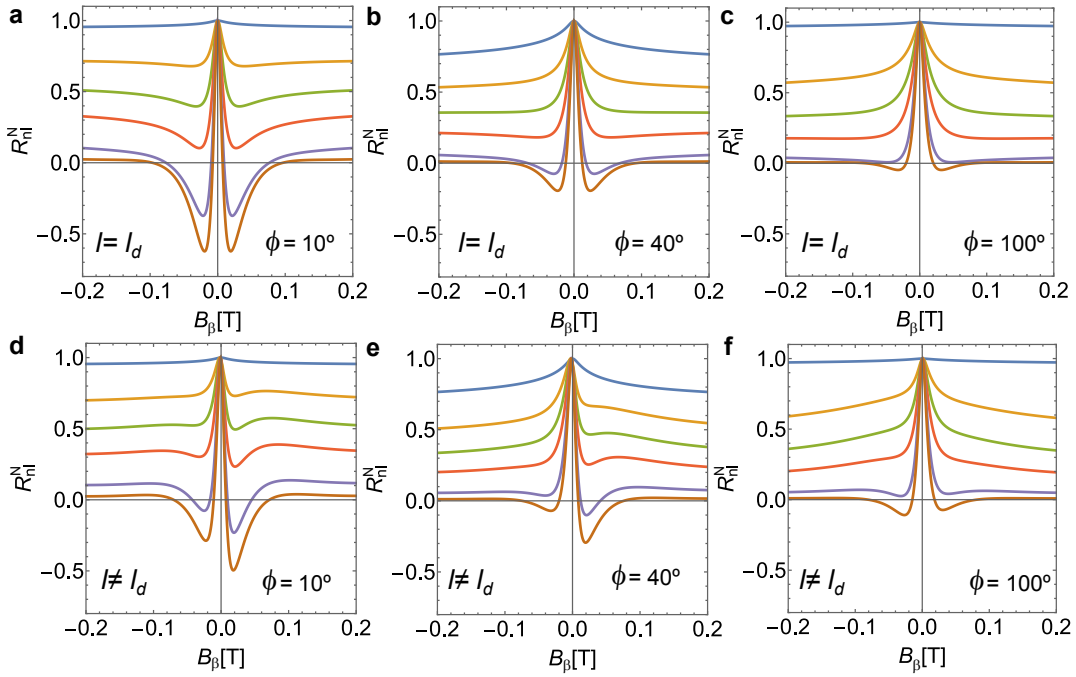


**Fig. 5.7:** Dependence of the lineshape of oblique precession curves on $\phi$ in a symmetric and asymmetric device. **a.** $R^N_{nl}$ vs $B_z$ precession curves for different $\phi$ in a symmetric device ($l = l_d$). **b,c.** $R^N_{nl}$ vs $B_z$ precession curves for different $\phi$ in an asymmetric device ($l \neq l_d$) in the range <0°, 90°> (**b**) and <90°, 180°> (**c**). $\beta = 0°, 20°, 30°, 40°, 60°, 90°$ top to bottom.

Figure 5.8 shows pronounced changes in the lineshape of precession curves for an asymmetric device when $\tau^s_z$ is gradually reduced from 400 ps to 5 ps. The oblique angle is set to $\beta = 45°$ and the influence of the lineshape on $\tau^s_z$ is investigated for $\phi = 10°, 40°$ and $100°$. Figure 5.8 shows that oblique precession experiments are highly sensitive to $\tau^s_z$, regardless of the specific value of $\phi$.

In conclusion, this chapter presented the solution of Bloch diffusion equations for a partially proximitized graphene channel. It predicted the lineshape of precession curves for various magnetic field orientations. The misalignment between the spin injection direction and the long spin lifetime direction was demonstrated to cause an effective rotation of the spins. The simulations demonstrate the lineshape dependence of $R_{nl}$ vs $\vec{B}$ curves on the device geometry and the spin lifetime hierarchy. The asymmetric devices display features absent in the symmetric ones; therefore, they were identified as a better choice for the experiments. The strong in-plane SOF along $\hat{x}'$ causes an anomalous decrease of $R_{nl}$ as a function of $B_y$ if $\phi \neq 0°, 90°$. The anomalous decrease is associated with the in-plane anisotropy-induced rotation of the spins below the TMDC and the subsequent out-of-plane precession of the rotated spin components.

Taking into account the the observed dependences of the precession curves on spin transport parameters, the most suitable protocol for experimental determination of $\tau^s_{x'}$, $\tau^s_{y'}$, $\tau^s_z$ and $\phi$ can be identified. The protocol involves:

1. Fabrication of devices with pronounced geometrical asymmetry ($l \neq l_d$).
2. Determination of $\tau_s$, $D_s$, and $P_i P_d$ in the reference graphene region.
3. Determination of $\tau^s_{x'}$, $\tau^s_{y'}$, and $\phi$ in the proximitized region from the $R_{nl}$ vs $B_z$ data.
4. Independent verification of $\tau^s_{x'}$, $\tau^s_{y'}$, $\phi$, and first estimation of $\tau_z$ in the proximitized region from the $R_{nl}$ vs $B_y$ data.
5. More accurate determination of $\tau^s_z$ from the $R_{nl}$ vs $B_\beta$ dataset.
6. Verification of extracted $\tau^s_{x'}$, $\tau^s_{y'}$, $\tau^s_z$, and $\phi$ by interchanging the role of injector and detector and repeating previous measurements.

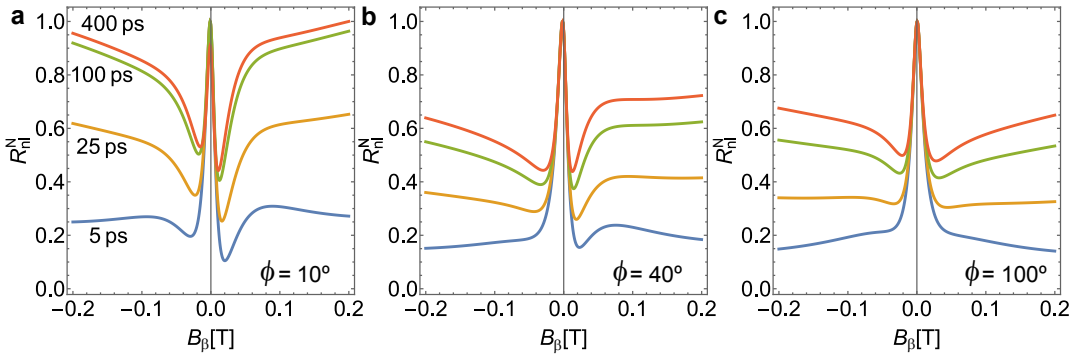


**Fig. 5.8:** Influence of $\tau^s_z$ on the lineshape of 45° oblique precession curves ($\tau^s_z = 400, 100, 25$, and 5 ps top to bottom). **a.** $\phi = 10°$. **b.** $\phi = 40°$. **c.** $\phi = 100°$.

## References

[1] B. Raes et al.; "Determination of the spin-lifetime anisotropy in graphene using oblique spin precession". *Nature Communications* 2016, **7**, p. 11444. DOI: 10.1038/ncomms11444.

[2] B. Raes et al.; "Spin precession in anisotropic media". *Physical Review B* 2017, **95**, p. 085403. DOI: 10.1103/PhysRevB.95.085403.

# Chapter 6

# Anisotropic spin dynamics in graphene/$PdSe_2$ heterostructures

Spin transport in vdW heterostructures comprising graphene and 2H-TMDCs is characterised by the large anisotropy between in-plane and out-of-plane spin lifetimes. Nevertheless, spins relax isotropically within the graphene plane due to the $\mathcal{C}_{3v}$ symmetry of these heterostructures. The dominant SOFs for spin relaxation for in-plane spins point out-of-plane and emerge due to the strong proximity-induced valley-Zeeman SOC. In contrast, symmetry-free heterostructures of 2D crystals with mutually incompatible lattices have been predicted to show in-plane anisotropic spin relaxation [1]. This chapter demonstrates a giant in-plane spin lifetime anisotropy in graphene proximitized with pentagonal crystal $PdSe_2$. Furthermore, the induced SOC is shown to be highly tunable by the carrier density, opening avenues for gate-controlled spintronic devices. The results presented have been submitted for publication "Room-temperature anisotropic in-plane spin dynamics in graphene induced by $PdSe_2$ proximity"; J. F. Sierra*, J. Světlík*, W. Savero Torres, L. Camosi, F. Herling, T. Guillet, K. Xu, J. S. Reparaz, V. Marinova, D. Dimitrov, and S. O. Valenzuela in *Nature Materials*.

## 6.1 Introduction

Strongly anisotropic spin relaxation has been observed up to room temperature in hybrid graphene/TMDCs systems [2–4], with the out-of-plane lifetime $\tau_{\perp}^{s}$ being much larger than in-plane spin lifetime $\tau_{\parallel}^{s}$ due to the valley-Zeeman SOC [5, 6] (see Sec. 2.8). While a Rashba SOC has also been predicted and observed, the SOFs and the spin relaxation in the graphene plane remain isotropic due to the $\mathcal{C}_{3v}$ symmetry of the heterostructure.

In-plane spin lifetime anisotropy has not been conclusively demonstrated. Only indications have been observed at low temperatures in the intrinsically anisotropic black phosphorus [7]. A recent theoretical study has proposed that giant in-plane anisotropy could be achieved in graphene when integrated into a heterostructure with orthorhombic SnTe, a buckled vdW material with disparate crystalline symmetries

[1] (see Sec. 2.8). Therefore, this, or a similar low-symmetry heterostructure, could enable gate-tunable in-plane anisotropic transport at room temperature.

We note that unconventional CSI components have been observed in graphene combined with low-symmetry semimetals $MoTe_2$ [8, 9] and $WTe_2$ [10, 11]. However, the bulk contributions from these semimetals complicate the analysis, making it challenging to isolate the CSI occurring in graphene by proximity effects and identify the corresponding proximity-induced spin textures.

## 6.2 Graphene/$PdSe_2$ device design

This chapter investigates spin transport in heterostructures made of graphene and $PdSe_2$, a low-crystal symmetry material. $PdSe_2$ is a semiconducting TMDC with a band gap of about 1.3 eV in monolayer form that decreases with thickness [12, 13]. Similar to SnTe, its unit cell is orthorhombic and both materials are centrosymmetric, however, the space group is Pbca (61) and Pnma (62) for $PdSe_2$ and SnTe, respectively. A monolayer of $PdSe_2$ comprises irregular pentagons and has a buckled structure along the $a$-axis. Pentagonal $PdSe_2$, vertically stacked with hexagonal graphene, forms a symmetry-free heterostructure (Fig. 6.1a).

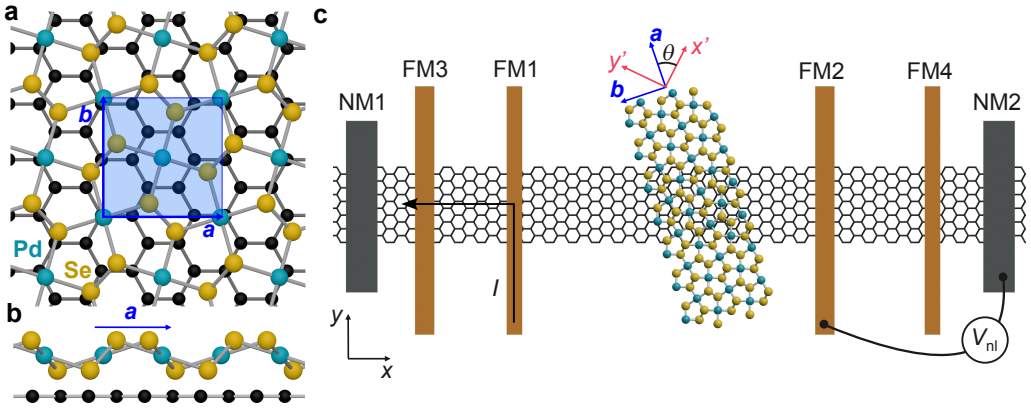


**Fig. 6.1:** Graphene/$PdSe_2$ device geometry. **a**,**b.** Top (**a**) and side (**b**) view of the pentagonal lattice of monolayer $PdSe_2$ on hexagonal graphene resulting in symmetry-free heterostructure. The rectangle denotes the unit cell. The side view shows the buckled structure along the $a$-axis. **c.** Device schematic: monolayer graphene spin channel with four FM contacts along $\hat{y}$ and two NM contacts. Blue arrows indicate $PdSe_2$ crystalline axes $a$ and $b$; red arrows denote in-plane spin directions $\hat{x}'$ and $\hat{y}'$ for the longest and shortest spin lifetimes, respectively. The angle $\theta$ characterises the rotation between $\hat{x}'$ and $a$.

The valley-Zeeman SOC imprinted into graphene by TMDCs has been described as directly induced by interlayer tunnelling [14]. Within this band-to-band tunnelling framework, electrons in graphene can tunnel to any of the three atomic layers of $PdSe_2$, however, the probability of reaching the first Se layer is exponentially higher. Consequently, considering the proximity SOC in these terms, the buckled structure of $PdSe_2$ —characterised by its highly anisotropic arrangement of Se atoms (Fig. 6.1b) — may give rise to novel spin textures with strong in-plane anisotropy.

To test this hypothesis, we have characterised the spin lifetimes in graphene/$PdSe_2$ heterostructures along three orthogonal axes using the non-local spin device illustrated in Fig. 6.1c. The experiments systematically investigate in-plane and out-of-plane spin precession with selected magnetic field $\vec{B}$ orientations [15–17], relative to the $\hat{x}$, $\hat{y}$ and $\hat{z}$ axes. Here, $\hat{z}$ is perpendicular to the graphene plane and $\hat{y}$ is along the length of the FM electrodes, FM1-FM4. A $PdSe_2$ single crystal is stacked with graphene between electrodes FM1 and FM2. It is beneficial to place the $PdSe_2$ off-centre, i.e. closer to one of the electrodes, as it leads to the appearance of spin precession features in the lineshape that would be otherwise absent (for details see Sec. 5.4). $PdSe_2$ introduces proximity SOC in graphene, which modifies the spin dynamics and relaxation. The spin lifetimes $\tau^s_{x'}$, $\tau^s_{y'}$, $\tau^s_{z'}$, along $\hat{x}'$, $\hat{y}'$ and $\hat{z}' = \hat{z}$, directly correlate with the induced SOC and spin textures. As introduced in Chapter 5, we adopt the convention that $\hat{x}'$ ($\hat{y}'$) points along the in-plane direction for which the spin lifetime is the longest (shortest).

Because of the low symmetry of the heterostructure, the induced spin textures are not necessarily aligned to the crystalline axis of graphene or $PdSe_2$. The angle $\theta$ characterises the $\hat{x}'$ orientation relative to $\hat{a}$, the crystallographic orientation of the $PdSe_2$. The distance between FM1 and FM2 is chosen to be approximately 10 µm in the fabricated devices. This length is sufficient to ensure large-angle spin precession and complete dephasing of the spin accumulation perpendicular to $\vec{B}$ at moderately low $B$ for spins diffusing between FM1 and FM2 [15] (see Sec. 3.2). Two additional FM electrodes, FM3 and FM4, in combination with FM1 and FM2, form two reference devices for characterising the spin dynamics in pristine graphene.

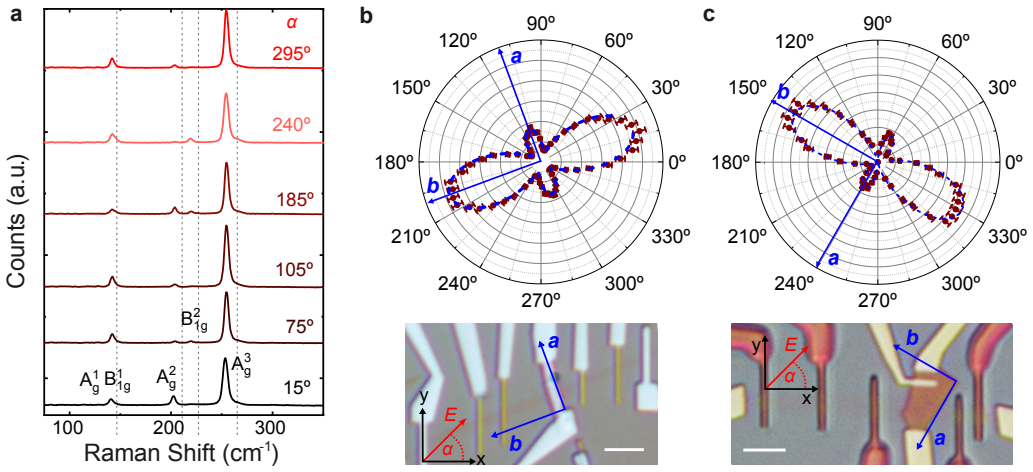


**Fig. 6.2: a.** Polarised Raman spectra of $PdSe_2$ flake on Device 1 for several different $\alpha$. The intensity of $A^2_g$ mode shows pronounced dependence on the polarisation of incident light. **b**,**c.** Polar plots of the angular dependence (top) of Device 1 (**b**) and Device 2 (**c**) and their optical images (bottom).

The crystallographic directions of $PdSe_2$ flakes in both devices were identified by polarised Raman spectroscopy. Figure 6.2a illustrates Raman spectra under parallel polarisation configuration for several rotation angles $\alpha$ between 0° and 360° relative to $\hat{x}$. $PdSe_2$ has Raman modes with symmetry assignments $A_g$ and $B_{1g}$. The $A_g$ peaks display intensity modulation with a 180° period, enabling the identification of the

crystalline axes of the crystal [18]. The angular dependence of the intensity of the $A_g^2$ mode for $PdSe_2$ flake on Device 1 (Device 2) is shown in Fig. 6.2b (c), indicating that the *a* axis is tilted 20° counter-clockwise from $\hat{y}$ in the case of Device 1 and 30° clockwise from $\hat{y}$ in for Device 2.

## 6.3 Back-gate characterisation of graphene/$PdSe_2$ devices

A back-gate voltage applied to the $Si/SiO_2$ substrate allows us to tune the carrier density in the graphene/$PdSe_2$ heterostructures. Figure 6.3 shows two fabricated graphene/$PdSe_2$ devices and their back-gate characterisation. Device 1 comprises a $PdSe_2$ crystal that is 1.4 µm wide and 20 nm thick (Fig. 6.3a). The CNP for both pristine graphene (Fig. 6.3b) and proximitized region (Fig. 6.3c) is close to 0 V demonstrating that the graphene channel is undoped. Device 2 was fabricated using a 2.8 µm wide and 6 nm thick flake of $PdSe_2$. A thinner flake (with a wider band gap in dispersion spectra), was selected to limit potential parallel conduction through $PdSe_2$ in the proximitized region. In Device 2, graphene is slightly n-doped with the CNP approximately at -12 V in the reference region (Fig. 6.3e). The back-gate measurement of the proximitized region shows two maxima (Fig. 6.3f). The position of the left maximum coincides with the one measured in the reference region. The second peak at around 18 V hints at possible charge transfer between graphene and $PdSe_2$ in the proximitized region (p-doping of proximitized graphene).

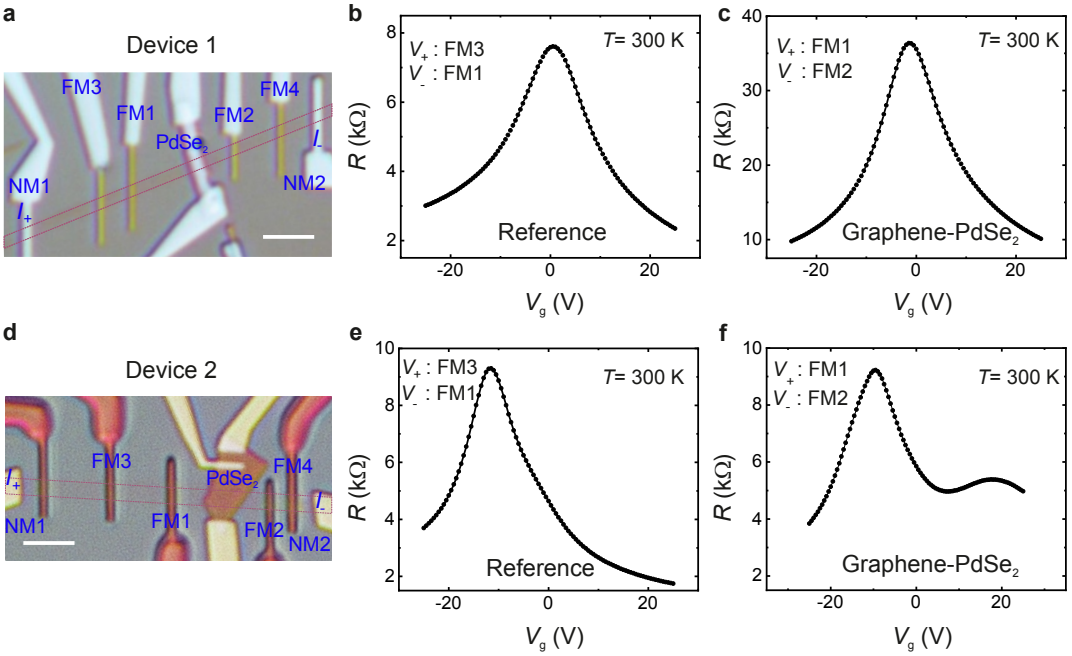


**Fig. 6.3: a.** Device 1 comprises a narrower and thicker $PdSe_2$ flake placed on a graphene channel and FM/NM electrodes. **b**,**c.** Back-gate measurements in the reference (**b**) and proximitized (**c**) region of Device 1 demonstrate a superior graphene quality. **d.** Device 2 comprises a wider and thinner $PdSe_2$ flake on a graphene channel and FM/NM electrodes. **e**,**f.** Back-gate measurements in reference (**e**) and proximitized (**f**) region indicate n-doped reference graphene and p-doped proximitized graphene.

Figures 6.4a,b show two configurations, used to investigate the $V_g$ dependence of the drain-source current $I_{ds}$ across graphene/$PdSe_2$ interface and $PdSe_2$ alone, respectively. The 20-nm thick $PdSe_2$ layer in Device 1 has a small estimated bandgap ($\sim$ 30 meV) and a finite, albeit very low, conductivity $\sigma_{PdSe_2}$ at room temperature [12]. The $PdSe_2$ exhibits ambipolar transport behaviour, transitioning from hole to electron carriers across the measured $V_g$ range, with the lowest conductivity around $V_g \approx -12$ V (Fig. 6.4c,d). The behaviour of the 6-nm thin $PdSe_2$ in Device 2 is investigated at a low temperature (77 K). The $I_{ds}$ remains undetectable for all measured $-50$ V $< V_g <$ 50 V at negative and low positive $V_{ds}$, while sharply increasing only when $V_{ds} > 0.2$ V and positive $V_g$ is applied (Fig. 6.4e,f). This behaviour demonstrates the presence of a wider band gap in 6-nm $PdSe_2$ that suppresses charge transport between graphene and $PdSe_2$ [19, 20].

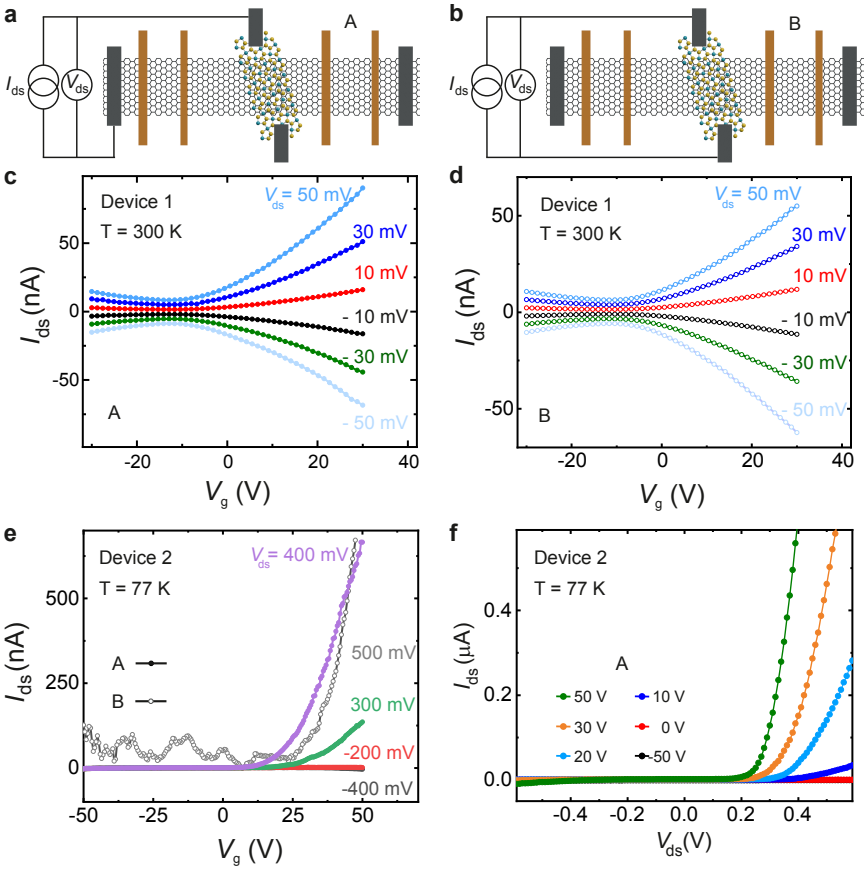


**Fig. 6.4: a,b.** Measurement configuration to investigate charge transport across graphene/$PdSe_2$ interface (**a**) and $PdSe_2$ alone (**b**), respectively. **c,d.** $I_{ds}$ vs $V_g$ measurements of 20-nm thick $PdSe_2$ (Device 1) in the configurations A (**c**) and B (**d**), respectively. **e,f.** $I_{ds}$ vs $V_g$ (**e**) and $I_{ds}$ vs $V_{dv}$ (**f**) measurements of 6-nm thin $PdSe_2$ (Device 2).

## 6.4 Spin transport in Device 1

All measurements of Device 1 were performed at room temperature, following the protocol designed in Chapter 5 . The reference graphene region (the spin channel

between FM1 and FM3) is characterised by measuring Hanle spin precession with $B_z$ (Fig. 6.5a) at different back-gate values. Fitting the data to the solution of Bloch diffusion equation yields spin transport parameters $\tau_s$ and $D_s$. Figures 6.5b,c show their values, extracted for different back-gates. Both $\tau_s$ and $D_s$ increase away from the CNP, a typical signature of FM contacts with pinholes in the $TiO_2$ tunnel barrier [21]. Despite the pinholes, the reference device has a large spin signal. The spin diffusion length is determined to be $\lambda \approx 5$ µm with the exact value depending on the carrier density.

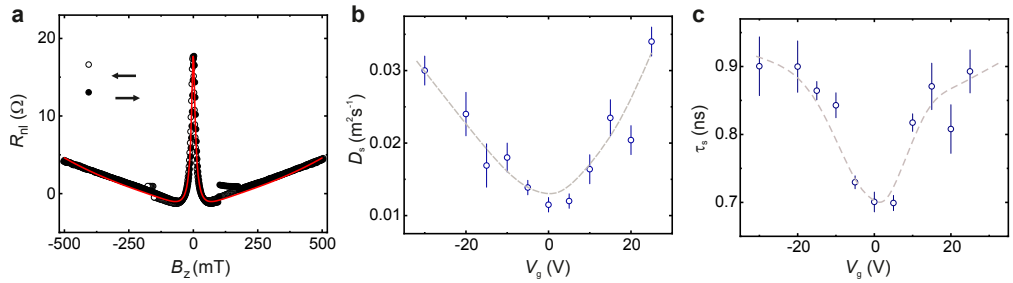


**Fig. 6.5: a.** Hanle spin precession for $B_z$. **b,c.** Spin diffusion constant (**b**) and spin lifetime (**c**) as a function of $V_g$.

After the characterisation of the reference, the spin-lifetime anisotropy in the graphene/$PdSe_2$ region (spin channel between FM1 and FM2) is investigated by sweeping $\vec{B}$ along the $\hat{z}$, $\hat{y}$ and $\hat{x}$ directions while monitoring $R_{nl}$. Figure 6.6 illustrates the dramatic impact of $PdSe_2$ on the graphene spin dynamics for $B_z$ and $B_y$ configurations in Device 1. Figures 6.6a,b show $R_{nl}$ for pristine graphene, obtained using the reference graphene device, while Figs. 6.6c,d present the corresponding measurements in the graphene/$PdSe_2$ device.

The magnetisations $\vec{M}$ of the FM electrodes tend to be aligned along their long axis (i.e. along $\hat{y}$), owing to shape anisotropy. Therefore, $B_z$ causes spins to precess exclusively in the $xy$ plane (see Fig. 6.6e). Because the spin relaxation in graphene on $SiO_2$ is isotropic [15–17], the spin dynamic in the reference does not depend on the spin orientation and the spin precession lineshape is symmetric about $B_z = 0$ (Fig. 6.6a). In stark contrast, the spin precession profile in graphene/$PdSe_2$ is strongly asymmetric (Fig. 6.6c). The values of $R_{nl}$ differ at the two minima located at $B_z \approx \pm 20$ mT by a factor $\sim 3.5$. This result shows that the spin relaxation in the graphene channel underneath $PdSe_2$ differs when spins precess counter-clockwise ($B_z < 0$) or clockwise ($B_z > 0$), suggesting a strong in-plane spin relaxation anisotropy. It also demonstrates that neither $\hat{x}'$ nor $\hat{y}'$ are parallel to $\hat{y}$ (i.e., the orientation of the injected spins). Otherwise, the precession profile would be symmetric about $B_z = 0$, albeit with a different lineshape than in Fig. 6.6a (see Figs. 5.5b,c and Fig. 5.6 in Sec. 5.4 ). Fit of the data obtained for isotropic reference graphene region (Fig. 6.6a) yields $\tau_s = 0.9$ ns. The solutions of the Bloch equations in Figs. 6.6c,d assume $\tau^s_{x'} = 260$ ps, $\tau^s_{y'} = 21$ ps, $\tau^s_{z'} = 18.5$ ps and $\theta = 71°$.

Further evidence of in-plane spin relaxation anisotropy is displayed in Fig. 6.6d. In this configuration, $\vec{B}$ is aligned along $\hat{y}$ (Fig. 6.6f). Therefore, the injected spins are

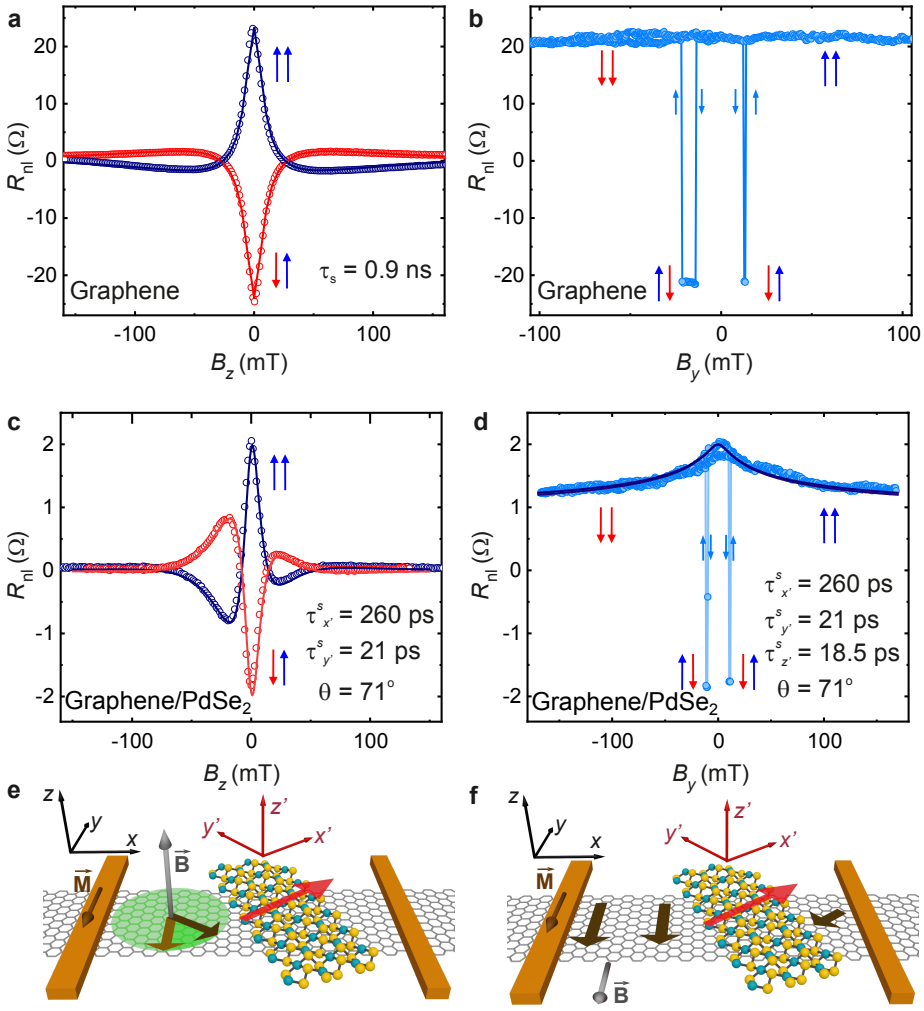


**Fig. 6.6:** $R_{nl}$ as a function of $\vec{B}$ along $\hat{y}$ and $\hat{z}$ in Device 1. **a**,**b.** Measurements of the isotropic reference graphene region. **c**,**d.** Measurements of the anisotropic graphene/$PdSe_2$ region. Open circles represent experimental data and lines are the fits. **a**,**c.** Spin precession measurements as a function of $B_z$, for parallel (blue) and antiparallel (red) FM configurations. **e.** Illustration of the spin precession in the graphene plane $xy$. **b**,**d.** $R_{nl}$ as a function of $B_y$. **f.** Illustration of the spin valve configuration. Injected spins, initially parallel to $\hat{y}$ and $\vec{B}$, rotate towards $\hat{x}'$ when diffusing under $PdSe_2$. Because they misalign from $\vec{B}$, they precess out of plane, making $R_{nl}$ field-dependent and sensitive to $\tau^s_{x'}$, $\tau^s_{y'}$ and $\tau^s_z$ (**e**). In isotropic graphene, $R_{nl}$ is field independent (**b**). Measurements were performed with $V_g = -30$ V.

parallel to $\vec{B}$ and do not precess when diffusing in the isotropic graphene. The $R_{nl}$ is independent of $B_y$, as demonstrated in the reference device (Fig. 6.6b). However, $R_{nl}$ becomes dependent on $B_y$ in graphene/$PdSe_2$ (Fig. 6.6d). To understand this behaviour, we note that the injected spins along $\hat{y}$ are misaligned with $\hat{x}'$ and $\hat{y}'$, as concluded from the analysis of Fig. 6.6c. As explained in Chapter 5, given that by definition $\tau^s_{x'} > \tau^s_{y'}$, spins diffusing in graphene/$PdSe_2$ not only relax but also effectively rotate towards $\hat{x}'$, losing the alignment with $\hat{y}$ even for $B = 0$ (Fig. 6.6f). Therefore, when applying $\vec{B}$ along $\hat{y}$, the spins are no longer parallel to $\vec{B}$ and they start precessing around $\hat{y}$, acquiring an out-of-plane component (see also simulations in Fig. 5.1 and related discussion). Consequently, the signal becomes dependent on

$B_y$ and is influenced not only by $\tau^s_{x'}$ and $\tau^s_{y'}$, but also by $\tau^s_{z'}$.

Spin precession was also investigated with $\vec{B}$ along $\hat{x}$ (Fig. 6.7a,c). For low $B_x$, spins precess out-of-plane but, for sufficiently large $B_x$, the magnetisation of the FMs rotates and ultimately aligns parallel to $\hat{x}$ at the saturation magnetic field $B^{sat}_x$ (see schematics in 6.7e). Since $\vec{B}$ is within the graphene plane, the measurements are largely unaffected by magnetoresistance effects [15, 16]. In isotropic graphene, $R_{nl}(B = 0) \approx R_{nl}(B_x \geq B^{sat}_x)$ (Fig. 6.7a). However, the graphene/$PdSe_2$ region features in-plane anisotropy; thus, $R_{nl}(B = 0)$ and $R_{nl}(B_x > B^{sat}_x)$ will typically differ, as observed in Fig. 6.7c. The precession profile hinges upon the spin lifetimes in all orthogonal directions and, similar to Fig. 6.6d, misalignment between $\hat{x}$ and both $\hat{x}'$ and $\hat{y}'$ leads to a signal dependence on $B_x$, even for $B_x > B^{sat}_x$.

Having established in-plane spin lifetime anisotropy in graphene/$PdSe_2$, the anisotropy can be quantified by estimating $\tau^s_{x',y',z}$. This is achieved by modelling the experimental results using the solution of the Bloch diffusion equations (see Sec. 3.3, Sec.3.4, and Chapter 5).

First, $\theta$ and $\tau^s_{x',y'}$ for graphene/$PdSe_2$ are extracted from the data in Fig. 6.6c using $\tau_s$ and $D_s$ as fixed parameters (extracted beforehand from the reference device). Then, an initial estimate of $\tau^s_z$ is obtained using the results shown in 6.6d, with $\tau^s_{x',y'}$ and $\theta$ taken as fixed parameters. The estimation of $\tau^s_z$ can be improved by forcing the spins to precess out of graphene plane with $\vec{B}$ along $\hat{x}$ (Fig. 6.7c). To fit the results in Fig. 6.7c, the Stoner-Wohlfarth approximation is adopted with in-plane saturation magnetic field $B^{sat}_x = 0.18$ T. The diffusion model precisely accounts for subtle differences in the measurements for $B_x < 0$ and $B_x > 0$, attributed to the rotation of the FMs' magnetisations.

The extraction of $\tau^s_z$ from spin precession measurements with $B_x$ is affected by the substantial non-uniform rotation of the FMs magnetisations even under moderate $B_x$. As explained in Sec. 3.3 and Sec. 5.5, a more reliable approach to determine $\tau^s_z$ requires applying an oblique $\vec{B}$ [15, 16], characterised by an angle $\beta$ measured from the graphene plane (Fig. 6.7f). An oblique magnetic field induces conical spin precession; thus the measurement is sensitive to all spin lifetimes $\tau^s_{x',y',z}$. By varying $\beta$ and the magnitude of $\vec{B}$, the orientation of the spin in the graphene/$PdSe_2$ region relative to the graphene plane changes continuously from 0 to 180°. This allows a systematic scanning of the spin dynamics over all possible spin orientations and derivation of more accurate values of $\tau^s_{x',y',z}$.

Figures 6.7b,d show $R_{nl}$ as a function of a magnetic field $B_\beta$ applied at an angle $\beta$ for reference graphene region and graphene/$PdSe_2$ region, respectively. Fitting the oblique spin precession data in the reference region with an isotropic Bloch diffusion equation provides excellent results (Fig. 6.7b). Oblique data for the graphene/$PdSe_2$ region unequivocally demonstrate that spin lifetimes differ in all three spatial directions. Modelling the precession curves with Bloch diffusion equations, assuming the same values of spin transport parameters as for previous fits ($\tau^s_{x'} = 260$ ps, $\tau^s_{y'} = 21$ ps, $\tau^s_{z'} = 18.5$ ps and $\theta = 71°$), yields excellent results (Fig. 6.7d).

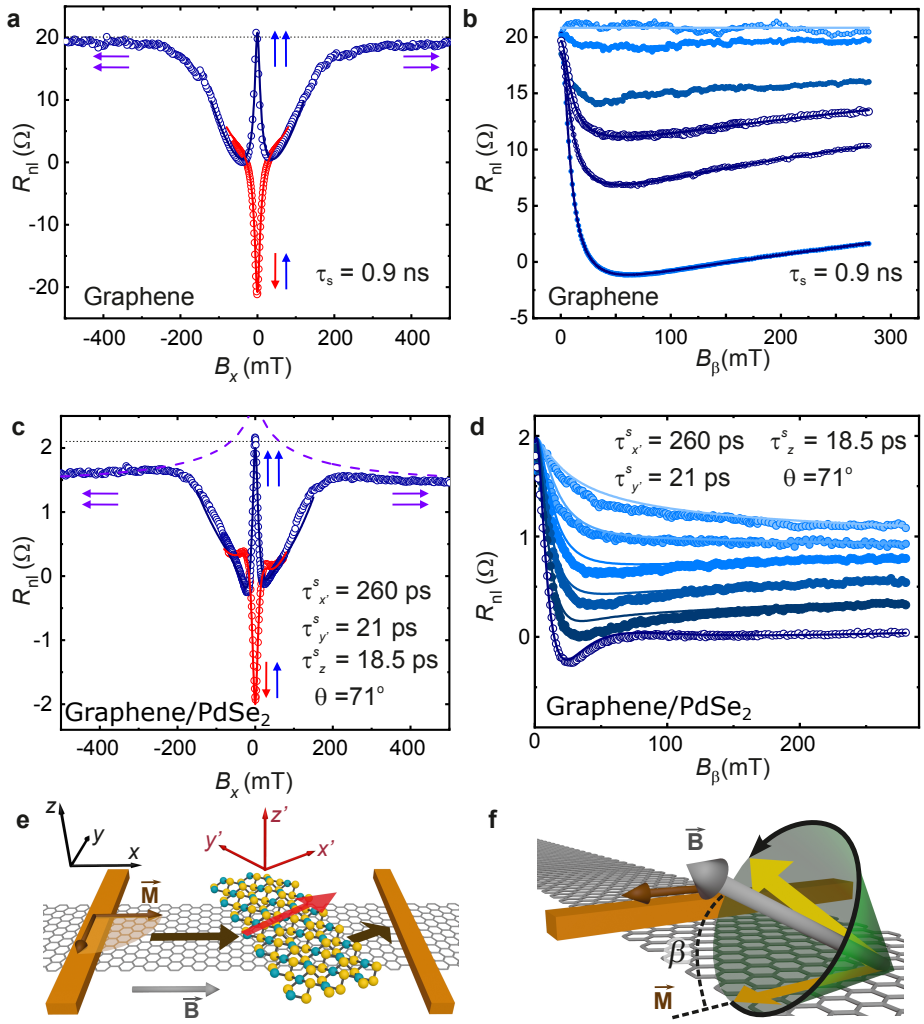


**Fig. 6.7:** $R_{\mathrm{nl}}$ as a function of $\vec{B}$ along $\hat{x}$ and oblique fields applied in the $yz$ plane for Device 1. **a**,**b.** Measurements of the reference graphene region. **c**,**d.** Measurements of the graphene/$PdSe_2$ region. Open circles represent experimental data and lines are the simulations. **a**,**c.** Spin precession measurements as a function of $B_x$, for parallel (blue) and antiparallel (red) FM configurations. In **c**, the dashed line represents the solution for $\vec{M}$ aligned with $\hat{x}$, valid for $B_x > B_x^{\mathrm{sat}}$; solid lines use the Stoner-Wohlfarth approximation with $B_x^{\mathrm{sat}} = 0.18$ T. For low $B_x$, injected spins precess perpendicular to the substrate. **e.** Illustration of the spin precession below $PdSe_2$ due to the in-plane anisotropy. **b**,**d**. $R_{\mathrm{nl}}$ as a function of $B_\beta$ for parallel configuration and $\beta = 3°, 20°, 29°, 41°, 51°$ and $90°$ (top to bottom). All measurements were performed with $V_{\mathrm{g}} = -30$ V.

To further confirm the validity and accuracy of our model, $R_{\mathrm{nl}}$ as a function of $B_\beta$ was measured for two different configurations: using FM1 as injector and FM2 as detector (Fig. 6.8a) and using FM2 as injector and FM1 as detector (Fig. 6.8b). The interchange of the FM1/FM2 roles alters the spin orientation in the graphene/$PdSe_2$ region for the chosen $\beta$ at a given $B$ due to the non-equidistant positioning of $PdSe_2$ relative to FM1 and FM2 (see Sec. 5.4). Both configurations exhibit complete dephasing at $B = B_{\mathrm{dp}} \approx 0.1$ T, however, noticeable differences are observed in the precession profiles. Specifically, using FM1 as the injector (Fig. 6.8a) results in a less prominent $R_{\mathrm{nl}}$ extremum at $B \approx 20$ mT compared to using FM2 as the injector (Fig. 6.8b). The difference is particularly evident at $\beta = 90°$. As $\beta$ is reduced, an anomalous decrease

in $R_{nl}$ is observed, even for $B > B_{dp}$. This behaviour contrasts with that of the pristine graphene, where $R_{nl}$ asymptotically approaches a constant value and then slowly increases due to the out-of-plane tilting of the FM1/FM2 magnetisations at high $B$ [15, 16].

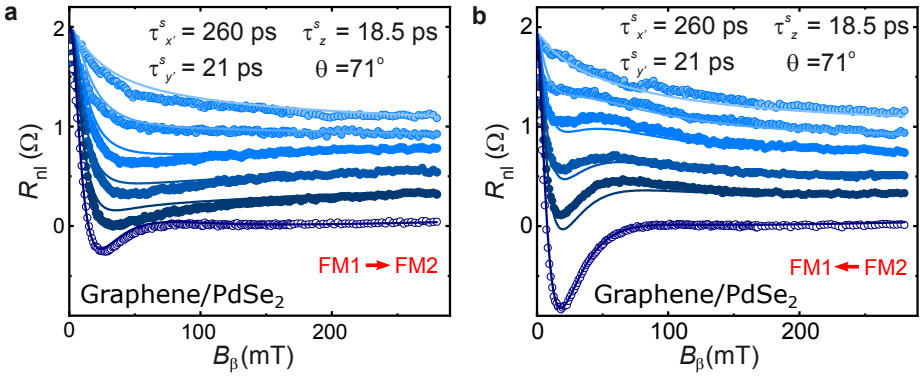


**Fig. 6.8:** Effect of swapping FM injector and detector in Device 1. **a**. Oblique spin precession when using FM1 as an injector and FM2 as a detector. **b.** Oblique spin precession when using FM2 as injector and FM1 as detector. Open circles represent experimental data and lines are the fits. $\beta = 3°, 20°, 29°, 41°, 51°$ and $90°$ (top to bottom). All measurements were performed with $V_g = -30$ V.

The agreement between the model with the experimental results is remarkable, capturing all experimental trends. This is particularly noteworthy considering the breadth of measurements and experimental conditions being examined.

Finally, the spin lifetimes $\tau^s_{x',y',z}$ were investigated as a function of back-gate voltage $V_g$ (Fig. 6.9), which changes the carrier density in the device. Although the spin dynamics remains anisotropic over the measured $V_g$ range, the in-plane anisotropy, defined as $\zeta_{xy} \equiv \tau_{x'}/\tau_{y'}$, decreases from $\zeta_{xy} \approx 12.4$ at $V_g = -30$ V down to $\zeta_{xy} \approx 2.5$ at $V_g = 25$ V. The decrease is driven by the change in $\tau^s_{x'}$, as $\tau^s_{y'}$ and $\tau^s_z$ remain roughly constant with $\zeta_{yz} \equiv \tau^s_{y'}/\tau^s_z \approx 1.1 - 1.3$. Tunable anisotropy has been predicted in conventional 2H-TMDCs/graphene heterostructures [5]. However, systematic experimental investigation of gate control of spin-relaxation anisotropy in these heterostructures have not been performed prior to our results.

Anisotropic behaviour similar to that observed could arise from anisotropic spin absorption in $PdSe_2$. This would require $PdSe_2$ to be conductive and to exhibit spin relaxation lengths that differ depending on the spin orientation. In such a scenario, the observed effective anisotropy would result from variations in spin absorption rather than from differing spin lifetimes within graphene. Although the conductivity of $PdSe_2$ is very low, it is non-zero, and thus this possibility must be considered. However, the presented comprehensive measurements and analysis establish that the anisotropic spin relaxation is an interfacial effect induced by the proximity of $PdSe_2$ to graphene, rather than the result of spin absorption. This conclusion is supported by three key observations:

1. The significant misalignment between the primary spin relaxation axes, $\hat{x}'$ and $\hat{y}'$, and the crystalline axes of $PdSe_2$ ($\theta = 71°$).

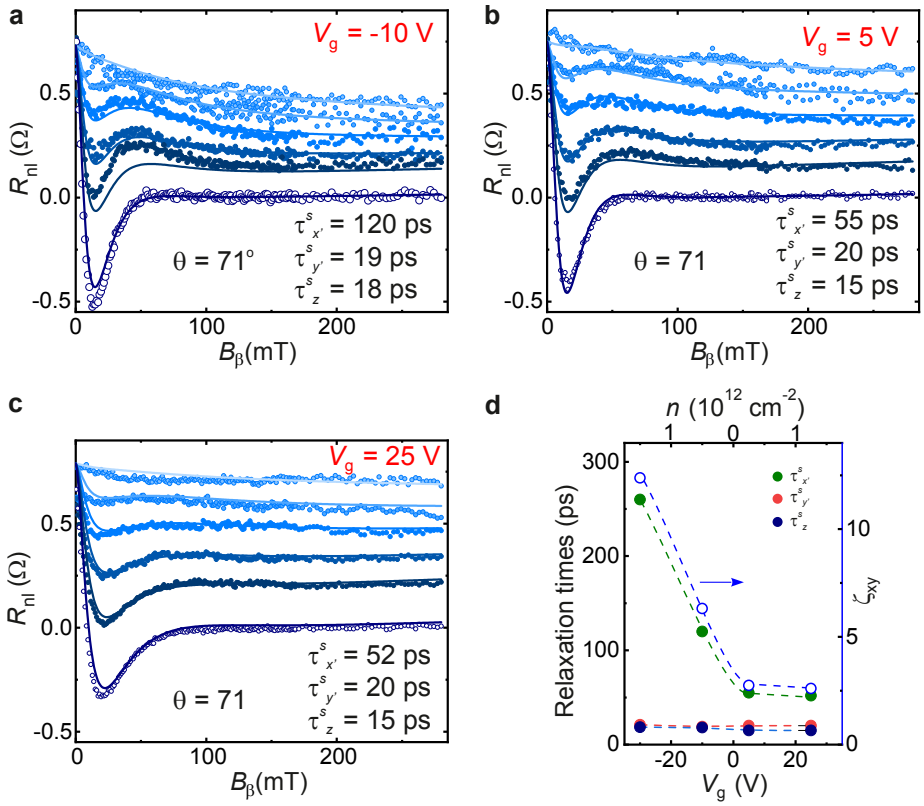


**Fig. 6.9: a,b,c.** Oblique spin precession in graphene/$PdSe_2$ using FM2 as spin injector and FM1 as detector for selected $\beta = 3°, 20°, 29°, 41°, 51°, 90°$ (top to bottom) and $V_g = -10$ V (**a**), $V_g = 5$ V (**b**), and $V_g = 25$ V (**c**), respectively. **d**. $\tau^s_{x'}$, $\tau^s_{y'}$, $\tau^s_z$ and $\zeta_{xy} \equiv \tau^s_{x'}/\tau^s_{y'}$ as a function of $V_g$. $\tau^s_{y'}$, $\tau^s_z$ are largely independent of $V_g$ and around 20 ps, while $\tau^s_{x'}$ decreases from 260 ps at $V_g = -30$ V to 52 ps at $V_g = 25$ V, resulting in $\zeta_{xy}$ decreasing from 12.5 to 2.5. Lines are guides for the eye.

2. The strong agreement between our experimental data and a spin diffusion model that excludes spin absorption.

3. The absence of any correlation between the gate dependence of the spin lifetimes and anisotropy ratios and the gate-dependent transport properties of $PdSe_2$ (compare Figs. 6.4a,b with Fig. 6.9d).

While it is conceivable that spin absorption within $PdSe_2$ could influence spin lifetimes and thus anisotropy ratios, this scenario also appears improbable. There is no discernible correlation between the gate-invariant $\tau^s_{y'}$ and $\tau^s_z$, or the monotonically decreasing $\tau^s_{x'}$ and $\zeta_{xy}$, and the transport characteristics of $PdSe_2$, contrary to what would be expected if spin absorption was a contributing factor.

## 6.5 Spin transport in Device 2

These conclusions are further supported by the spin precession measurements of the graphene/$PdSe_2$ device with thinner $PdSe_2$ at low temperatures (Device 2). In the case of 6-nm thin $PdSe_2$ integrated into Device 2 the band gap is estimated to be larger than 500 meV [13]. To completely suppress the charge transport through $PdSe_2$,

Device 2 was measured at liquid nitrogen temperature. Thus, all the spin transport data presented in this section were gathered at $T = 77$ K.

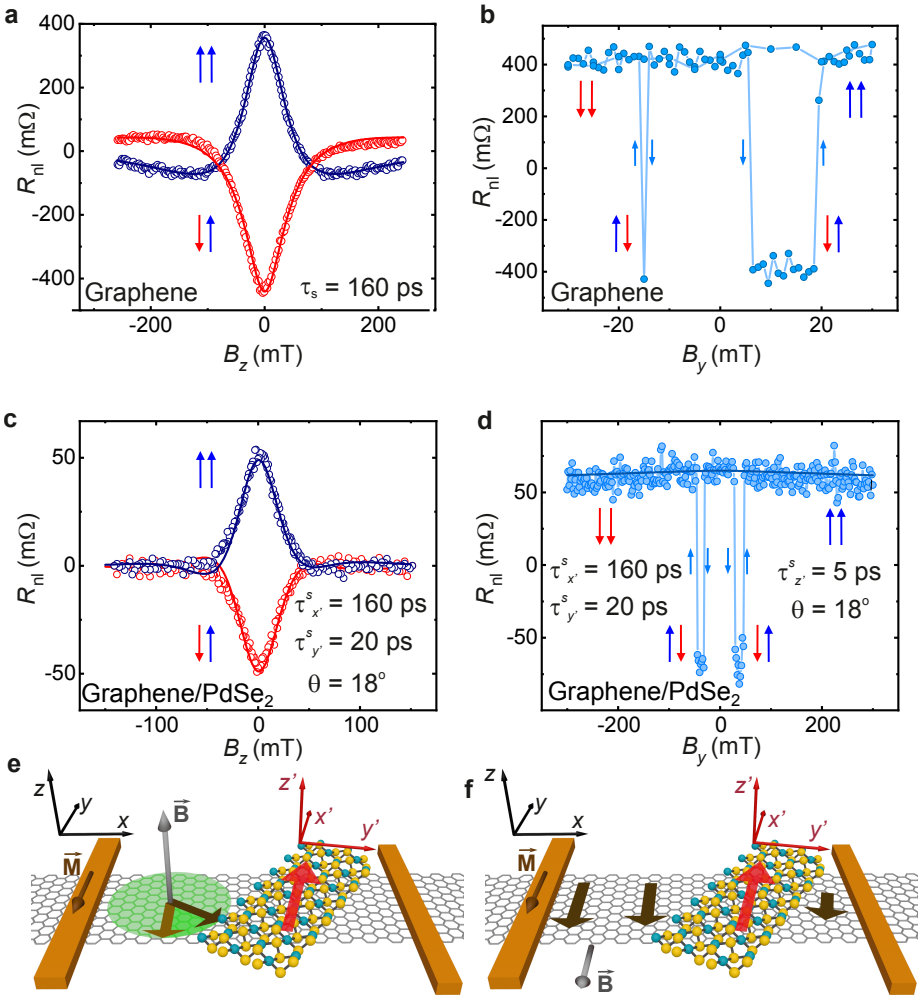


**Fig. 6.10:** $R_{nl}$ as a function of $\vec{B}$ along $\hat{y}$ and $\hat{z}$ in Device 2. **a**,**b.** Measurements of the isotropic reference graphene region. **c**,**d.** Measurements of the anisotropic graphene/$PdSe_2$ region. Open circles represent experimental data and lines are the fits. **a**,**c.** Spin precession measurements as a function of $B_z$, for parallel (blue) and antiparallel (red) FM configurations. **c**,**e.** As $\hat{y}$ is almost collinear with $\hat{x}'$ (illustration **e**), the curve is symmetric about $B_z = 0$. **e.** Illustration of the spin precession in the graphene plane $xy$. **b**,**d.** $R_{nl}$ as a function of $B_y$. **h.** Illustration of the spin valve configuration. Injected spins are already almost colinear with $\hat{x}'$, therefore, they undergo only a slight change of orientation when diffusing below $PdSe_2$ and only a small decrease of $R_{nl}$ is seen when increasing $B_y$.

Figure 6.10 shows $R_{nl}$ for $B_z$ and $B_y$ at $V_g = 50$ V in Device 2. Similar to Device 1, the spin transport in the isotropic reference graphene region is first characterised (Fig. 6.10a). The spin lifetime and diffusion constant are lower in Device 2, possibly due to the contamination of the graphene channel during the device fabrication (see Fig. 6.3e,f).

The spin transport across the graphene/$PdSe_2$ region was investigated with applied $B_z$ (Fig. 6.10c). While the spin precession lineshape appears symmetric, it notably differs from the typical profile observed in pristine graphene (Fig. 6.10a). Specifically, $|R_{nl}|$ in the graphene/$PdSe_2$ region diminishes with increasing $|B_z|$,

reaching zero without a discernible change in sign. This behaviour suggests that $\hat{x}'$ is nearly aligned to $\hat{y}$, i.e., the orientation of the injected spins, as discussed in Sec. 5.4. This observation is reinforced by the weak variation of $R_{\rm nl}$ with $B_y$ (Fig. 6.6d) and is conclusively established by the dramatic suppression of $R_{\rm nl}$ when $B_x$ forces the rotation of the FM magnetisations towards $\hat{x}$ (Fig. 6.11b). Indeed, $R_{\rm nl}(|B_x^{\rm sat}|) = 0$ in the proximitized region, in contrast to $R_{\rm nl}(|B_x^{\rm sat}|) = R_{\rm nl}^0$ in the reference region (Fig. 6.11a). This decrease in $R_{\rm nl}$ is much more pronounced than in Device 1, because once $|B_x| > B_x^{\rm sat}$, the spins are injected close to a short spin lifetime direction ($\hat{y}'$). The effect is also magnified by the larger width of the $PdSe_2$, which covers 2.8 µm of the graphene channel length in Device 2, compared to just 1.4 µm in Device 1. Consequently, the contrast in the exponential decay for spins aligned with $\hat{x}'$ and $\hat{y}'$, characterised by different relaxation lengths, increases. The spin lifetimes and $\theta$ are estimated using oblique spin precession (Fig. 6.11d), yielding $\tau_{x'}^{\rm s} = 160$ ps, $\tau_{y'}^{\rm s} = 20$ ps, $\tau_z^{\rm s} = 5$ ps and $\theta = 18°$. Extracted spin lifetimes and $\zeta_{xy} \approx 8$ are similar to those observed in Device 1.

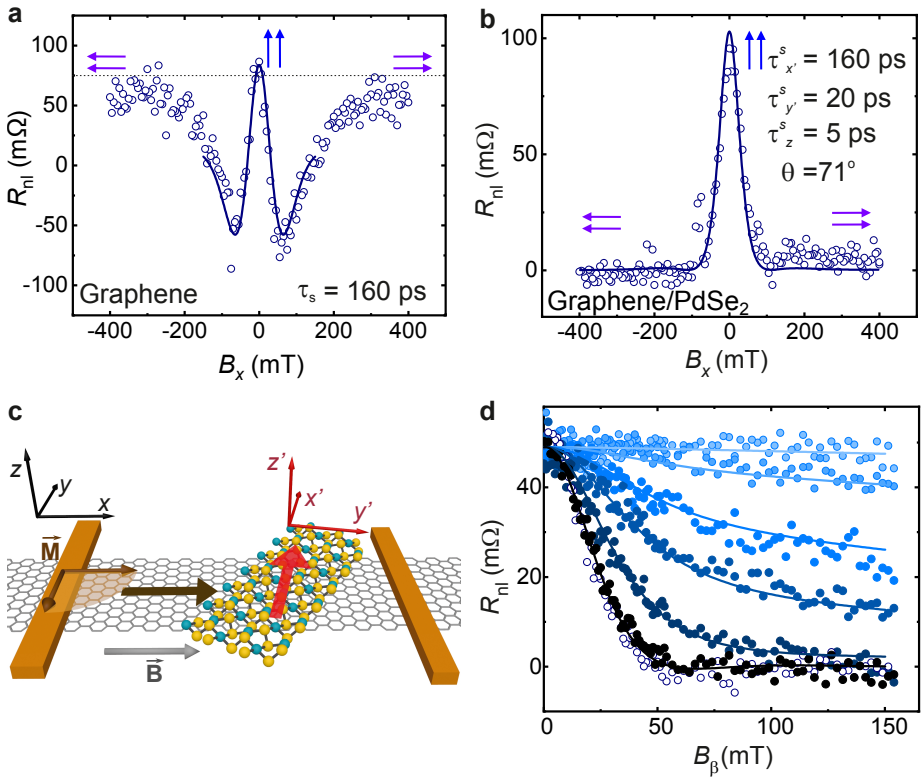


**Fig. 6.11:** $R_{\rm nl}$ as a function of $\vec{B}$ along $\hat{x}$ and oblique fields applied in the $yz$ plane for Device 2. **a**,**b.** Spin precession measurements as a function of $B_x$, for the reference (**a**) and the graphene/$PdSe_2$ (**b**) region. **c.** For $B_x > B_x^{\rm sat}$, spins are injected and detected along $\hat{x}$, which is almost aligned with $\hat{y}'$, leading to the disappearance of $R_{\rm nl}$ (see **b**). **d.** $R_{\rm nl}$ as a function of $B_\beta$ for parallel FM configuration.

## 6.6 Novel SOC in graphene/$PdSe_2$ heterostructure

The results from Device 2 confirm the reproducibility of the findings. The comparable anisotropy between Devices 1 and 2 reinforces that spin absorption is not the source of the observed anisotropy. Moreover, if the observed anisotropy was due to an anisotropic spin absorption, its anisotropy directions would correlate with the $PdSe_2$ crystallographic directions. Therefore, the substantial misalignment between the $PdSe_2$ $a$ axis and $\hat{x}'$ in both devices (71° for Device 1 and 18° for Device 2, see Fig. 6.12) supports the conclusion that the observed anisotropy is due to proximity effects rather than spin absorption. When symmetries are broken, the orientation of the SOFs can vary dramatically with small differences in the structure properties, such as twisting angle [22]. This could explain the differing misalignment between the $PdSe_2$ $a$ axis and $\hat{x}'$ in the two devices.

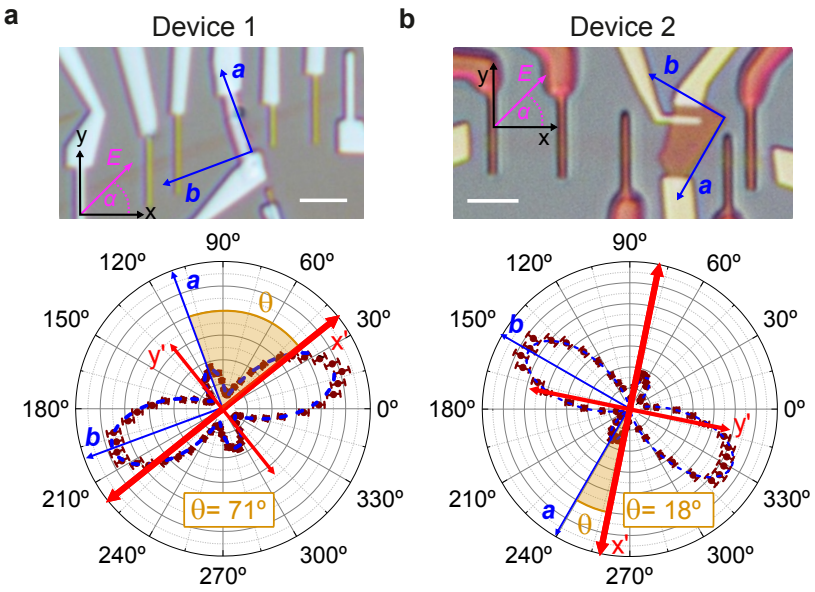


**Fig. 6.12:** Dominant SOF directions in the two devices. **a**,**b.** Top: Optical images of Device 1 (**a**) and Device 2 (**b**). Bottom: Polar plots showing different misalignments between crystallographic directions of $PdSe_2$ and dominant SOF in Device 1 (**a**) and Device 2 (**b**).

The observed spin-lifetime hierarchy $\tau^s_{x'} \gg \tau^s_{y'} \gtrsim \tau^s_z$ suggests the presence of a momentum-independent (persistent) spin texture component along $\tau^s_{x'}$, which dominates the spin relaxation. Persistent spin textures have been predicted in structures with reduced symmetry like monolayers of topological insulators $1T_d$-$MoTe_2$ and $1T_d$-$WTe_2$ [23]. Significant in-plane spin relaxation anisotropy is expected in the conduction band of $1T_d$-$MoTe_2$ monolayers, as the band edge is approached [23], although this has yet to be observed experimentally. A novel SOC term has been anticipated in graphene/SnTe, attributed to the crystal gradient potential in the low-symmetry SnTe [1]. As a result, the in-plane spin texture in the proximitized graphene would be predominantly polarised in a direction closely perpendicular to this gradient. The predicted spin lifetimes in graphene/SnTe reveal a large anisotropy below the valence band maximum, exhibiting a hierarchy akin to that observed in

our experiments. Experimental signatures of anisotropic in-plane spin transport has been reported in ultra-thin black phosphorus at low temperatures (1.5 K), with a small $\zeta_{xy} \approx 1 - 1.8$ and a larger $\zeta_{zy} \approx 6$ [7]. However, the spin lifetime hierarchy $\tau_z^s \gg \tau_{x'}^s \gtrsim \tau_{y'}^s$ differs from that of graphene/$PdSe_2$ and is similar to that of graphene proximitized by 2H-TMDCs. The origin of the anisotropy in black phosphorous remains unknown, as the spin relaxation is expected to be dominated by the Elliot-Yafet mechanism for which $\tau_z^s < \tau_{x',y'}^s$ [24].

Spin dynamics in proximitized graphene is governed by the Dyakonov-Perel mechanism [2, 3, 5]. The spin relaxation rates are described as

$$(\tau_i^s)^{-1} = [\langle\Omega_j^2\rangle_p + \langle\Omega_k^2\rangle_p]\,\tau_p + [\langle\Omega_j^2\rangle_{\rm iv} + \langle\Omega_k^2\rangle_{\rm iv}]\,\tau_{\rm iv} \tag{6.1}$$

with $\{i,j,k\} \subseteq \{x',y',z\}$, where $\tau_p$ and $\tau_{\rm iv}$ represent respectively the momentum and intervalley scattering times and $\langle\Omega_i^2\rangle_{p,{\rm iv}}$ are the average momentum-dependent (index $p$) and momentum-independent (index iv) effective SOF components. In graphene/2H-TMDC heterostructures preserving the $\mathcal{C}_{3v}$ symmetry, $\langle\Omega_i^2\rangle_p$ are determined by the conventional Rashba SOC and the pseudospin inversion asymmetry SOC terms with $\langle\Omega_z^2\rangle_p = 0$, while $\langle\Omega_i^2\rangle_{\rm iv}$ is given by the valley-Zeeman SOC with $\langle\Omega_{x'}^2\rangle_{\rm iv} = \langle\Omega_{y'}^2\rangle_{\rm iv} = 0$ [5]. Accordingly, the out-of-plane spins follow the usual Rashba-SOC relaxation, while the in-plane spins are affected by both the Rashba SOC and valley-Zeeman SOC. The resulting spin lifetime anisotropy is

$$\zeta_{zx(y)} \equiv \frac{\tau_z^s}{\tau_{x(y)}^s} = \left(\frac{\lambda_{\rm VZ}}{\lambda_{\rm R}}\right)^2 \left(\frac{\tau_{\rm iv}}{\tau_p}\right) + \frac{1}{2}\,, \tag{6.2}$$

where $\lambda_{\rm R}$ and $\lambda_{\rm VZ}$ are the Rashba (R) and valley-Zeeman (VZ) SOC strengths, $\tau_{\rm iv}$ the intervalley scattering time and $\tau_p$ the momentum relaxation time [5]. Because typically $\tau_{\rm iv}/\tau_p \gg 1$, and $\lambda_{\rm R}$ and $\lambda_{\rm VZ}$ are of similar magnitude, then $\zeta_{zx(y)} \gg 1$. In graphene/$PdSe_2$, the momentum-independent SOF is along $\hat{x}'$, thus $\langle\Omega_{y'}^2\rangle_{\rm iv} = \langle\Omega_{z'}^2\rangle_{\rm iv} = 0$. Therefore, the spin relaxation along $\hat{x}'$ is dominated by the Rashba SOC, while the spin relaxation along $\hat{y}'$ and $\hat{z}$ include contributions from both the Rashba SOC and the persistent SOF. In this case, we obtain

$$\zeta_{xy} = 2\left(\frac{\lambda_{\rm pers}}{\lambda_{\rm R}}\right)^2 \left(\frac{\tau_{\rm iv}}{\tau_p}\right) + 1 \tag{6.3}$$

and $\zeta_{zy} \equiv \tau_z^s/\tau_y^s \lesssim 1$.

To estimate $\lambda_{\rm R}$ and $\lambda_{\rm pers}$, it is necessary to know the characteristic timescales $\tau_p$ and $\tau_{\rm iv}$. The intervalley scattering time in graphene has been determined through spin relaxation anisotropy experiments [2, 3] and weak localization measurements [25–27]. Regardless of the substrate or fabrication process, the reported $\tau_{\rm iv}$ consistently cluster within the 5-20 ps range. Assuming $\tau_{\rm iv} \approx 10$ ps and taking $\tau_p \approx 0.4$ ps, as estimated from the conductivity of Device 1, our experimental $\zeta_{xy} \approx 12.5$ in graphene/$PdSe_2$ corresponds to $\lambda_{\rm pers}/\lambda_{\rm R} \approx 0.5$. The experimental estimation of $\lambda_{\rm R}$ for graphene

proximitized with 2H-TMDCs falls within the range of 5 and 30 meV [26, 28–30]. Taking a conservative value of $\lambda_R = 5$ meV for graphene/$PdSe_2$, we obtain $\lambda_{pers} \approx 2.5$ meV.

The origin of $\theta$ remains an open question and requires density functional theory calculations as a function of twist angle in the graphene/$PdSe_2$ heterostructure, similar to those performed for graphene/SnTe [1]. However, predicting $\theta$ can be challenging; for instance, in the simpler case of proximity Rashba SOC in graphene coupled with high-symmetry 2H-TMDCs, the spin texture rotation angle away from tangential was found to be highly sensitive to the heterostructure's properties, with no discernible trend as a function of twist angle [22].

The reported spin-lifetime anisotropy in graphene/$PdSe_2$ underscores the versatility of proximity effects in van der Waals heterostructures. Our findings offer valuable insights into innovative strategies for tailoring spin textures through the combination of materials with distinct crystal symmetries. The observation of persistent spin textures in graphene/$PdSe_2$, akin to those predicted in monolayer $1T_d$-$MoTe_2$ and $1T_d$-$WTe_2$, introduces promising avenues for advancing spin manipulation techniques and exploring topologically non-trivial states. The ability to tune the spin relaxation anisotropy opens new opportunities for developing directionally tunable spin transport.

## References

[1] M. Milivojevic et al.; "Giant asymmetric proximity-induced spin–orbit coupling in twisted graphene/SnTe heterostructure". *2D Materials* 2024**, 11**, p. 035036. DOI: 10.1088/2053-1583/ad59b4.

[2] T. S. Ghiasi et al.; "Large Proximity-Induced Spin Lifetime Anisotropy in Transition-Metal Dichalcogenide/Graphene Heterostructures". *Nano Letters* 2017**, 17**, pp. 7528–7532. DOI: 10.1021/acs.nanolett.7b03460.

[3] L. A. Benítez et al.; "Strongly anisotropic spin relaxation in graphene–transition metal dichalcogenide heterostructures at room temperature". *Nature Physics* 2018**, 14**, pp. 303–308. DOI: 10.1038/s41567-017-0019-2.

[4] F. Herling et al.; "Gate tunability of highly efficient spin-to-charge conversion by spin Hall effect in graphene proximitized with $WSe_2$". *APL Materials* 2020**, 8**, p. 071103. DOI: 10.1063/5.0006101.

[5] A. W. Cummings et al.; "Giant Spin Lifetime Anisotropy in Graphene Induced by Proximity Effects". *Physical Review Letters* 2017**, 119**, p. 206601. DOI: 10.1103/PhysRevLett.119.206601.

[6] M. Offidani and A. Ferreira; "Microscopic theory of spin relaxation anisotropy in graphene with proximity-induced spin-orbit coupling". *Physical Review B* 2018**, 98**, p. 245408. DOI: 10.1103/PhysRevB.98.245408.

[7] L. Cording et al.; "Highly anisotropic spin transport in ultrathin black phosphorus". *Nature Materials* 2024**, 23**, pp. 479–485. DOI: 10.1038/s41563-023-01779-8.

[8] C. K. Safeer et al.; "Large Multidirectional Spin-to-Charge Conversion in Low-Symmetry Semimetal $MoTe_2$ at Room Temperature". *Nano Letters* 2019**, 19**, pp. 8758–8766. DOI: 10.1021/acs.nanolett.9b03485.

[9] A. M. Hoque et al.; "All-electrical creation and control of spin-galvanic signal in graphene and molybdenum ditelluride heterostructures at room temperature". *Communications Physics* 2021**, 4**, pp. 1–9. DOI: 10.1038/s42005-021-00611-6.

[10] B. Zhao et al.; "Unconventional Charge–Spin Conversion in Weyl-Semimetal $WTe_2$". *Advanced Materials* 2020**, 32**, p. 2000818. DOI: 10.1002/adma.202000818.

[11] L. Camosi et al.; "Resolving spin currents and spin densities generated by charge-spin interconversion in systems with reduced crystal symmetry". *2D Materials* 2022**, 9**, p. 035014. DOI: 10.1088/2053-1583/ac6fec.

[12] J. Sun et al.; "Electronic, transport, and optical properties of bulk and monolayer $PdSe_2$". *Applied Physics Letters* 2015**, 107**, p. 153902. DOI: 10.1063/1.4933302.

[13] A. D. Oyedele et al.; "$PdSe_2$: Pentagonal Two-Dimensional Layers with High Air Stability for Electronics". *Journal of the American Chemical Society* 2017**, 139**, pp. 14090–14097. DOI: 10.1021/jacs.7b04865.

[14] A. David et al.; "Induced spin-orbit coupling in twisted graphene–transition metal dichalcogenide heterobilayers: Twistronics meets spintronics". *Physical Review B* 2019**, 100**, p. 085412. DOI: 10.1103/PhysRevB.100.085412.

[15] B. Raes et al.; "Determination of the spin-lifetime anisotropy in graphene using oblique spin precession". *Nature Communications* 2016**, 7**, p. 11444. DOI: 10.1038/ncomms11444.

[16] B. Raes et al.; "Spin precession in anisotropic media". *Physical Review B* 2017**, 95**, p. 085403. DOI: 10.1103/PhysRevB.95.085403.

[17] L. A. Benítez et al.; "Investigating the spin-orbit interaction in van der Waals heterostructures by means of the spin relaxation anisotropy". *APL Materials* 2019**, 7**, p. 120701. DOI: 10.1063/1.5124894.

[18] J. Yu et al.; "Direct Observation of the Linear Dichroism Transition in Two-Dimensional Palladium Diselenide". *Nano Letters* 2020**, 20**, pp. 1172–1182. DOI: 10.1021/acs.nanolett.9b04598.

[19] W. Yan et al.; "A two-dimensional spin field-effect switch". *Nature Communications* 2016**, 7**, p. 13372. DOI: 10.1038/ncomms13372.

[20] A. Dankert and S. P. Dash; "Electrical gate control of spin current in van der Waals heterostructures at room temperature". *Nature Communications* 2017**, 8**, p. 16093. DOI: 10.1038/ncomms16093.

[21] W. Han et al.; "Tunneling Spin Injection into Single Layer Graphene". *Physical Review Letters* 2010**, 105**, p. 167202. DOI: 10.1103/PhysRevLett.105.167202.

[22] T. Naimer et al.; "Twist-angle dependent proximity induced spin-orbit coupling in graphene/transition metal dichalcogenide heterostructures". *Physical Review B* 2021**, 104**, p. 195156. DOI: 10.1103/PhysRevB.104.195156.

[23] M. Vila et al.; "Low-symmetry topological materials for large charge-to-spin interconversion: The case of transition metal dichalcogenide monolayers". *Physical Review Research* 2021**, 3**, p. 043230. DOI: 10.1103/PhysRevResearch.3.043230.

[24] M. Kurpas, M. Gmitra, and J. Fabian; "Spin properties of black phosphorus and phosphorene, and their prospects for spincalorics". *Journal of Physics D: Applied Physics* 2018**, 51**, p. 174001. DOI: 10.1088/1361-6463/aab5a2.

[25] Z. Wang et al.; "Strong interface-induced spin–orbit interaction in graphene on $WS_2$". *Nature Communications* 2015**, 6**, p. 8339. DOI: 10.1038/ncomms9339.

[26] Z. Wang et al.; "Origin and Magnitude of 'Designer' Spin-Orbit Interaction in Graphene on Semiconducting Transition Metal Dichalcogenides". *Physical Review X* 2016**, 6**, p. 041020. DOI: 10.1103/PhysRevX.6.041020.

[27] T. Wakamura et al.; "Strong Anisotropic Spin-Orbit Interaction Induced in Graphene by Monolayer $WS_2$". *Physical Review Letters* 2018**, 120**, p. 106802. DOI: 10.1103/PhysRevLett.120.106802.

[28] L. A. Benítez et al.; "Tunable room-temperature spin galvanic and spin Hall effects in van der Waals heterostructures". *Nature Materials* 2020**, 19**, pp. 170–175. DOI: 10.1038/s41563-019-0575-1.

[29] C. Monaco, A. Ferreira, and R. Raimondi; "Spin Hall and inverse spin galvanic effects in graphene with strong interfacial spin-orbit coupling: A quasiclassical Green's function approach". *Physical Review Research* 2021**, 3**, p. 033137. DOI: 10.1103/PhysRevResearch.3.033137.

[30] D. Wang et al.; "Quantum Hall Effect Measurement of Spin–Orbit Coupling Strengths in Ultraclean Bilayer Graphene/$WSe_2$ Heterostructures". *Nano Letters* 2019**, 19**, pp. 7028–7034. DOI: 10.1021/acs.nanolett.9b02445.

# Chapter 7

# Charge–spin interconversion in graphene/$WTe_2$ heterostructures

The ability to generate spins in arbitrary directions, ideally by electrical means, is a long-sought goal in spintronics. Charge–spin interconversion (CSI) phenomena offer FM-free electrical injection and detection of spins. The direction of the spin currents and the spin polarisation generated by CSI strongly depend on the crystal symmetries. The requirement for mutual perpendicularity between charge current, spin current, and spin polarisation is lifted in low-symmetry systems, allowing for CSI with unconventional components. This chapter presents a measurement protocol for the disentanglement of spin currents and spin densities in low-symmetry systems and provides an experimental demonstration of unconventional CSI in graphene/$WTe_2$ heterostructure. The chapter is based on the work published in *2D Materials* **9**, 035014 (2022). [1].

## 7.1 Introduction

Spin–orbit coupling (SOC) strongly modifies the electronic states in crystals lacking inversion symmetry [2]. Such modifications result in spin-polarised bands and intriguing topological phases [3–6], which allow charge-spin interconversion (CSI) [7–9]. The spin Hall effect (SHE) [8, 10–12], inverse spin galvanic effect (ISGE) [13], and the corresponding reciprocal effects (related to the former by Onsager reciprocal relations [14, 15]) are fundamental CSI phenomena that have been widely studied to achieve FM-free spin injection and detection [7–9] (see Sec. 2.5 for an introduction of CSI phenomena).

Experimental observations of the SHE and ISGE were originally obtained in semiconductors [13, 16, 17] and metals [18–20]. Although it was known that, given their SOC-related origin, the SHE and ISGE are often concomitant, those early works usually focused only on one of the two and its reciprocal effect. Understanding the relation between the SHE and ISGE has become essential in light of their potential technological relevance, particularly for magnetic recording [8, 21]. Research on SHE and ISGE has been further stimulated by recent results demonstrating relatively high

CSI efficiency in vdW heterostructures comprising graphene and high SOC materials [22–24].

In some cases, it is possible to discriminate between SHE and ISGE, for instance, when graphene is modified by the proximity of a semiconducting TMDC in high-symmetry heterostructures. In these systems, SHE is driven by the valley-Zeeman SOC and ISGE by the Rashba SOC, leading to spin populations that are orthogonal to each other [25, 26] and, therefore, can be easily disentangled [22, 24, 27]. However, if the TMDC conducts charge, the separation of CSI contributions from the TMDC bulk, the graphene/TMDC interface, and proximitized graphene becomes more challenging [23]. Moreover, CSI with unconventional spin orientations is expected in the low-symmetry TMDCs (e.g., $MoTe_2$ or $WTe_2$) and twisted graphene/TMDC heterostructures, further complicating the analysis.

$WTe_2$ has been used as a spin current source in spin-orbit torque (SOT) experiments to demonstrate the possibility of injecting spins with new polarisation components unavailable in high-symmetry materials [28]. Graphene/$MoTe_2$ and graphene/$WTe_2$ nonlocal spin valve studies have found an unexpected spin-polarisation component along the direction of charge current [29, 30]. This component is prohibited by bulk symmetries and was attributed to broken symmetries due to uncontrolled strain during device fabrication. However, these measurements were performed without characterising the strain and direct knowledge of the crystal orientation. It has been only argued that the crystals generally cleave in a preferential direction [29].

Furthermore, a recent study suggests that a widespread method used to identify the ISGE (SGE) by rotating the FM detector's (injector's) magnetisation is unreliable due to significant charge current contribution to the signal [31]. The Hall effect in graphene induced by stray fields was identified as a probable source of this artefact.

These observations demonstrate the need for careful nonlocal measurement protocols that would allow the identification and quantification of competing CSI effects. Additionally, CSI experiments that identify the crystallographic directions of $WTe_2$ and the strain at the interface are required. This chapter first discusses CSI effects in $WTe_2$ in the context of crystal symmetries. Polarised Raman spectroscopy is used to determine the $WTe_2$ crystal orientation and characterise the strain. Subsequently, a measurement protocol that can be used to resolve the contributions of SHE and ISGE is presented. Measurements of the graphene/$WTe_2$ device are then shown and analysed. Finally, the possible origins of the observed CSI components are discussed.

## 7.2 Symmetry considerations for CSI in $T_d$-$WTe_2$

$WTe_2$ is a vdW TMDC that is stable in several different phases. The orthorhombic $T_d$ phase ($Pmn2_1$) is characterised by a lack of bulk inversion symmetry. Compared to the monoclinic (centrosymmetric) T′ phase, the $T_d$ phase has only a mirror plane $\mathcal{M}_a$ and glide mirror plane $\widetilde{\mathcal{M}_b}$ perpendicular to the $\hat{a}$ and $\hat{b}$ crystallographic direction, respectively (Fig. 7.1). An out-of-plane two-fold screw rotational symmetry $\mathcal{C}_{2a}$

present in T′ $WTe_2$ is slightly broken [32]. Multilayer $T_d$-$WTe_2$ is a type II Weyl semimetal [33, 34], while in monolayer form it is a 2D topological insulator [35–37].

The SHE is described by linear response theory [38] as

$$J^k_{s,i} = \sigma^k_{ij} E_j \Rightarrow \vec{J}^k_s = \overline{\sigma^k}\, \vec{E}\,, \tag{7.1}$$

where $E_j$ is the external electric field in the $\hat{j}$ direction that generates the spin current $J^k_{s,i}$ in the $\hat{i}$ direction with spin polarisation $\vec{S}$ in the $\hat{k}$ direction. $\overline{\sigma^k}$ is the spin Hall conductivity tensor whose terms depend on the composition of the crystal and its symmetries. In a high-symmetry crystal, only off-diagonal $\sigma^k_{ij}$ terms with $i \neq j \neq k$ are nonzero, resulting in conventional SHE ($\vec{J}_c \perp \vec{J}_s \perp \vec{S}$). Reduced symmetries allow additional $\sigma^k_{ij}$ terms that can break the mutual perpendicular relationship between $\vec{J}_c$, $\vec{J}_s$ and $\vec{S}$ [39].

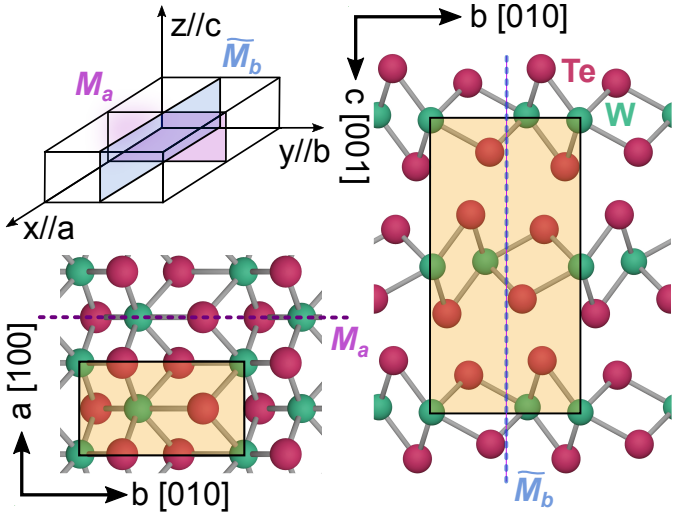


**Fig. 7.1:** Crystal structure of $T_d$-$WTe_2$. It has two mirror symmetries $\mathcal{M}_a$ and $\widetilde{\mathcal{M}}_b$ that allow only conventional CSI components.

In the case of bulk $T_d$-$WTe_2$, mirror planes $\mathcal{M}_a$ and $\widetilde{\mathcal{M}}_b$ (Fig. 7.1) allow only conventional SHE. Nevertheless, there are 6 independent conventional configurations due to the crystal's low symmetry (Laue group mmm and space group 31) [38]

$$\overline{\sigma^x} = \begin{pmatrix} 0 & 0 & 0 \\ 0 & 0 & \sigma^x_{yz} \\ 0 & \sigma^x_{zy} & 0 \end{pmatrix} \quad \overline{\sigma^y} = \begin{pmatrix} 0 & 0 & \sigma^y_{xz} \\ 0 & 0 & 0 \\ \sigma^y_{zx} & 0 & 0 \end{pmatrix} \quad \overline{\sigma^z} = \begin{pmatrix} 0 & \sigma^z_{xy} & 0 \\ \sigma^z_{yx} & 0 & 0 \\ 0 & 0 & 0 \end{pmatrix} \tag{7.2}$$

and the SHE is anisotropic, i.e. the magnitude of induced $\vec{J}^k_s$ depends on the direction of the charge current. This property could be used, for instance, to modulate the strength of SOTs in spintronic devices.

At the graphene/$PdSe_2$ interface, $\widetilde{\mathcal{M}}_b$ is broken. Only $\mathcal{M}_a$ possibly remains if the two 2DMs are aligned, i.e. there is no twist between them (Fig. 7.2a). In this case, an electric field $E_x$ perpendicular to $\mathcal{M}_a$ induces a transverse $\vec{J}_s$ with $\vec{S}$ that can be anywhere in this plane, possibly colinear with $\vec{J}_s$ (Fig. 7.2b). However, $\mathcal{M}_a$

still forbids transverse $\vec{J}_s$ with $\vec{S}$ along $\vec{J}_c$. This restriction disappears if the mirror symmetry $\mathcal{M}_a$ is broken at the twisted graphene/$WTe_2$ interface and $\vec{S}$ is allowed in any direction.

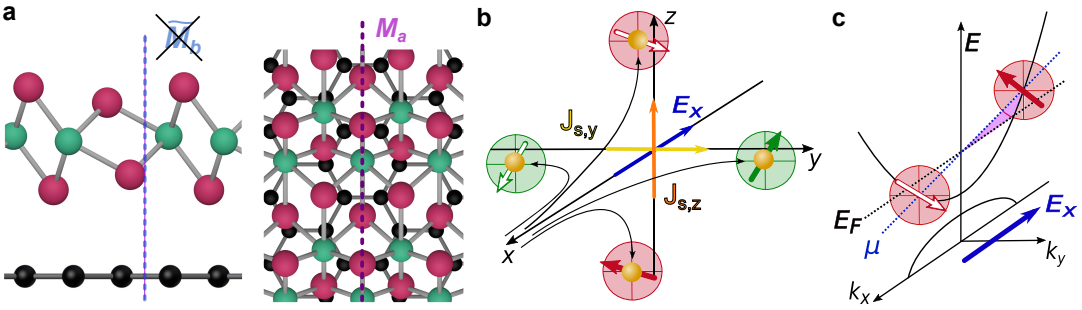


**Fig. 7.2: a.** Aligned graphene/ $T_d$-$WTe_2$ interface (i.e. without twist), where $\widetilde{\mathcal{M}}_b$ is broken and only $\mathcal{M}_a$ is preserved. **b,c.** SHE and ISGE occurring at the aligned graphene/$T_d$-$WTe_2$ interface. $E_x$ induces spin Hall current along $\hat{z}$ ($J^{yz}_{s,z}$) and $\hat{y}$ ($J^{yz}_{s,y}$) with spin polarisation $\vec{S}$ within the $xy$ plane (**b**) and an out-of-equilibrium distribution of spin population (**c**). The circles in **b** and **c** show the planes where $\vec{S}$ (represented by the arrows) is allowed by symmetry.

The ISGE depends directly on the electronic band structure polarisation and is governed by the same symmetry considerations [40, 41]. In a high-symmetry crystal, a spin polarisation can only arise when the inversion symmetry is broken at a boundary or an interface, leading to the Rashba effect [42, 43]. At the interface of the aligned graphene/$T_d$-$WTe_2$ heterostructure, the spin polarisation must be contained in the plane $\mathcal{M}_a$ (Fig. 7.2c). Again, this constraint is removed at the interface of twisted graphene/$T_d$-$WTe_2$ heterostructure.

The CSI effects can be resolved with nonlocal measurements of lateral spin valve devices. The next section presents the device geometry and the measurement protocol that allows the disentanglement of spin currents and spin densities generated by SHE and ISGE in $WTe_2$/graphene heterostructures.

## 7.3 Device geometry and measurement protocol for CSI disentanglement

Nonlocal spin-dependent measurements have been widely used to investigate CSI phenomena [18] and extract the polarisation of the generated spins. In these measurements, a charge current $I$ is applied along the CSI region generating a spin-polarised population through SHE and ISGE. The spin-polarised population diffuses from the CSI region and induces a nonlocal voltage $V_{nl}$ between FM and a reference NM contact. The polarisation of the CSI-generated spins can be extracted by studying the $V_{nl}$ as a function of a magnetic field $\vec{B}$ of different magnitudes and orientations [44, 45].

When the spins originating from the SHE and the ISGE are mutually perpendicular, they can be fully resolved by investigating spin precession with in-plane and out-of-plane magnetic fields [24] or by a symmetry analysis in oblique magnetic fields

[22, 27]. These approaches are insufficient in graphene/$WTe_2$ and graphene/$MoTe_2$ heterostructures because the low-symmetry TMDC is conducting [29, 30, 46]. However, the ISGE induces a local spin density that homogeneously diffuses to both sides of the sample, whereas the SHE generates a directed spin current. Thus, it is possible to discern between the SHE and ISGE-generated spins by comparing spin accumulations along the spin current direction at opposite sides of the CSI region, as illustrated in Fig. 7.3.

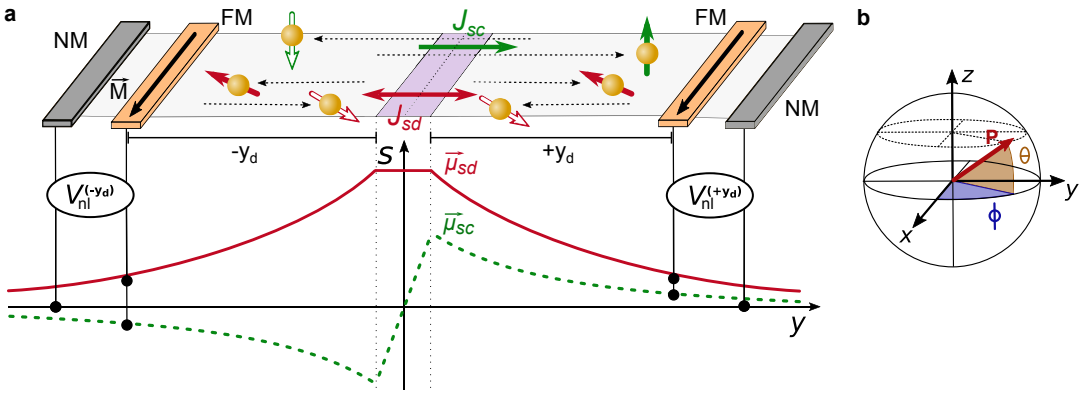


**Fig. 7.3: a.** Sketch of the device geometry and generated spin Hall current ($J_{sc}$) and spin density ($J_{sd}$) (top) and spin electrochemical potentials $\vec{\mu}_{sc}$ and $\vec{\mu}_{sd}$ (bottom). The spins generated in the CSI region (depicted by violet stripe) diffuse in the spin channel towards $\pm\hat{y}$ and are detected by the FM electrodes. $J_{sc}$ originates from the spin Hall current along $\hat{y}$ ($J_{s,y}$). The spin density originates from the uniform spin accumulation in the CSI region due to $J_{s,z}$ and ISGE. **b.** Illustration of the CSI spin polarisation orientation characterised by angles $\phi$ and $\theta$.

When the current $I$ is applied along $\hat{x}$ in the CSI region, the SHE generates spin currents along $\hat{y}$ ($J_{s,y}$) and $\hat{z}$ ($J_{s,z}$) (Fig. 7.2b), which coexist with the spin density induced by the ISGE (Fig. 7.2c). Diffusing spins induce nonlocal voltages $V_{nl}^{(\pm y_d)}$. A direct comparison between the $V_{nl}^{(\pm y_d)}$ measured by the two equally spaced detectors at a distance $\pm y_d$ away from the CSI region differentiates the spins generated by the spin current $J_{s,y}$ from those generated by the ISGE and $J_{s,z}$. Indeed, the spin current component $J_{sc}$ diffusing away from the CSI region, which originates from $J_{s,y}$, generates opposite spin accumulation at $\pm y_d$. In contrast, the spin current $J_{sd}$, associated with ISGE and $J_{s,z}$, generates the same spin accumulation at $\pm y$. Therefore,

$$(V_{nl}^{(+y)} + V_{nl}^{(-y)})/2 \propto J_{sd}\,, \tag{7.3}$$

whereas

$$(V_{nl}^{(+y)} - V_{nl}^{(-y)})/2 \propto J_{sc}\,. \tag{7.4}$$

These measurements do not distinguish between ISGE and $J_{s,z}$, since both induce a spin density whose orientation does not vary in the CSI region [23]. However, these components can be disentangled by analysing $(V_{nl}^{(+y)} + V_{nl}^{(-y)})/2$ as a function of the thickness of the SOC material [8]. In particular, when the thickness is much smaller than the spin relaxation length along $\hat{z}$, $J_{s,z}$ vanishes [47, 48], and only ISGE contributes to the nonlocal signal.

Considering the previous discussion, we focus on characterising the spins generated by $J_{sc}$ and $J_{sd}$ employing spin detectors placed at $\pm y_d$ to measure spin precession signals. The steady-state spin diffusion and precession in the narrow spin channel are governed by the 1D Bloch diffusion equation (see Eq. 5.1), which we reproduce here [49, 50]

$$D_s \frac{\partial^2 \vec{\mu}_s}{\partial y^2} + \gamma_c \, \vec{\mu}_s \times \vec{B} - \vec{\mu}_s \cdot \overline{\tau_s}^{-1} = 0 \,, \tag{7.5}$$

where $\vec{\mu}_s = (\mu_x \,,\ \mu_y \,,\ \mu_z)$ and $\mu_i$ is the spin electrochemical potential for spins along $\hat{i}$, $\gamma_c$ is the electron gyromagnetic ratio, $D_s$ is the diffusion constant and $\overline{\tau_s}^{-1}$ characterises the spin lifetimes $\tau_i^s$. In the case of graphene $\tau_x^s = \tau_y^s = \tau_z^s = \tau_s$ and spin relaxation is isotropic [51]. The graphene/$WTe_2$ bilayer serves as a spin injector. The CSI spin injection efficiency $\vec{P}^{\pm}$ is characterised by effective spin polarisation factors

$$\vec{P}^{\pm} = (P_x^{\pm} \,,\ P_y^{\pm} \,,\ P_z^{\pm}) = (J_x^{\pm}/I \,,\ J_y^{\pm}/I \,,\ J_z^{\pm}/I)\, w \,, \tag{7.6}$$

where $\pm$ stands for the injection at opposing sides of the CSI region, $J_i$ is the corresponding spin current with contributions from $J_{sc}$ and $J_{sd}$, and $w$ is the width of the spin channel. The FM detectors have magnetisation $\vec{M}$ along $\pm\hat{x}$ and are characterised by the polarisation factor $P_d$. Nonlocal resistance is defined as $R_{nl} \equiv V_{nl}/I$. By solving Eq. 7.5, the following expressions for $R_{nl}$ are obtained for $\vec{B}$ along $\hat{y}$ and for $\vec{B}$ along $\hat{z}$

$$R_{nl}(B_y) = \frac{R_{sh}\, P_d}{4\, w} \,\mathrm{Re}\left[ \frac{(P_x - i\, P_z)\, \exp\left[ - \sqrt{\frac{1 - i\, \tau_s\, \omega}{D\, \tau_s}}\, y_d \right]}{4 \sqrt{\frac{1 - i\, \tau_s\, \omega}{D\, \tau_s}}} + \text{h.c.} \right] \tag{7.7}$$

$$R_{nl}(B_z) = \frac{R_{sh}\, P_d}{4\, w} \,\mathrm{Re}\left[ \frac{(P_x + i\, P_y)\, \exp\left[ - \sqrt{\frac{1 - i\, \tau_s\, \omega}{D\, \tau_s}}\, y_d \right]}{4 \sqrt{\frac{1 - i\, \tau_s\, \omega}{D\, \tau_s}}} + \text{h.c.} \right] \,, \tag{7.8}$$

where $\omega = \gamma_c\, B$ and $R_{sh}$ is the sheet resistance of the spin channel.

Spin injection efficiency $\vec{P}$ can be determined by fitting the spin precession response to Eqs. 7.7 and 7.8. The spin-injection angles for spins moving towards $\pm\hat{y}$, defined as

$$\theta^{\pm} \equiv \arctan\left( P_z^{\pm} / \sqrt{(P_x^{\pm})^2 + (P_y^{\pm})^2} \right) \tag{7.9}$$

and

$$\phi^{\pm} \equiv \arctan(P_y^{\pm}/P_x^{\pm}) \,, \tag{7.10}$$

fully characterise the orientation of the injected spins on both sides of the CSI region. Therefore, comparing $\theta^+$ with $\theta^-$ and $\phi^+$ with $\phi^-$ provides direct information on $J_{sc}$ and $J_{sd}$. In addition, systematic errors related to possible differences in polarisations of the FM detectors, can be eliminated by focusing on $\theta^{\pm}$ and $\phi^{\pm}$, rather than $\vec{P}^{\pm}$.

The above discussion does not address the spin dynamics within the graphene/$WTe_2$ bilayer, which may exhibit anisotropy as in the case of the graphene/$PdSe_2$ bilayer (see Chapter 6). This information, along with the CSI conversion angles, is contained in $\vec{P}^{\pm}$ and cannot be independently extracted from these devices. Nevertheless, this is not required for the present analysis.

## 7.4 Determination of crystallographic directions of $WTe_2$

The crystallographic orientation of the $WTe_2$ crystal in the device is determined with linearly polarised Raman spectroscopy. The polarisation of incident laser light $\vec{E}$ is rotated at an angle $\alpha$ relative to the long edge of $WTe_2$, corresponding to $\hat{x}$ (inset of Fig. 7.4). As for $PdSe_2$ (Chapter 6), the Raman spectra of $WTe_2$ display several characteristic vibrational modes whose magnitude varies with $\alpha$ (Fig. 7.4a). Knowing the relationship between the intensity of the modes and the polarisation angle of the incident light [52], crystallographic axes of $WTe_2$ can be determined. Fig. 7.4b shows, that the ratio $A_1^5$ (164 $cm^{-1}$)/$A_1^2$ (212 $cm^{-1}$) is maximum at $\alpha = 0$, which means that $\hat{a} \parallel \hat{x}$ in the device.

In addition, Raman spectroscopy allows one to determine the presence or absence of strain in $WTe_2$. The presence of strain in crystals influences their vibrational modes, leading to shifts of characteristic Raman peaks from their normal position [53]. Even a small strain of 0.5% results in noticeable shifts of the Raman modes. However, the Raman spectra of the thin $WTe_2$ flake integrated into the graphene device do not show any shift of the peaks compared to the bulk flake on $SiO_2$, and the positions of the peaks are identical to those reported in the literature. Thus, the strain in the $WTe_2$ flake is negligible and the symmetry breaking due to the strain can be excluded.

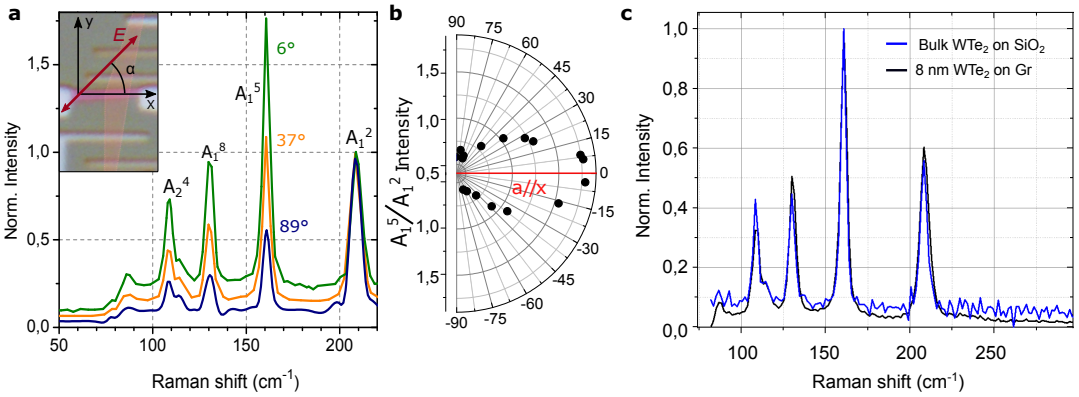


**Fig. 7.4: a.** Polarised Raman spectra for three different polarisation angles $\alpha$, defined in the inset. **b.** Polar plot of the ratio of the modes $A_1^5$ and $A_1^2$ intensities as a function of $\alpha$. The red line indicates the maximum of the $A_1^5/A_1^2$ intensity and corresponds to the $\hat{a}$ crystallographic direction. **c.** Raman spectra of 8 nm thin and bulk $WTe_2$ demonstrating the absence of strain.

## 7.5 Charge and spin transport in graphene/$WTe_2$ device

The graphene/$WTe_2$ device fabrication follows the steps established in Chapter 4. $WTe_2$ was exfoliated in a glovebox and a thin flake was selected to limit the bulk CSI contributions. The device comprises an 8-nm thick $WTe_2$ flake stacked on a 1.5 µm wide graphene channel and several lithographically defined spin-sensitive FM and spin-insensitive NM electrodes. The thickness of the $WTe_2$ flake was obtained by AFM measurement. $WTe_2$ of this thickness appears magenta on the 440 nm $SiO_2/Si^{++}$ substrate (Fig. 7.5a).

The spin transport properties of the bare graphene and FM electrodes are characterised using the two reference regions on both sides of $WTe_2$ (Ref1 and Ref2; marked by green and orange ellipses in Fig. 7.5a). Spin precession under an out-of-plane magnetic field $B_z$ enables the extraction of parameters $\tau_s$, $D_s$, and $P_d$ required for fitting CSI data (see Eqs. 7.7 and 7.8). The parameters extracted from the measurements in Fig. 7.5b) are $\tau_s = (100 \pm 10)$ ps, $D_s = (0.020 \pm 0.004)$ $m^2 s^{-1}$, and $P_d = (12 \pm 3)\%$, with the spin diffusion length $\lambda_s = \sqrt{\tau_s D_s} \cong 1.4$ µm in bare graphene. The rather small $\lambda_s$ can be attributed to contamination introduced during sample fabrication. This contamination can be seen in the AFM image taken once the spin-transport experiments were finished (inset of Fig. 7.5c). The extent of graphene channel contamination can also be deduced from the back-gate measurements of longitudinal resistance measured in a four-point configuration ($R_{4p}$ vs $V_g$). Fig. 7.5c shows back-gate measurements for the three regions — Ref1, Ref2, and graphene/$WTe_2$ bilayer. In those measurements, a charge current $I$ is always applied between electrodes NM3 and NM4, while voltage drop is measured between FM4 and FM3 (Ref1), FM2 and FM1 (Ref2) or FM3 and FM2 (bilayer).

Indeed, CNP points are shifted to 27 V and 34 V for Ref1 and Ref2, respectively, indicating the presence of p-type dopants on the graphene channel. The resistance measurement in the region with the bilayer displays two local maxima likely because the proximitized graphene covered with $WTe_2$ flake is protected from contamination and has a CNP close to 0 V; however, the shift could also be due to charge transfer.

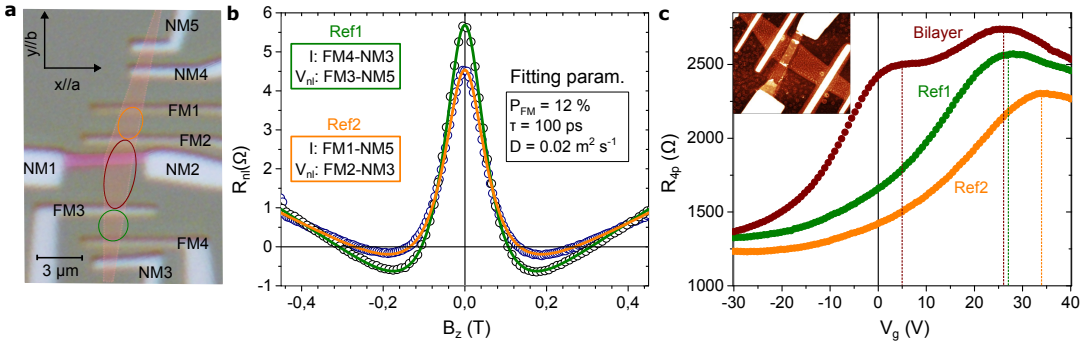


**Fig. 7.5: a.** Optical image of the device. The graphene channel, roughly oriented in $\hat{y}$ direction, is highlighted pink. Ellipses highlight the three spin diffusion regions (Ref1, Ref2, Bilayer) **b.** Hanle precession measurements in the two reference regions. **c.** Backgate dependence of the resistance of spin diffusion regions. Inset shows the AFM image of the device taken after the spin-transport measurements.

The CSI is investigated by applying a charge current $I$ along the $WTe_2$ crystal ($\hat{a} \parallel \hat{x}$ direction). Nonlocal voltages $V_{\rm nl}^{(+y_d)}$ and $V_{\rm nl}^{(-y_d)}$ are measured at $\pm y_d$ with $\vec{M}$ of the FM detectors saturated in $\pm\hat{x}$ direction, i.e. $\vec{M}(+x)$ and $\vec{M}(-x)$ (Fig. 7.6a). The blue and red lines in Fig. 7.6b, show $R_{\rm nl}^{(+y_d)}$ vs. $B_z$ for these two $\vec{M}$ configurations giving $R_{\rm nl}^{+}$ and $R_{\rm nl}^{-}$, respectively. The average of the two curves $(R_{\rm nl}^{+} + R_{\rm nl}^{-})/2$ provides the background of the measurement. The background is associated with spin-unrelated spurious signals and the FM magnetisation rotation (as $\vec{B} \perp \vec{M}$). The background is removed by taking the difference between the two curves $R_{\rm nl}^{(+y_d)} = (R_{\rm nl}^{+} - R_{\rm nl}^{-})$, providing the pure spin signal in Fig. 7.6b. This protocol is used to obtain pure spin signal at both ends of the sample ($\pm y_d$) and for both magnetic field configurations — $B_z$ and $B_y$.

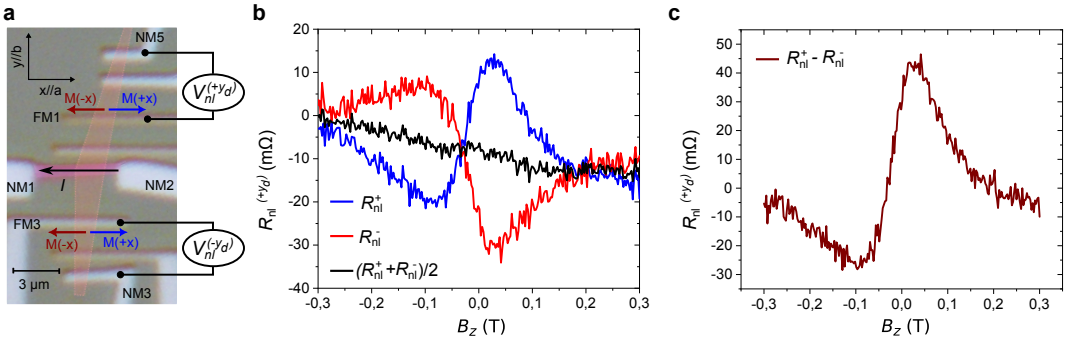


**Fig. 7.6: a.** CSI measurement configurations sketched on the optical image of the device. **b.** $R_{nl}^{+}$, $R_{nl}^{-}$ and the spin-independent background vs. $B_z$ measured at $+y_d$. **c.** Difference $R_{\rm nl}^{+} - R_{\rm nl}^{-}$ showing only the pure spin signal.

Figure 7.7 shows the pure spin signals $R_{\rm nl}^{(+y_d)}$ and $R_{\rm nl}^{(-y_d)}$ vs. $B_y$ and $B_z$. Remarkably, $R_{\rm nl}^{(+y_d)}$ and $R_{\rm nl}^{(-y_d)}$ have nearly indistinguishable lineshapes for $B_z$ (Fig. 7.7a, b). In contrast, they differ significantly for $B_y$ (7.7c, d).

In the case of $B_z$, only the in-plane ($xy$) spin components of the injected spins contribute to the precession lineshape. Therefore, the fact that $R_{\rm nl}^{(+y_d)} \sim R_{\rm nl}^{(-y_d)}$ demonstrates that the spins diffusing toward $-\hat{y}$ and $+\hat{y}$ have the same in-plane spin polarisation, which is an indication of a uniform in-plane spin polarisation in the CSI region (associated with $J_{\rm sd}$ in Fig. 7.3). Moreover, because $R_{\rm nl}^{(+y_d)}$ and $R_{\rm nl}^{(-y_d)}$ are neither fully symmetric nor fully antisymmetric about $B_z = 0$, the spin polarisation has nonzero components along both $\hat{x}$ and $\hat{y}$.

In contrast, in the case of $B_y$ only the spin components in the $xz$ plane contribute to the precession lineshape. The marked difference between $R_{\rm nl}^{(+y_d)}$ and $R_{\rm nl}^{(-y_d)}$ demonstrates that the spins diffusing towards $-\hat{y}$ and $\hat{y}$ have different spin polarisation orientations in the $xz$ plane. Combined with the results for $B_z$, this observation is an unambiguous indication of a spin-polarised current in the CSI region with a polarisation along $\hat{z}$ (associated with $J_{\rm sc}$ in Fig. 7.3). Furthermore, $R_{\rm nl}^{(+y_d)}$ being rather symmetric about $B_y = 0$ (Fig. 7.7d) demonstrates the presence of a uniform spin density along $\hat{z}$, originating from $J_{\rm sd}$, which partially compensates the contribution from $J_{\rm sc}$.

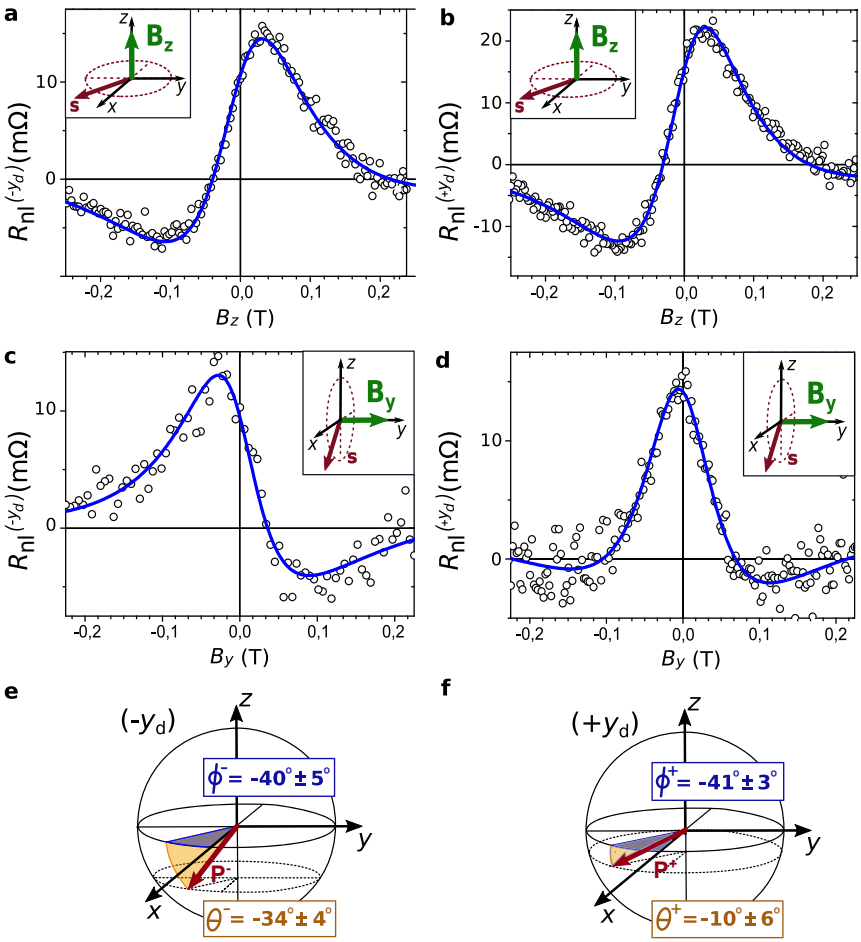


**Fig. 7.7:** Pure spin signals $R_{nl}^{(-y_d)}$ (**a**, **c**) and $R_{nl}^{(+y_d)}$ (**b**, **d**) measured as a function of $B_z$ (**a**, **b**) and $B_y$ (**c**, **d**). Open circles show the experimental data and the blue lines corresponding fits obtained with Eqs. 7.7 and 7.8. The insets represent the magnetic field direction and the correspondent spin precession plane. CSI angles extracted from the fits of $R_{nl}^{(-y_d)}$ (**e**) and $R_{nl}^{(+y_d)}$ (**f**).

To quantify the relative magnitudes of each CSI component, the data in Fig. 7.7 are fitted to Eqs. 7.7 and 7.8. The spin polarisation angles $\theta^{\pm}$ and $\phi^{\pm}$, are:

$$(\phi^-\,,\,\theta^-) = (-40^\circ \pm 5^\circ\,,\,-34^\circ \pm 4^\circ) \quad \text{and} \quad (\phi^+\,,\,\theta^+) = (-41^\circ \pm 3^\circ\,,\,-10^\circ \pm 6^\circ).$$

As the homogeneously diffusing spins $J_{sd}$ lead to identical spin accumulations on both sides of the sample ($\pm y$), they are characterised by the symmetric angular component

$$(\phi_{sym}\,,\,\theta_{sym}) = \left(\frac{1}{2}(\phi^+ + \phi^-)\,,\,\frac{1}{2}(\theta^+ + \theta^-)\right) = (-41^\circ \pm 4^\circ\,,\,-22^\circ \pm 5^\circ).$$

In contrast, the spins originating from the directed $J_{sc}$ lead to spin accumulations with opposite signs on each side and are characterised by the antisymmetric component

$$(\phi_{asym}\,,\,\theta_{asym}) = \left(\frac{1}{2}(\phi^+ - \phi^-)\,,\,\frac{1}{2}(\theta^+ - \theta^-)\right) = (0^\circ \pm 4^\circ\,,\,-12^\circ \pm 5^\circ).$$

The symmetric CSI angular components suggest the coexistence of uniform spin density with polarisation components along all three coordinate axes. In contrast, the antisymmetric CSI angular components hint at a directed spin-Hall current $J_{s,y}$ with spin polarisation along $\hat{z}$ ($\phi_{\text{asym}} \approx 0$).

Unequivocal identification of the underlying CSI mechanisms requires analysis based on the symmetries of the investigated system. CSI can originate from either the ISGE or the SHE, in the bulk of $WTe_2$, at the graphene/$WTe_2$ interface or in proximitized graphene. The next section discusses the possible origins of each of the measured CSI components.

## 7.6 Origin of the observed CSI in graphene/$WTe_2$

The spin density in the CSI region has components along all three spatial axes. According to the bulk $T_d$-$WTe_2$ crystal symmetries, for a current along $a$ ($\hat{x}$) only the spin polarisation component along $\hat{y}$ is allowed. The ISGE can generate a spin density with spin polarisation along $\hat{y}$, while the spin Hall current flowing along $\hat{z}$ ($J_{s,z}$) should also be polarised along $\hat{y}$. Therefore, the components of $J_{\text{sd}}$ along $\hat{x}$ and $\hat{z}$ are not expected in the bulk of $T_d$-$WTe_2$, indicating that they originate from an interfacial or proximity-induced effect in graphene [54].

The symmetry of a heterostructure or thin crystal can be equal to or lower than that of its bulk constituents, permitting additional nonzero spin polarisation components. Indeed, in the graphene/$WTe_2$ interface, the glide symmetry is absent, possibly leaving only the single mirror symmetry plane $\mathcal{M}_a$ (see Fig. 7.2). The generation of a spin density along $c$ ($\hat{z}$), when $J_c$ is along $a$ ($\hat{x}$), would then be allowed.

A spin density along $\hat{x}$ was previously observed in graphene/$MoTe_2$ and graphene/$WTe_2$ and was ascribed to additional bulk mirror symmetry breaking induced possibly by strain in the TMDC [29, 30]. In our experiments, Raman spectroscopy demonstrates that $WTe_2$ is not under strain, making this explanation implausible. Alternatively, the spin density along $\hat{x}$ could be generated by a current component along $\hat{y}$. Recent theoretical publications reported anisotropic SHE in $WTe_2$ and $MoTe_2$ as a function of the direction of the charge current and the position of the Fermi energy [55, 56]. However, the elongated geometry of our $WTe_2$ flake implies that the current component along $\hat{y}$ is small; therefore, a large CSI efficiency would be required to make this scenario viable. These observations suggest that the spin density along $\hat{x}$ is likely generated in proximitized graphene.

Recent first-principles calculations that address the twist angle dependence of proximity-induced SOC in graphene by 2H TMDCs ($MoS_2$, $MoSe_2$, $WS_2$ and $WSe_2$) have shown that the Rashba SOC could exhibit a radial component, thus deviating from the typical tangential orientation [57, 58]. The radial component is allowed for twist angles between the graphene and TMDC lattices that are different from 0° and 30°, where mirror symmetries are broken. Similarly, an arbitrary twist angle between the graphene and $WTe_2$ crystal lattices can break the remaining symmetry. At their

interface, with radial Rashba SOC coupling, a spin polarisation component parallel to $J_c$ may arise.

Finally, although the symmetries of bulk $WTe_2$ allow spin Hall current along $\hat{y}$, which is polarised along $\hat{z}$ ($J^z_{s,y}$), it has not been reported in prior graphene/$WTe_2$ studies [30, 46]. This component is allowed even in high-symmetry structures and has been reported in graphene-$MoS_2$ and graphene-$WS_2$ [22–24]. In these experiments, a spin density with polarisation along $\hat{y}$ was also found. Furthermore, it was confirmed that the spin current polarised along $\hat{z}$ and the spin density along $\hat{y}$ can originate solely from the SHE and ISGE in proximitized graphene, respectively.

The previous discussion strongly suggests that the unconventional CSI components in graphene/$WTe_2$ originate from proximity effects. In contrast, the observed spin current with polarisation along $\hat{z}$ and the spin densities with polarisation along $\hat{y}$ (conventional CSI components) are permitted also in the bulk of $T_d$-$WTe_2$. Quantifying spin absorption in $WTe_2$ could help to separate these remaining CSI contributions; however, the analysis is not straightforward or free of ambiguities. Spin absorption estimation requires detailed knowledge of heterostructure properties that cannot be readily obtained in these nonlocal devices incorporating a high conductivity $WTe_2$ semimetal (compare with the discussion on $PdSe_2$ in Chapter 6). The properties include the precise interface resistance between graphene and $WTe_2$ and the spin relaxation parameters in the proximitized graphene and $WTe_2$. Any subtle change in these parameters or the implementation of the spin absorption model can lead to divergent conclusions. In addition, due to the 2D nature of graphene, the spin absorption is not uniform at the graphene/$WTe_2$ interface, even if the spin current absorption occurs along $\hat{z}$. This can be easily understood by considering the inverse SHE, commonly used in CSI experiments. Because of the spin relaxation and the fact that there is no alternative path for spins to cross the CSI region, as in a 3D system, most spins will be absorbed on the side of graphene/$WTe_2$ closest to the FM injector. This could lead to a spin accumulation gradient (and a spin current) in the TMDC along the spin channel.

## References

[1] L. Camosi et al.; “Resolving spin currents and spin densities generated by charge-spin interconversion in systems with reduced crystal symmetry”. *2D Materials* 2022**, 9**, p. 035014. DOI: 10.1088/2053-1583/ac6fec.

[2] M. Dyakonov and V. Perel; “Spin orientation of electrons associated with the interband absorption of light in semiconductors”. *Soviet Physics JETP* 1971**, 33**, pp. 1053–1059.

[3] M. Z. Hasan and C. L. Kane; “Colloquium: Topological insulators”. *Reviews of Modern Physics* 2010**, 82**, pp. 3045–3067. DOI: 10.1103/RevModPhys.82.3045.

[4] A. N. Bogdanov and U. K. Rößler; "Chiral Symmetry Breaking in Magnetic Thin Films and Multilayers". *Physical Review Letters* 2001**, 87**, p. 037203. DOI: 10.1103/PhysRevLett.87.037203.

[5] C. L. Kane and E. J. Mele; "$Z_2$ Topological Order and the Quantum Spin Hall Effect". *Physical Review Letters* 2005**, 95**, p. 146802. DOI: 10.1103/PhysRevLett.95.146802.

[6] C.-Z. Chang and M. Li; "Quantum Anomalous Hall Effect in Time-Reversal-Symmetry Breaking Topological Insulators". *Journal of Physics: Condensed Matter* 2016**, 28**, p. 123002. DOI: 10.1088/0953-8984/28/12/123002.

[7] A. Manchon et al.; "New perspectives for Rashba spin–orbit coupling". *Nature Materials* 2015**, 14**, pp. 871–882. DOI: 10.1038/nmat4360.

[8] J. Sinova et al.; "Spin Hall effects". *Reviews of Modern Physics* 2015**, 87**, pp. 1213–1260. DOI: 10.1103/RevModPhys.87.1213.

[9] A. Soumyanarayanan et al.; "Emergent phenomena induced by spin–orbit coupling at surfaces and interfaces". *Nature* 2016**, 539**, pp. 509–517. DOI: 10.1038/nature19820.

[10] M. I. D'yakonov and V. I. Perel'; "Possibility of orienting electron spins with current". *ZhETF Pis. Red.* 1971**, 13**, pp. 657–660.

[11] M. I. Dyakonov and V. I. Perel; "Current-induced spin orientation of electrons in semiconductors". *Physics Letters A* 1971**, 35**, pp. 459–460. DOI: 10.1016/0375-9601(71)90196-4.

[12] J. E. Hirsch; "Spin Hall Effect". *Physical Review Letters* 1999**, 83**, pp. 1834–1837. DOI: 10.1103/PhysRevLett.83.1834.

[13] S. D. Ganichev et al.; "Spin-galvanic effect". *Nature* 2002**, 417**, pp. 153–156. DOI: 10.1038/417153a.

[14] L. Onsager; "Reciprocal Relations in Irreversible Processes. II." *Physical Review* 1931**, 38**, pp. 2265–2279. DOI: 10.1103/PhysRev.38.2265.

[15] P. Jacquod et al.; "Onsager relations in coupled electric, thermoelectric, and spin transport: The tenfold way". *Physical Review B* 2012**, 86**, p. 155118. DOI: 10.1103/PhysRevB.86.155118.

[16] Y. K. Kato et al.; "Observation of the Spin Hall Effect in Semiconductors". *Science* 2004**, 306**, pp. 1910–1913.

[17] J. Wunderlich et al.; "Experimental Observation of the Spin-Hall Effect in a Two-Dimensional Spin-Orbit Coupled Semiconductor System". *Physical Review Letters* 2005**, 94**, p. 047204. DOI: 10.1103/PhysRevLett.94.047204.

[18] S. O. Valenzuela and M. Tinkham; "Direct electronic measurement of the spin Hall effect". *Nature* 2006**, 442**, pp. 176–179. DOI: 10.1038/nature04937.

[19] E. Saitoh et al.; "Conversion of spin current into charge current at room temperature: Inverse spin-Hall effect". *Applied Physics Letters* 2006**, 88**, p. 182509. DOI: 10.1063/1.2199473.

[20] T. Kimura et al.; "Room-Temperature Reversible Spin Hall Effect". *Physical Review Letters* 2007**, 98**, p. 156601. DOI: 10.1103/PhysRevLett.98.156601.

[21] B. Dieny et al.; "Opportunities and challenges for spintronics in the microelectronics industry". *Nature Electronics* 2020**, 3**, pp. 446–459. DOI: 10.1038/s41928-020-0461-5.

[22] T. S. Ghiasi et al.; "Charge-to-Spin Conversion by the Rashba–Edelstein Effect in Two-Dimensional van der Waals Heterostructures up to Room Temperature". *Nano Letters* 2019**, 19**, pp. 5959–5966. DOI: 10.1021/acs.nanolett.9b01611.

[23] C. K. Safeer et al.; "Room-Temperature Spin Hall Effect in Graphene/$MoS_2$ van der Waals Heterostructures". *Nano Letters* 2019**, 19**, pp. 1074–1082. DOI: 10.1021/acs.nanolett.8b04368.

[24] L. A. Benítez et al.; "Tunable room-temperature spin galvanic and spin Hall effects in van der Waals heterostructures". *Nature Materials* 2020**, 19**, pp. 170–175. DOI: 10.1038/s41563-019-0575-1.

[25] J. H. Garcia, A. W. Cummings, and S. Roche; "Spin Hall Effect and Weak Antilocalization in Graphene/Transition Metal Dichalcogenide Heterostructures". *Nano Letters* 2017**, 17**, pp. 5078–5083. DOI: 10.1021/acs.nanolett.7b02364.

[26] M. Offidani et al.; "Optimal Charge-to-Spin Conversion in Graphene on Transition-Metal Dichalcogenides". *Physical Review Letters* 2017**, 119**, p. 196801. DOI: 10.1103/PhysRevLett.119.196801.

[27] S. A. Cavill et al.; "Proposal for Unambiguous Electrical Detection of Spin-Charge Conversion in Lateral Spin Valves". *Physical Review Letters* 2020**, 124**, p. 236803. DOI: 10.1103/PhysRevLett.124.236803.

[28] D. MacNeill et al.; "Control of spin–orbit torques through crystal symmetry in $WTe_2$/ferromagnet bilayers". *Nature Physics* 2017**, 13**, pp. 300–305. DOI: 10.1038/nphys3933.

[29] C. K. Safeer et al.; "Large Multidirectional Spin-to-Charge Conversion in Low-Symmetry Semimetal $MoTe_2$ at Room Temperature". *Nano Letters* 2019**, 19**, pp. 8758–8766. DOI: 10.1021/acs.nanolett.9b03485.

[30] B. Zhao et al.; "Unconventional Charge–Spin Conversion in Weyl-Semimetal $WTe_2$". *Advanced Materials* 2020**, 32**, p. 2000818. DOI: 10.1002/adma.202000818.

[31] C. K. Safeer et al.; "Reliability of spin-to-charge conversion measurements in graphene-based lateral spin valves". *2D Materials* 2022**, 9**, p. 015024. DOI: 10.1088/2053-1583/ac3c9b.

[32] S.-Y. Xu et al.; "Electrically switchable Berry curvature dipole in the monolayer topological insulator $WTe_2$". *Nature Physics* 2018**, 14**, pp. 900–906. DOI: 10.1038/s41567-018-0189-6.

[33] A. A. Soluyanov et al.; "Type-II Weyl semimetals". *Nature* 2015**, 527**, pp. 495–498. DOI: 10.1038/nature15768.

[34] P. Li et al.; "Evidence for topological type-II Weyl semimetal $WTe_2$". *Nature Communications* 2017**, 8**, p. 2150. DOI: 10.1038/s41467-017-02237-1.

[35] Z. Fei et al.; "Edge conduction in monolayer $WTe_2$". *Nature Physics* 2017**, 13**, pp. 677–682. DOI: 10.1038/nphys4091.

[36] S. Tang et al.; "Quantum spin Hall state in monolayer $1T'$-$WTe_2$". *Nature Physics* 2017**, 13**, pp. 683–687. DOI: 10.1038/nphys4174.

[37] S. Wu et al.; "Observation of the quantum spin Hall effect up to 100 kelvin in a monolayer crystal". *Science* 2018**, 359**, pp. 76–79. DOI: 10.1126/science.aan6003.

[38] A. Roy, M. H. D. Guimarães, and J. Sławińska; "Unconventional spin Hall effects in nonmagnetic solids". *Physical Review Materials* 2022**, 6**, p. 045004. DOI: 10.1103/PhysRevMaterials.6.045004.

[39] M. Seemann et al.; "Symmetry-imposed shape of linear response tensors". *Physical Review B* 2015**, 92**, p. 155138. DOI: 10.1103/PhysRevB.92.155138.

[40] J.-W. Luo, G. Bester, and A. Zunger; "Full-Zone Spin Splitting for Electrons and Holes in Bulk GaAs and GaSb". *Physical Review Letters* 2009**, 102**, p. 056405. DOI: 10.1103/PhysRevLett.102.056405.

[41] X. Zhang et al.; "Hidden spin polarization in inversion-symmetric bulk crystals". *Nature Physics* 2014**, 10**, pp. 387–393. DOI: 10.1038/nphys2933.

[42] Y. A. Bychkov and E. I. Rashba; "Oscillatory effects and the magnetic susceptibility of carriers in inversion layers". *Journal of Physics C: Solid State Physics* 1984**, 17**, pp. 6039–6045. DOI: 10.1088/0022-3719/17/33/015.

[43] G. Bihlmayer, O. Rader, and R. Winkler; "Focus on the Rashba effect". *New Journal of Physics* 2015**, 17**, p. 050202. DOI: 10.1088/1367-2630/17/5/050202.

[44] W. S. Torres et al.; "Spin precession and spin Hall effect in monolayer graphene/Pt nanostructures". *2D Materials* 2017**, 4**, p. 041008. DOI: 10.1088/2053-1583/aa8823.

[45] W. Yan et al.; "Large room temperature spin-to-charge conversion signals in a few-layer graphene/Pt lateral heterostructure". *Nature Communications* 2017**, 8**, p. 661. DOI: 10.1038/s41467-017-00563-y.

[46] B. Zhao et al.; "Observation of charge to spin conversion in Weyl semimetal $WTe_2$ at room temperature". *Physical Review Research* 2020**, 2**, p. 013286. DOI: 10.1103/PhysRevResearch.2.013286.

[47] S. Zhang; "Spin Hall Effect in the Presence of Spin Diffusion". *Physical Review Letters* 2000**, 85**, pp. 393–396. DOI: 10.1103/PhysRevLett.85.393.

[48] C. Stamm et al.; "Magneto-Optical Detection of the Spin Hall Effect in Pt and W Thin Films". *Physical Review Letters* 2017**, 119**, p. 087203. DOI: 10.1103/PhysRevLett.119.087203.

[49] H. C. Torrey; "Bloch Equations with Diffusion Terms". *Physical Review* 1956**, 104**, pp. 563–565. DOI: 10.1103/PhysRev.104.563.

[50] M. Johnson and R. H. Silsbee; "Coupling of electronic charge and spin at a ferromagnetic-paramagnetic metal interface". *Physical Review B* 1988**, 37**, pp. 5312–5325. DOI: 10.1103/PhysRevB.37.5312.

[51] B. Raes et al.; "Determination of the spin-lifetime anisotropy in graphene using oblique spin precession". *Nature Communications* 2016**, 7**, p. 11444. DOI: 10.1038/ncomms11444.

[52] Q. Song et al.; "The In-Plane Anisotropy of $WTe_2$ Investigated by Angle-Dependent and Polarized Raman Spectroscopy". *Scientific Reports* 2016**, 6**, p. 29254. DOI: 10.1038/srep29254.

[53] W. Yang et al.; "Raman-active modes of 1$T'$-$WTe_2$ under tensile strain: A first-principles prediction". *Physical Review B* 2019**, 99**, p. 235401. DOI: 10.1103/PhysRevB.99.235401.

[54] F. Xue and P. M. Haney; "Staggered spin Hall conductivity". *Physical Review B* 2020**, 102**, p. 195146. DOI: 10.1103/PhysRevB.102.195146.

[55] J. Zhou et al.; "Intrinsic spin Hall conductivity of the semimetals $MoTe_2$ and $WTe_2$". *Physical Review B* 2019**, 99**, p. 060408. DOI: 10.1103/PhysRevB.99.060408.

[56] M. Vila et al.; "Low-symmetry topological materials for large charge-to-spin interconversion: The case of transition metal dichalcogenide monolayers". *Physical Review Research* 2021**, 3**, p. 043230. DOI: 10.1103/PhysRevResearch.3.043230.

[57] T. Naimer et al.; "Twist-angle dependent proximity induced spin-orbit coupling in graphene/transition metal dichalcogenide heterostructures". *Physical Review B* 2021**, 104**, p. 195156. DOI: 10.1103/PhysRevB.104.195156.

[58] Y. Li and M. Koshino; "Twist-angle dependence of the proximity spin-orbit coupling in graphene on transition-metal dichalcogenides". *Physical Review B* 2019**, 99**, p. 075438. DOI: 10.1103/PhysRevB.99.075438.

# Chapter 8

# Conclusions and Outlook

The use of SOC in spintronic devices to interconvert charge and spin and manipulate the flow of spin currents shows great promise for future energy-efficient information technologies. Graphene is a perfect material for spin transport over long distances because of its intrinsically small SOC. However, spin manipulation without SOC is challenging. Graphene proximitized with 2DMs containing heavy atoms such as TMDCs exhibits a sizeable SOC on the order of a few to tens of meV while preserving its superior charge transport properties. The proximity-induced SOC in graphene allows for efficient FM-free spin injection or detection through CSI. Moreover, induced spin textures can be used for spin filtering due to the large spin relaxation anisotropy between spins in different directions. However, a deep understanding of proximity-induced SOC physics is required to master the control the spin dynamics. Recently, heterostructures comprising crystals with disparate lattices were predicted to exhibit novel SOC and spin textures. Moreover, the low symmetry of such heterostructures may result in unconventional CSI components. In this context, this thesis explored the proximity-induced SOC in heterostructures comprising graphene and low-symmetry TMDCs through spin relaxation and CSI measurements. The main achievements are:

- Theoretical analysis of spin diffusion and precession in partially proximitized graphene displaying distinct spin lifetimes along three spatial directions. Modelling the spin density across the sample and the expected lineshape of precession curves for various geometric and spin transport parameters.
- Development of a measurement protocol for identifying spin lifetimes in a highly anisotropic system and characterising the dominant spin textures driving spin relaxation within a Dyakonov-Perel mechanism.
- Demonstration of a large proximity-induced in-plane spin relaxation anisotropy in low-symmetry graphene/$PdSe_2$ vdW heterostructures up to room temperature. Such robust in-plane anisotropy has not been observed in any prior work.
- Demonstration of efficient control of the in-plane spin relaxation anisotropy in the graphene/$PdSe_2$ vdW heterostructure by an external electric field. The in-plane anisotropy is highly gate tunable exhibiting a modulation from $\zeta_{xy} \approx 12.5$ to $\zeta_{xy} \approx 2$.

- Development of a measurement protocol for disentangling spin currents and spin densities generated by CSI.
- Demonstration of the possibility to generate spins with polarisation components in three spatial directions through unconventional CSI in graphene/$WTe_2$ heterostructures.

Previous works have demonstrated a large spin relaxation anisotropy between in-plane and out-of-plane spins in graphene/2H-TMDC heterostructures resulting from the out-of-plane valley-Zeeman SOC directly imprinted into graphene from the 2H-TMDC [1–3]. Graphene/2H-TMDC heterostructures may serve as spin-filtering devices that predominantly transmit the out-of-plane spin component. However, the in-plane relaxation remains isotropic in these heterostructures.

In contrast, the experimental data presented in Chap. 6 demonstrate that graphene/$PdSe_2$ heterostructures are characterised by large in-plane relaxation anisotropy where strong in-plane persistent SOF dominates spin transport. Therefore, in-plane spin filtering is achievable in devices based on graphene/low-symmetry TMDCs. Moreover, the simulations performed in Chap. 5 and the experimental data presented in Chap. 6, demonstrate that magnetic-field-free spin rotation can be achieved in devices where the long spin lifetime axis is neither parallel nor perpendicular to the spin injection direction. This is a consequence of a faster relaxation of the spin component parallel to the short spin lifetime axis. The spin rotation angle depends strongly on $\zeta_{xy}$, which is highly gate-tunable, therefore, spin polarisation of transmitted spins can be controlled by an external electric field. The possibility of in-plane spin filtering and magnetic-field-free manipulation of spin polarisation opens pathways for new spin-circuit architectures.

The identified direction of the persistent SOF is different for the two measured samples presented in Chap. 6 suggesting that it likely depends on the twisting between graphene and $PdSe_2$. Further research is needed to address the twist angle dependence . Namely, theoretical calculations of the expected spin texture in graphene/$PdSe_2$ should be performed, focusing on the influence of twisting and Fermi level position similar to studies conducted for high-symmetry graphene/2H-TMDC heterostructures [4–7]. Additional experiments exploring the carrier density dependence would also be of interest. While our results demonstrate that carrier density significantly modifies the anisotropy in one of our devices, the Fermi level in the graphene/$PdSe_2$ region was not unambiguously identified. No distinct CNP was observed in this region, potentially because it coincides with that of pristine graphene or due to the narrowness of the $PdSe_2$ flake, which reduces the impact on the overall resistance of the spin channel.

The results in Chap. 7 demonstrate that the CSI in graphene/$WTe_2$ heterostructures, with a current along the $a$ axis of $WTe_2$, can generate spin-polarised carriers with polarisation components in all three spatial directions. As a spin accumulation with polarisation along the applied current is not allowed in the $WTe_2$ bulk, it can

only stem from the graphene/$WTe_2$ interface. It likely involves the emergence of a radial component in proximity-induced Rashba SOC, originating from twisting [4, 5]. The radial component in graphene proximitized by semiconducting TMDCs has been predicted to be extremely sensitive to twist angle, unintended doping, and carrier density [5]. Therefore, systematic investigations of the dependence of spin accumulation parallel to the current as a function of twist angle and gate voltage are needed to understand its origin. Another important experiment that should be conducted to understand proximity-induced spin textures in graphene/$WTe_2$ is the investigation of a device comprising graphene Hall-cross and a monolayer $WTe_2$. In the monolayer limit, bulk CSI phenomena will be absent and only the interfacial CSI will generate spins. Finally, investigating the CSI in graphene/$PdSe_2$ could directly circumvent the challenges posed by semimetals as $WTe_2$ and $MoTe_2$, as in this material spin absorption is shown not to affect spin dynamics.

## References

[1] T. S. Ghiasi et al.; "Large Proximity-Induced Spin Lifetime Anisotropy in Transition-Metal Dichalcogenide/Graphene Heterostructures". *Nano Letters* 2017**, 17**, pp. 7528–7532. DOI: 10.1021/acs.nanolett.7b03460.

[2] J. Ingla-Aynés et al.; "Electrical Control of Valley-Zeeman Spin-Orbit-Coupling–Induced Spin Precession at Room Temperature". *Physical Review Letters* 2021**, 127**, p. 047202. DOI: 10.1103/PhysRevLett.127.047202.

[3] L. A. Benítez et al.; "Strongly anisotropic spin relaxation in graphene–transition metal dichalcogenide heterostructures at room temperature". *Nature Physics* 2018**, 14**, pp. 303–308. DOI: 10.1038/s41567-017-0019-2.

[4] Y. Li and M. Koshino; "Twist-angle dependence of the proximity spin-orbit coupling in graphene on transition-metal dichalcogenides". *Physical Review B* 2019**, 99**, p. 075438. DOI: 10.1103/PhysRevB.99.075438.

[5] T. Naimer et al.; "Twist-angle dependent proximity induced spin-orbit coupling in graphene/transition metal dichalcogenide heterostructures". *Physical Review B* 2021**, 104**, p. 195156. DOI: 10.1103/PhysRevB.104.195156.

[6] T. Naimer and J. Fabian; "Twist-angle dependent proximity induced spin-orbit coupling in graphene/topological insulator heterostructures". *Physical Review B* 2023**, 107**, p. 195144. DOI: 10.1103/PhysRevB.107.195144.

[7] K. Zollner et al.; "Twist- and gate-tunable proximity spin-orbit coupling, spin relaxation anisotropy, and charge-to-spin conversion in heterostructures of graphene and transition metal dichalcogenides". *Physical Review B* 2023**, 108**, p. 235166. DOI: 10.1103/PhysRevB.108.235166.

# *Acknowledgements*

My pursuit of PhD would not have been possible without invaluable professional and personal support from numerous wonderful people. Therefore, I would like to express my deep gratitude to **all of you** who offered me your hand in case of need, wise insight when searching for answers, and kind words or even just a heart-warming smile.

First and foremost, I would like to offer my deep gratitude to **Sergio Valenzuela** for giving me the opportunity to pursue a PhD in his group. Thank you for granting me the academic freedom to explore various research ideas and nurturing my curiosity. Thank you for your approachability, kindness, and patient guidance. It has been a great privilege to work with you and learn from you in the process. I extend my deep gratitude to **Juan Sierra** for his immense practical and moral support at all stages of my PhD. Thank you for always being available and for your encouragement. Your calm approach to dealing with problems taught me what resilience in science means.

I would like to extend my sincere thanks to **Franz** for his encouragement, suggestions, and help towards the end of my PhD. I am thankful to **Lorenzo**, for his great enthusiasm, openness for collaborations, and being a good friend. Furthermore, I'd like to acknowledge **Thomas** for his excellent work on the measurement setups making the experimenting easier for everyone.

I appreciate **Marius**, **Williams**, **Matias**, and **Antonio** for showing me around the labs, sharing their recipes and device fabrication tricks with me, and always being available to help. I would like to thank **Iván** for accompanying me on this long journey and his friendship; **Elisa** and **Flavius** for being great office companions, **Nandu** and **Motomi** for the lunchtime discussions and **Victor** for all the magic. I also had the pleasure of working with **Regina** and **Adriana** , whom I thank for their infinite optimism and positivity. At the beginning of my PhD, countless coffee breaks shared with **Frédéric**, **Aloïs** and **Zewdu** brought intriguing discussions and stopped the rush of the day for a moment. I will also remember the fun shared at conferences with **Carmen**, **José**, **Aron**, **Omar**, and **Bingcheng**. Furthermore, I would like to offer my gratitude to **Markos** for his emotional support and encouragement whenever our paths crossed randomly in the corridors of ICN2, **Stephan** for countless interesting discussions we had, and **María José** for her kindness. **Raúl**, thank you for fighting for us the never-ending battle with entropy and maintaining the cleanroom working as it should. I would also like to recognize the support of **IT**, **maintenance**, and all the **administrative departments** of the ICN2. I further extend my appreciation to all the amazing people I have had the pleasure of meeting and working alongside at ICN2: **Patricia**, **Mireia**, **Enzo**, **Luis**, **David**, **Christina**, **Francisco**, **Marta**, **María**, **Guillermo**; and the institutes in its proximity, i.e. Raman spectroscopy and SQUID maestros from ICMAB: **Kai**, **Sebastian**, and **Bernat**; ARPES experts from ALBA: **Kevin**, **Ji**, and **Massimo** and CNM nanolithography specialists: **Xavier** and **Albert**.

This journey was made possible through generous financial support, for which I am deeply thankful. I received **funding** from the European Union's Horizon 2020 research and innovation programme under the Marie Skłodowska-Curie grant agreement No. 754558 (BIST PhD Fellowship Programme) and support from the European Union's Horizon 2020 FET-PROACTIVE project TOCHA, under grant agreement No. 824140.

Také bych chtěl poděkovat své **rodině** za jejich nekonečnou podporu během mých nekonečně dlouhých studií.

И накрая, но не на последно място, бих искал да благодаря на моята приятелка Илияна, че винаги е до мен и нейната подкрепа и любов. Обичам те обратно.

# Publications

1. J. Světlík, L. Camosi, J. F. Sierra, and S. O. Valenzuela, "Spin Dynamics in Heterogeneous Nonlocal Spin Devices: Interplay of Isotropic and Anisotropic Spin Relaxation". [in preparation].

2. J. F. Sierra*, J. Světlík*, W. Savero Torres, L. Camosi, F. Herling, T. Guillet, K. Xu, J. S. Reparaz, V. Marinova, D. Dimitrov, and S. O. Valenzuela. "Room-temperature anisotropic in-plane spin dynamic in graphene induced by $PdSe_2$ proximity". *Nature Materials*, [Accepted in principle].

3. K. Xu, L. M. Armesto, J. Světlík, J. F. Sierra, V. Marinova, D. Dimitrov, A. R. Goñi, A. Krysztofik, B. Graczykowski, R. Rurali, S. O. Valenzuela, and J. S. Reparaz. "Unravelling the Origin of Thermal Anisotropy in $PdSe_2$". *2D Materials*, 2024, **11**(4), 045006. DOI: https://doi.org/10.1088/2053-1583/ad64e3

4. L. Camosi, J. Světlík, M. V. Costache, W. Savero Torres, I. Fernández Aguirre, V. Marinova, D. Dimitrov, M. Gospodinov, J. F. Sierra, and S. O. Valenzuela, "Resolving spin currents and spin densities generated by charge-spin interconversion in systems with reduced crystal symmetry". *2D Materials*, 2022, **9**(3), 035014. DOI: https://dx.doi.org/10.1088/2053-1583/ac6fec

5. Juan F. Sierra, Josef Světlík, and Sergio O. Valenzuela. Chapter "Spintronics in lateral spin devices in 2D materials" in a book "Beyond-CMOS: State of the Art and Trends". Wiley 2023. ISBN: 9781789451276. DOI: https://doi.org/10.1002/9781394228713